



# UNIVERSITÀ DEGLI STUDI DI TRIESTE

## XXX CICLO DEL DOTTORATO DI RICERCA IN NANOTECNOLOGIE

### Lipid raft formation and protein-lipid interactions in model membranes

Settore scientifico-disciplinare: FIS/03

DOTTORANDO

**Fabio Perissinotto**

COORDINATORE

**PROF. Lucia Pasquato**

SUPERVISORE DI TESI

**Dr. Loredana Casalis**

CO-SUPERVISORE DI TESI

**Dr. Denis Scaini**

**ANNO ACCADEMICO 2016/2017**

# TABLE OF CONTENTS

<b>ABSTRACT</b> .....	4
<b>INTRODUCTION</b> .....	6
<b>1. Biological membranes</b> .....	6
1.1 Lipid composition of cellular membranes .....	7
1.2 Membrane proteins .....	11
<b>2. Physical and structural properties of cell membranes</b> .....	12
2.1 Lipid-lipid interactions and phase separation .....	12
2.2 Membrane asymmetry .....	14
2.3 Lipid diffusion .....	15
2.4 Lipid-protein interactions .....	16
<b>3. Lipid rafts</b> .....	17
3.1 Cellular functions of lipid rafts .....	18
3.2 Lipid rafts and diseases .....	21
<b>4. Protein misfolding, aggregation and role of lipid rafts in Parkinson's disease</b> .....	24
4.1 Parkinson's disease .....	25
4.2 Alpha synuclein .....	27
4.3 Alpha synuclein aggregation pathway .....	29
4.5 Alpha synuclein interaction with biological membranes .....	31
4.6 Alpha synuclein and metal ions in Parkinson's disease .....	33
<b>5. Artificial model membranes: a great tool for studying lipid raft domains</b> .....	34
5.1 Membrane models .....	35
5.2 Model membrane preparations .....	36
<b>6. Analytical techniques to characterized artificial lipid bilayers</b> .....	40
6.1 Atomic force microscopy .....	40
<b>RESULTS AND DISCUSSION</b> .....	45
<b>7. Optimization of drop-casting method for the production of complex artificial model membranes</b> .....	45
7.1 One-component lipid bilayers .....	45
7.2 Two-component membranes .....	47
7.3 Three-component membranes .....	50
7.4 Application of drop-casting method to study membrane-carbon nanotube interactions .....	52
7.5 Discussion .....	54

<b>8. Raft-like lipid bilayers by direct vesicle fusion and applications in biomolecule-lipid interactions</b> .....	56
8.1 Ternary membranes .....	56
8.2 Stability of SLB in aqueous solution .....	62
8.3 GM1 distribution on lipid rafts.....	65
8.4 Lipidated-Prion protein (PrP <sup>C</sup> ) insertion into model membranes.....	68
8.5 Discussion.....	70
<b>9. Iron-mediated interaction of Alpha Synuclein (<math>\alpha</math>S) with lipid raft model membranes</b> .....	73
9.1 In vitro iron-mediated aggregation of $\alpha$ S.....	74
9.2 Interaction of monomeric $\alpha$ S with lipid raft model membranes .....	77
9.3 Interaction of iron-induced oligomers of $\alpha$ S with lipid raft model membranes.....	80
9.4 Attenuated total reflectance infrared spectroscopy measurements .....	82
9.5 Discussion.....	88
<b>CONCLUSIONS</b> .....	92
<b>FUTURE PERSPECTIVES</b> .....	94
<b>MATERIALS AND METHODS</b> .....	95
<b>APPENDIX</b> .....	101
<b>BIBLIOGRAPHY</b> .....	107

## ABSTRACT

The biological membranes of eukaryotic organisms contain functional, highly dynamic nano-domains called "lipid rafts" (LRs) which are enriched in cholesterol, sphingolipids and GPI-anchor proteins. They are involved in several biological processes which implicate or are mediated by the plasma membrane as protein trafficking, intra-extracellular cell signaling, chemotaxis and cell polarity. Moreover, LRs seem to have a critical role in the onset of some neurodegenerative diseases such as the Alzheimer's disease (AD), Parkinson's disease (PD) and Prion protein disorders. In the last two decades, the complexity of studying such domains in living cells has caused a growing interest in the use and design of artificial membrane models, which mimic the structure and composition of biological membranes. In this context, I promoted the formation and investigated the properties of lipid raft domains in artificial lipid bilayers by exploiting Atomic Force Microscopy (AFM). AFM provides in fact great advantages for the investigation of nanoscale surface properties of biological samples in near-physiological environment. First, I compared two different fabrication methods for the production of artificial lipid bilayers, the drop-casting and the direct vesicle fusion techniques. I started from one-component lipid membranes and I progressively moved towards more complex models, as binary and ternary lipid compositions, in order to study the main LRs features in relation to specific biological phenomena, such as protein-lipid interactions involved in particular pathological diseases. The direct vesicle fusion method appeared to be the most suitable approach in term of reproducibility, stability and control of lipid composition. I took advantage from this method for carrying out a morphological characterization of raft-like model membranes composed by phosphocoline (DOPC), sphingomyelin (SM) and cholesterol focusing in particular on lipid phase behavior. Membranes exhibited the coexistence of two lipid phases, the fluid phase made by DOPC, and the solid-ordered phase made by SM and cholesterol, the latter resembling raft-like domains.

With selected 3-component lipid systems, I then investigated the distribution of GM1 ganglioside, a LR marker, into my system, demonstrating its preferential localization in the nano-domains and highlighting the feasibility and versatility of model membrane technology. For the first time, I studied the binding of synthetic full-length Prion protein ( $\text{PrP}^{\text{C}}$ ), carrying a C-terminal membrane anchor (MA), to LRs domains. The conversion of  $\text{PrP}^{\text{C}}$  into the scrapie isoform  $\text{PrP}^{\text{Sc}}$ , which displays high propensity to aggregate leading to cytotoxicity, has been reported to take place into LRs and to be influenced by lipid-anchors. I demonstrated with this study the propensity of this protein to specifically target LR domains of my artificial systems, observing an aggregation process occurring even at low protein concentrations. A comparative analysis with  $\text{PrP}^{\text{C}}$  lacking of MA is however required to assess the role of lipid-anchor into the protein distribution and aggregation.

Finally, in the last part of my research I focused on the study of the role of iron ions in the interaction between alpha synuclein ( $\alpha$ S) and lipid membranes.  $\alpha$ S is the central protein of PD and the presence of amyloid  $\alpha$ S fibrils is the main pathological hallmark of the disease. Several factors such as membrane-binding, pH and metal ions concentration, can promote *in vivo* and *in vitro* protein aggregation forming different kinds of structures. Iron represents a big challenge for finding therapeutic approaches against the disease. Increasing concentrations of iron have been found in the brain of PD patients and a strong interplay between iron, oxidative stress and  $\alpha$ S-aggregation has been postulated. Recently several evidences have showed that intermediate aggregated products, called oligomers, rather than fibrils are the elements which cause neurotoxicity. By AFM in combination with attenuated total reflectance infrared (ATR-IR) spectroscopy, I compared the structural behavior of the wild-type (wt) and a mutant form of  $\alpha$ S (A53T) in presence of  $\text{Fe}^{2+}$  ions and the effect of the iron ions on the interaction with my artificial membrane, and specifically with LRs. I demonstrated that iron strongly promotes the formation of  $\alpha$ S-oligomers with a greater propensity of the mutant form to aggregate. ATR-IR data revealed that the mutant is characterized by a bigger content of  $\beta$ -sheet secondary structures and a more-pronounced structural disorder as well as a better ability to form complexes with iron. At the same time, the AFM comparative analysis of protein monomers vs oligomers showed oligomer accumulation, with the formation of protein clusters, on raft-like domains. On the contrary, monomers in absence of iron ions bind to the membrane (wt  $\alpha$ S to both lipid phases, the mutant A53T  $\alpha$ S to the fluid phase only) leading to extensive defect sites and to slight aggregation. The protein clustering on raft-like domains suggests a possible role of  $\alpha$ S-oligomers in interfering with the biological processes that are modulated by proteins enriched on LRs. The administration of iron-induced  $\alpha$ S-oligomers to neuronal cells primary cultures would be a promising next step in order to gain new insights into the relation between iron, LRs and the multi-factorial aggregation of  $\alpha$ S.

# INTRODUCTION

## 1. Biological membranes

Biological membranes represent one of the most important structures in cell biology. Cell membrane acts as a physical barrier separating intracellular environment from the extracellular one and maintaining cellular homeostasis. In eukaryotic cells, membranes surround also cell organelles, as Golgi apparatus, endoplasmic reticulum and mitochondria. Beside its structural role in compartmentalization, the cell membrane is involved in a variety of cellular processes such as signaling, cell-cell interactions and ion conductivity. Membrane components both communicate with intracellular and extracellular environment, by interacting with structural proteins of cytoskeleton, as actin and tubulin, and with small molecules and polymeric compounds of extracellular matrix (ECM) <sup>1</sup>.

In spite of their different functions, the basic structure of all the biological membranes is a lipid bilayer. Cell membrane is a very complex and highly dynamic structure with thousands of different phospholipids with a variety of saturation and length of acyl chains. In addition to the various types of phospholipids, membrane proteins and sugars are also key components of the structure. While lipids primary exert a structural role, membrane proteins are the nanomachines that carry out specific membrane functions, enabling membranes to send and receive messages and to transport molecules in and out of cells and compartments.

In 1972, Singer and Nicholson proposed the “*fluid mosaic model*” to describe the dynamic and fluid structure of plasma membrane. The model is based on the thermodynamics principles of the organization of lipids and proteins of a biological membrane <sup>2</sup>. According to the model, the membrane was represented as a uniform fluid lipid bilayer of phospholipids in which globular integral proteins and glycoproteins were able to laterally diffuse within the plane of the bilayer (Fig. 1A). The model emphasized the fluidity of the membrane and the coexistence of lipids and proteins, without the presence of any membrane sub-compartmentalization. However, in the next two decades a large number of studies has highlighted the lateral heterogeneity of membrane, featuring the presence of different sub-compartment that differ in their composition and biophysical properties, and that limit the mobility of many membrane proteins within the bilayer. In vivo, the first evidence of the presence of membrane heterogeneity has been observed in epithelial cells which have been shown to be morphologically and functionally polarized, displaying a selective delivery of lipids to their apical and basolateral sides <sup>3</sup>. This new view of membrane structure has brought to formally develop a new model of plasma membrane

organization, called the “lipid rafts model” <sup>4</sup> (Fig. 1B). According to the raft hypothesis, the interaction between specific lipids in the plane of the bilayer drives the formation of functional ordered membrane domains, the so-called lipid rafts, which are involved in several biological events such as signal transduction and membrane trafficking pathways and other biological processes. We will briefly review the principle components of biological membranes and the biophysical properties that govern the integrity and functionality of these essential cellular structures.

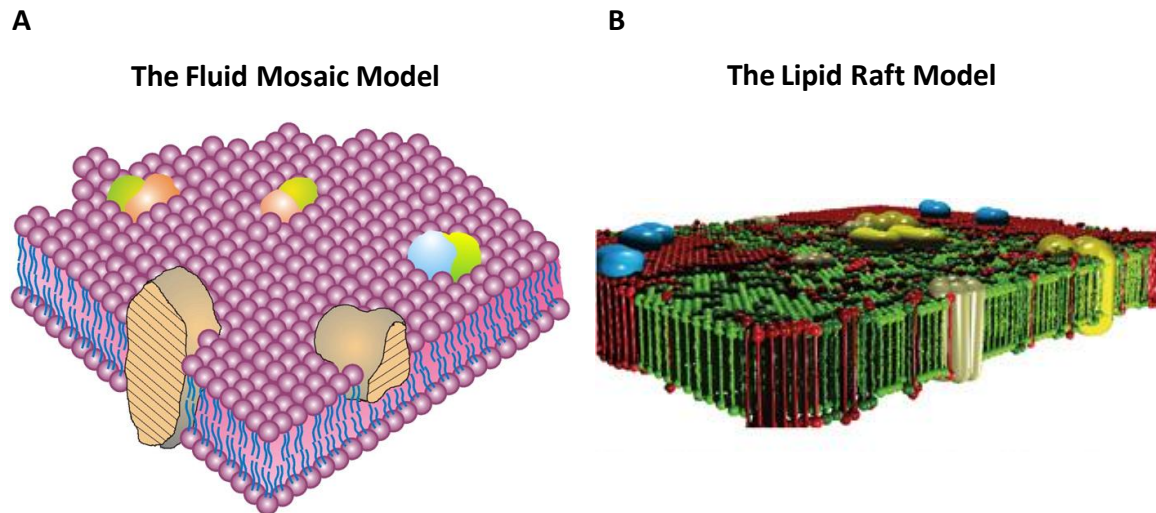


**Figure 1. The Fluid Mosaic Membrane Model and the Lipid Raft Model of biological membrane structure. (A)** The picture represents a section view of a cell membrane with globular integral membrane proteins randomly distributed in the plane of a completely fluid bilayer. The membrane does not contain other membrane-associated structures or membrane domains of different compositions. *From Singer and Nicholson, 1972* <sup>2</sup>. **(B)** The picture, generating from Monte Carlo simulations, represents a modern view of membrane structure which exhibits lateral heterogeneities, cluster and domain formation within the membrane plane. *From Eeman and Deleu, 2009* <sup>5</sup>.

### 1.1 Lipid composition of cellular membranes

Lipids are described as water-insoluble biomolecules that are highly soluble in organic solvents. They are amphipathic, containing a hydrophobic domain (or apolar end) and a hydrophilic domain which interacts with aqueous environment. The self-association of the hydrophobic portions minimizes the total surface in contact with water, leading to an increase of system entropy. The polar head of lipids interacts with water and other headgroups generating an energetically stable system in aqueous solution <sup>6</sup>. At physiological concentration, lipids are able to assemble into different structural associations (lamellar, micellar and cubic), according to the volume of their polar headgroups and fatty acyl chains. This ability is referred to as lipid polymorphisms <sup>7</sup>.

However, biological membranes are mostly lamellar and this is due to lipid-lipid and protein-lipid interactions which make the lamellar state energetically more favorable.

Lipids have a variety of biological roles: they are used for energy storage, as signaling molecules acting as first and second messengers in signal transduction, and as structural building blocks of biomembranes. Biological membranes are characterized by a different lipid composition which even differs among membrane compartments <sup>8</sup> (Fig. 2). For example, the total number of lipid species in cellular lipidome is likely to be in the thousands <sup>9</sup>. A possible reason for this lipid complexity is to guarantee a robust apparatus even in presence of local environmental changes, such as pH and osmolarity. The most abundant lipids of eukaryotic cell membranes are glycerophospholipids, sphingolipids and sterols. The former two are classified according to their polar headgroup, acyl chain length and degree of saturation.

		Percentage of total lipids				
		Human Erythrocyte plasma membrane	Human Myelin	Bovine heart Mitochondria	<i>E. coli</i> Cell membrane	Spinach Chloroplast thylakoid membrane
Glycerophospholipids	Phosphatidic acid	1.5	0.5	0	0	0
	Phosphatidylcholine	19	10	39	0	0
	Phosphatidylethanolamine	18	20	27	65	0
	Phosphatidylglycerol	0	0	0	18	7
	Phosphatidylinositol	1	1	7	0	2
	Phosphatidylserine	8	8	0.5	0	0
	Cardiolipin	0	0	23.5	17	0
Glyceroglycolipids	Monogalactosyldiacylglycerol	-	-	-	-	53
	Digalactosyldiacylglycerol	-	-	-	-	27
	Sulfoquinovosyldiacylglycerol	-	-	-	-	7
Sphingophospholipid	Sphingomyelin	17.5	8.5	0	0	0
Sphingoglycolipid	Ganglioside	10	26	0	0	0
	Cholesterol	25	26	3	0	0
	Other	0	0	0	0	4

Figure 2. Lipid membrane composition of different cell membranes

- Glycerophospholipids.** Glycerophospholipids are the major structural lipids in eukaryotic cell membranes. Their hydrophobic portion is a diacylglycerol (DAG), a glyceride consisting of two fatty acid chains esterified to a glycerol molecule (in C1 and C2). The acyl chains can be saturated or cis-unsaturated with varying length. A phosphate group is attached to the C3 of the glycerol molecule giving rise to several kind of phospholipids such as phosphatidic acid (PA), phosphatidylcholine (PC), phosphatidylserine (PS), phosphatidylinositol (PI), and cardiolipin (CL) <sup>10</sup>. PC self assembles spontaneously into planar lipid bilayer and represent more than 50% of total glycerophospholipids in most eukaryotic membranes. It has one cis-unsaturated acyl chains which renders the molecule

fluid at room temperature (Fig. 3)<sup>11</sup>. In biological membranes glycerophospholipids are usually present with the acyl chain of C1 saturated with 16-18 carbons and with longer unsaturated C2. Their degree of saturation contributes to the elasticity of the membrane, influencing insertion and sequestration of the proteins. Moreover, it has to be considered that lipids are not only the structural constituents of the membrane but they actively participate to several membrane processes. For example, phosphatidylethanolamine (PE) due to its conical geometry, imposes a curvature stress onto a PC bilayer, mediating membrane protein accommodation and modulating their activity<sup>6,12</sup>. PA instead is the biosynthetic precursor of all glycerolipids and acts as a signaling lipid, recruiting cytosolic proteins to the membrane<sup>13</sup>.

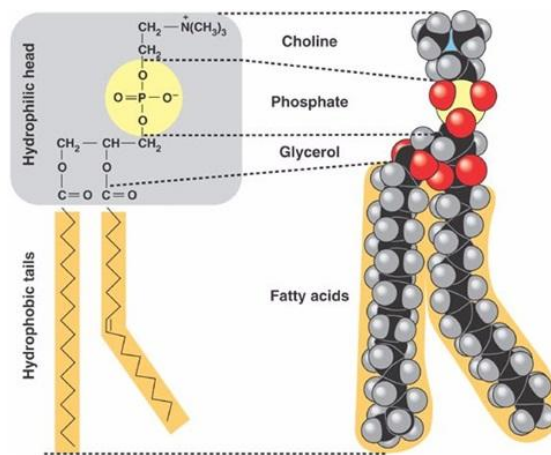


**Figure 3. Representation of the structure of phosphatidylcholine (PC).** From Rodriguez-Berdini and Ferrero, (2016)<sup>14</sup>.

- **Sphingolipids.** Sphingolipid molecules are built on ceramide backbone, which is composed of sphingosine and a fatty acid. In cell membrane they are usually present with both acyl chains saturated with 16 to 24 carbons long (Fig. 4). The major sphingolipids in mammalian cells are sphingomyelin (SM) and the glycosphingolipids (GSLs)<sup>10</sup>. SM molecules have a PC or PE headgroup and pack more tightly into bilayer due to the unsaturation of the acyl chains. Sphingolipids are enriched in lipid rafts being able to form specific interaction with cholesterol, which modulates their phase in membrane (see next paragraph). SM is specially found in neuronal cell membranes with a greater concentration on the outer than the inner leaflet. Moreover, it is a component of myelin, the structure that surrounds axon neuronal membrane, and it plays significant roles in signaling pathways. The degradation and synthesis of SM produce, indeed, important second messengers for signal transduction<sup>15</sup>.

Among glycosphingolipids, gangliosides such as GM1, GM2, GM3, have to be mentioned. They have two acyl chains embedded in the plasma membrane and one or more carbohydrate residues linked to a hydrophobic lipid moiety through a glycosidic linkage. In addition, they have terminal sialic acids linked to sugar chains which are implicated in neural transmission and synaptogenesis. They are found predominantly in nervous system and are concentrated on cell surface, especially on lipid raft domains <sup>4</sup>. They are involved in many signaling processes like cell to cell adhesion, receptor binding and signal transduction <sup>16</sup>. Accumulation of gangliosides in cell lysosomes causes a group of diseases, called gangliosidosis (i.e. Tay-Sachs disease <sup>17</sup>).

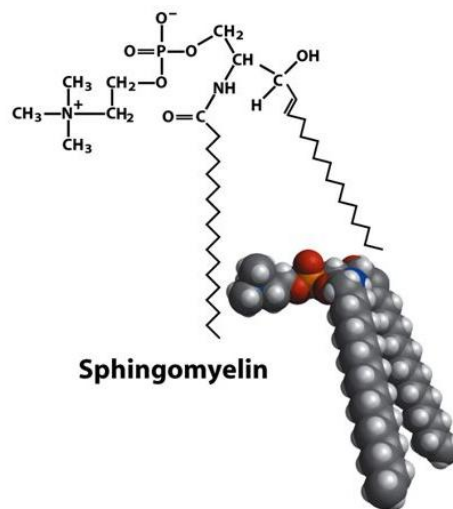


**Figure 4. The structure of sphingomyelin.** The formula and the space-filling model of the molecule are reported. *From Nelson et al, 2013* <sup>18</sup>.

- **Sterols.** Sterols are organic molecules characterized by a fused four-ring core structure. They represent the major non-polar lipids of plasma membrane. The most abundant sterol in mammalian membranes is cholesterol (Fig. 5), representing ca 30% of the total lipid content. Cholesterol is able to interact with lipid membrane by inserting perpendicularly into the lipid bilayer. The hydroxyl group forms hydrogen bonds with the carbonyl oxygen of phospholipid headgroups while the hydrocarbon tail positions itself in the non-polar core of the bilayer. Cholesterol is preferentially present into lipid rafts where it strongly displays higher affinity for saturated acyl chains, like SM, instead of unsaturated ones <sup>19</sup>. It plays an important role regulating membrane fluidity by packing the acyl chains and increasing the rigidity of the bilayer. This effect of cholesterol results in the reduction of bilayer permeability, while the effect on lateral diffusion of proteins and lipids within the plane of the membrane is minimal <sup>20</sup>.

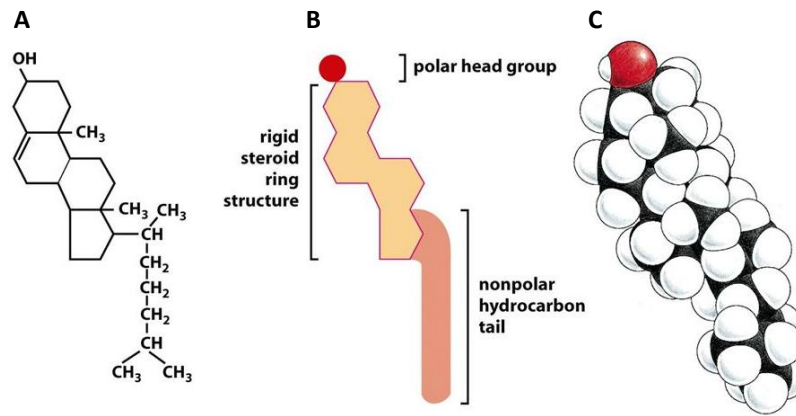


**Figure 5. The structure of cholesterol.** Cholesterol is represented (A) by a formula, (B) by a schematic drawing, and (C) as a space-filling model. *From Alberts et al, 2002*<sup>21</sup>.

## 1.2 Membrane proteins

Membrane proteins are responsible for carrying out most of cellular membrane functions, representing 50% of membranes in weight. Protein content varies depending on cell type and subcellular compartments. Some proteins are bound only to the membrane surface, whereas others cross the membrane bilayer having both extracellular and cytoplasmic domains. Based on the nature of lipid-protein interactions, membrane proteins can be classified into two wide categories: integral proteins and peripheral proteins<sup>21</sup> (Fig. 6).

1. **Integral proteins.** These proteins have one or more hydrophobic portions that are inserted into the lipid bilayer, anchoring the protein to the membrane. Among this class, some proteins, called transmembrane proteins, span the entire membrane by one or more membrane-spanning domains which are usually  $\alpha$  helices of 20-25 hydrophobic amino acids or multiple  $\beta$  sheets. Transmembrane proteins with  $\alpha$  helices domains are usually receptors involved in signaling events, whereas those with multiple  $\beta$  sheets structure form pores in membrane and have a role in the uptake and disposal of small molecules across the membrane. In contrast to transmembrane proteins, some integral proteins are anchored to one membrane leaflet by a lipid tail, covalently bound to the protein structure. One class of these proteins is inserted into the extracellular leaflet by glycosylphosphatidylinositol (GPI) anchors. Many GPI-anchor proteins are associated with lipid rafts<sup>22</sup>.

2. **Peripheral proteins.** These proteins do not interact with the hydrophobic core of lipid membrane, instead are bound to the membrane by direct interactions with lipid headgroups or by indirect interactions with integral proteins. Peripheral proteins located on cytosolic side of the membrane perform a wide range of functions such as anchoring cytoskeleton proteins with membrane and triggering intracellular pathways. One important group of peripheral proteins are water-soluble enzymes, such as phospholipases which hydrolyze headgroups of phospholipids and are involved in the degradation of damaged cells<sup>21</sup>.

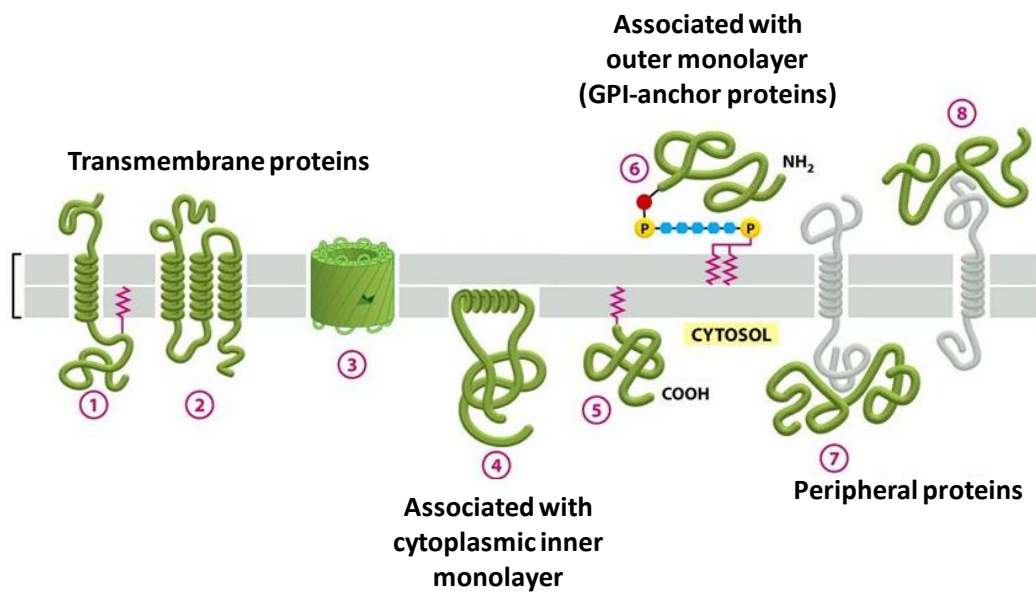


**Figure 6. Membrane proteins classification.** Trans-membrane proteins cross the bilayer as (1) a single  $\alpha$  helix, (2) as multiple  $\alpha$  helices, or (3) as a  $\beta$  barrel. Other membrane proteins are exposed at only one side of the membrane. (4) Some of these are anchored to the cytosolic surface by an amphipathic  $\alpha$  helix that partitions into the cytosolic monolayer of the lipid bilayer through the hydrophobic face of the helix. (5) Others are attached to the bilayer solely by a covalently attached lipid chain or, (6) via an oligosaccharide linker, to phosphatidylinositol in the non-cytosolic monolayer. (7, 8) many proteins are attached to the membrane only by non-covalent interactions with other membrane proteins. *From Alberts et al, 2002*<sup>21</sup>.

## 2. Physical and structural properties of cell membranes

### 2.1 Lipid-lipid interactions and phase separation

In solution lipids spontaneously self-assemble forming a lipid bilayer, which allows tight packing of adjacent side chains with the maximum exclusion of water from the hydrophobic domain. The organization of lipids in the bilayer is strongly affected by the nature of acyl chains, the

headgroups and physical parameters such as ion content, pH and temperature <sup>23</sup>. At a given temperature a lipid bilayer can exist in either a liquid-disordered ( $L\alpha$  or  $L_d$ ) or a solid-ordered phase ( $S_o$ ) (Fig. 7 A). The difference between these two phases is referred to the fluidity of the hydrophobic domains. Lipids in solid-ordered state have the hydrocarbon chains fully extended and closely packed whereas the hydrocarbon chains of lipids in fluid state are randomly oriented and fluid. Each lipid has a specific transition temperature ( $T_m$ ) at which it undergoes a transition from gel to fluid phase.  $T_m$  mainly involves the disordering of hydrocarbon chains, and several factors can directly affect the phase transition temperature including hydrocarbon length, unsaturation, charge, and headgroup species <sup>24,25</sup>. As the hydrocarbon length is increased, van der Waals interactions become stronger requiring more energy to disrupt the ordered packing, thus the phase transition temperature increases. Likewise, introducing a cis double bond into the acyl group puts a kink in the chain which requires much lower temperatures to induce an ordered packing arrangement. Saturated lipids as SM have usually higher  $T_m$  compared to unsaturated ones. The presence of cholesterol strongly increases the complexity of the system, exhibiting a dual effect on lipid bilayer <sup>26</sup>. Cholesterol stabilizes the membrane interacting with the  $L\alpha$  phase and ordering the acyl chains. At the same time it disorders the  $S_o$  phase with a transition to a new phase called liquid-ordered phase ( $L_o$ ) in which the molecules are more tightly packed and ordered than in  $L\alpha$  phase <sup>27,28</sup>. Notwithstanding its ability to interact with both lipid phases, it has been showed that cholesterol prefers to interact with ordered unsaturated lipids such as SM although for non completely clear reasons <sup>29</sup>. As a matter of fact it is a peculiar feature of lipid rafts being enriched in cholesterol and SM.

The use of artificial membrane systems has been instrumental to study lipid behavior and phase transitions of biological membranes. Depending on the lipid composition, a lipid bilayer can exhibit different physical states including single liquid phase, two coexisting liquid phases, liquid-solid phase coexistence and single solid phase. Three-component (high  $T_m$  lipid/low  $T_m$  lipid/cholesterol) model membranes have the minimal number of components that yield complex phase behavior. Several studies have been performed on different ternary lipid mixtures as a function of temperature and relative molecular concentration. Different phase diagrams which summarize and identify each phase including the presence of coexisting phases, at all compositions, are now available for a better and easier interpretation of the biological membranes. In Fig. 7B is reported a phase diagram of a three-components lipid mixture that contains cholesterol, DOPC and SM in excess water, determined at 25°C from confocal fluorescent microscopy of ternary giant unilamellar vesicles (GUVs) <sup>30</sup>. The diagram displays coexisting  $L_o$  and  $L\alpha$  domains and shows that an increasing cholesterol concentration can induce the formation of a boundary between the  $L\alpha$ - $L_o$  coexistence region and the liquid-solid coexistence region.

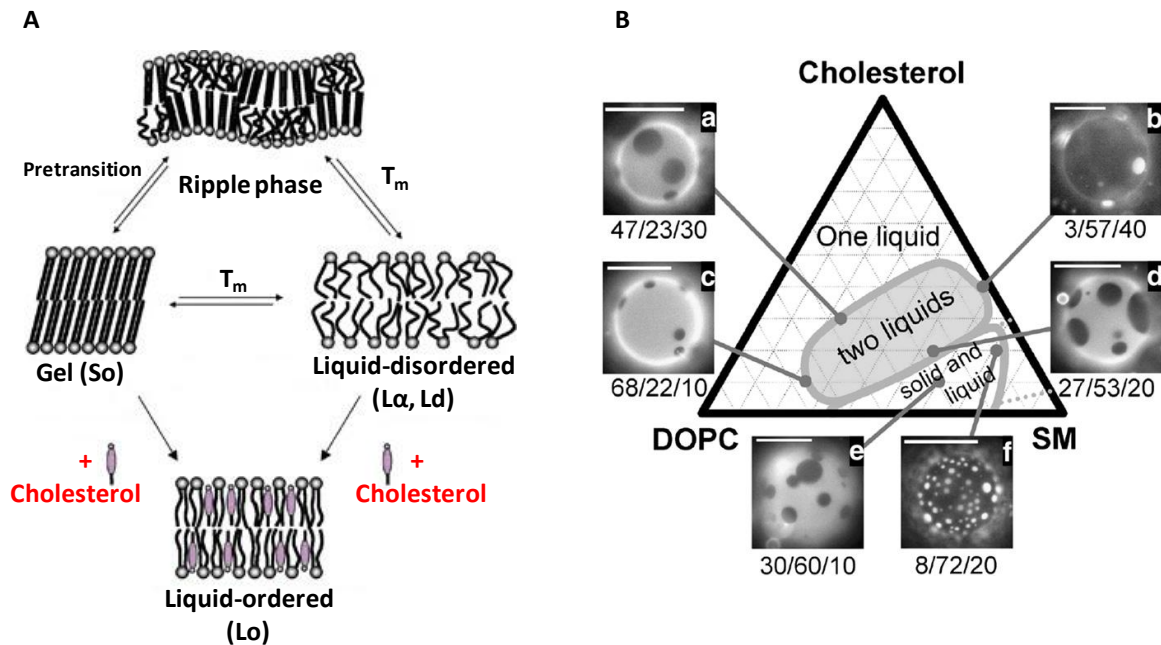


**Figure 7. Lipid phase transition.** (A) Different physical state adopted by a lipid bilayer in liquid environment. (B) Phase diagram for a three-component lipid mixture made of DOPC, SM and cholesterol, determined at 25 °C based on confocal fluorescence microscopy images. The compositions DOPC/SM/Chol are given in mole fractions. Each side is divided into ten fractions each of which corresponds to an increase of 10% molar of each components. The dark regions are liquid phases rich in SM and cholesterol while the bright regions are rich in DOPC. The scale bars are 20  $\mu\text{m}$ . Adapted from Veatch and Keller, 2005<sup>30</sup>.

## 2.2 Membrane asymmetry

Plasma membrane is asymmetric in the composition of lipids and proteins. The outer leaflet consists mainly of PC, SM and GPI-anchor proteins, whereas PE and PS are the predominant phospholipids of the inner leaflet as well as PI, which plays an important role in cell signaling (Fig. 8). Cholesterol is distributed in both leaflets being present in about the same molar amount as the phospholipids, but apparently enriched within the inner leaflet<sup>31,32</sup>. For instance, a study based on quenching of fluorescence and fluorescence photobleaching of two fluorescent cholesterol molecules (dehydroergosterol and NBD-cholesterol) have showed an enrichment of cholesterol in the inner leaflet of human erythrocyte plasma membrane<sup>33</sup>.

Maintenance of membrane asymmetry is an active process which is performed by several proteins. Translocation of lipids from one leaflet to the other is called “flip-flop” and is catalyzed by enzymes, know as lipid translocases or flippases, which require ATP hydrolysis to perform this transbilayer movement. ATB-binding cassette transporters (ABC) seem to move (flop) phospholipids from the inner to the outer leaflet whereas P-type ATPases control movement of lipids to the cytoplasmic layer (flip)<sup>34</sup>. Membrane asymmetry is known to affect various bilayer

properties such as shape, permeability and stability. For instance, the interaction of PS with skeletal proteins improved mechanical stability of membrane of red blood cells<sup>35</sup>. Local and global changes of transbilayer asymmetry are directly involved in many cellular processes. For example, apoptotic cells show a collapse of lipid asymmetry which results in the PS exposure that is used as recognition signal by macrophages<sup>36</sup>. In addition, PE exposure is essential for cell cycle progression<sup>19</sup>.

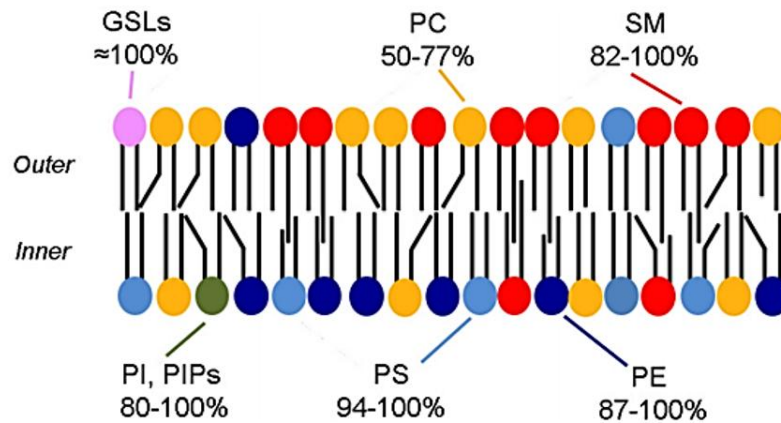


**Figure 8. Schematic representation of lipid asymmetry in erythrocyte membrane.** The colors indicate the asymmetric distribution of phospholipids. The range in percentage indicates the amount present in the preferred leaflet. *From Fujimoto and Parmryd, 2016<sup>38</sup>.*

### 2.3 Lipid diffusion

Besides transbilayer lipid movements which are slow in physiological conditions and relatively easy to maintain, lipids even undergo lateral diffusion that happens when molecules exchange place in the same leaflet. The rapid thermal diffusion or Brownian diffusion within the two dimensional plane of the membrane makes the membrane a two dimensional fluid entity. This effect occurs very quickly, with a diffusion coefficient around  $10^{-7}$  and  $10^{-8}$   $\text{cm}^2/\text{sec}$  (at room temperature), that means a single lipid moves around all erythrocyte membrane cell in around 1 sec. Lateral diffusion coefficient ( $D_L$ ) of lipids is one of the most important dynamical parameters of biological membranes and it is closely related to the membrane structure. Different experimental techniques are used to calculate this coefficient and are typically based on fluorescence microscopy approaches<sup>39,40</sup>. Generally, lateral diffusion coefficient is strongly affected by the packing of lipids and the by molecular ordering: a denser lipid packing in the bilayer leads to a decrease of  $D_L$ <sup>41</sup>. The 2D diffusion of molecules of the size of lipids is treated using the free area theory. The theory considers a particle performing a two-dimensional random walk. For each diffusion step a molecule requires sufficient free area to move and certain minimal

energy to perform engage the step<sup>42</sup>. It was found that  $D_L$  depends on the degree of saturation of lipid acyl chains.  $D_L$  increases with increasing number of double bonds, as a consequence of the increased headgroup area<sup>43</sup>.

Since in a real cellular membrane the lateral diffusion of lipids is influenced by proteins, raft domains and interactions with the cytoskeleton, various artificial model membrane systems have been developed in order to investigate how each of the before mentioned factors can affect lateral movements of lipids<sup>44,45</sup>. In general, several studies on three-component model membranes (i.e. DOPC/SM/Chol) have demonstrated that  $D_L$  is about 2:10-fold smaller in the  $L_o$  phase and the activation energy for the diffusion process in the  $L_o$  is higher than for the  $L_\alpha$  phase<sup>46</sup>.

## 2.4 Lipid-protein interactions

Lipid-protein interactions are very important for the stabilization of protein structure, regulation of protein activity and for partition of proteins in different lipid domains, as in lipid rafts. At the molecular level, these interactions drive the complex organization of plasma membrane.

In general, membrane proteins with different length of their transmembrane domains (TMDs) tend to localize into different lipid environments, to minimize the energetically unfavorable exposure of hydrophobic residues to aqueous environment. For instance, proteins with long TMDs segregate with long-chains lipid molecules (*hydrophobic matching*). When a length mismatch is present between TMDs and the lipids associated with the proteins, protein-protein interactions induce the formation of lateral protein-rich aggregates (*hydrophobic mismatching*)<sup>47</sup> (Fig. 9). Membrane proteins are usually surrounded by a layer of lipid molecules which interacts with the membrane-penetrating surface of the protein. These lipid molecules are called annular lipids, because they form a ring around the protein. They adopt a distorted conformation interacting with the surface of the protein and are in rapid exchange with the bulk lipid of the membrane<sup>48,49</sup>. Some evidences have proposed the presence of lipid-binding sites on membrane proteins which are bound to different lipid molecules. These areas are referred to as non-annular lipid motifs and are located between transmembrane  $\alpha$ -helices or at protein-protein interfaces<sup>50</sup>. These interactions are essential for the partition of the proteins in different membrane domains or for the regulation of their activity. For instance, the HIV glycoprotein gp41, contains cholesterol-binding sites that regulates their distribution into lipid raft domains<sup>51</sup>. The function of several G protein-coupled receptor is cholesterol-dependent, although it is not clear whether the interaction is specific with a well-known protein region or if the effect translates into a physical change of the surrounding membrane. Voltage ion-channels are other proteins whose activity is lipid-dependent<sup>52</sup>. For instance, potassium channels directly bind the membrane phospholipids

phosphatidylinositol 4,5-bisphosphate (PI(4,5)P<sub>2</sub>) leading to an increased probability of channel opening<sup>53</sup>.

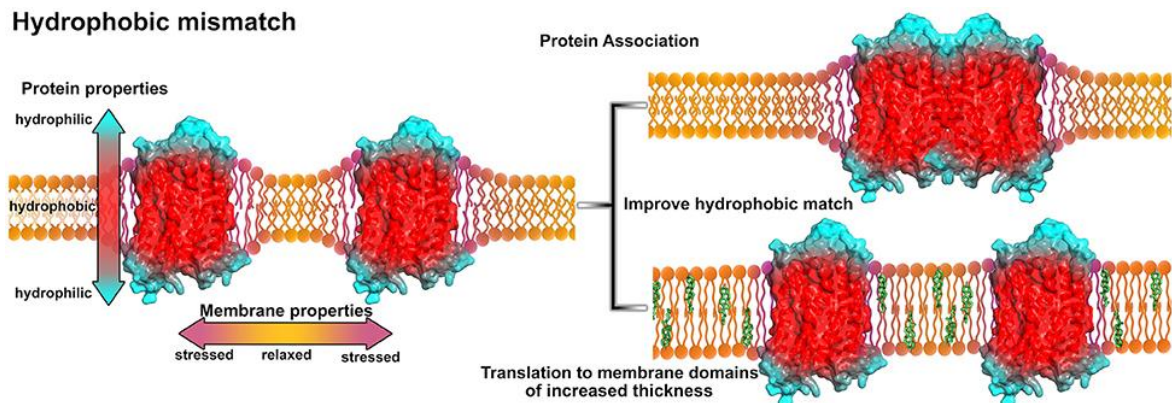


**Figure 9. Influence of the hydrophobic mismatch on membrane protein organization in membrane.** Due to protein insertion, the hydrophobic mismatch induces stress and curvature in the membrane (purple areas in the membrane). In order to reduce membrane stress, the proteins can associate or move to membrane areas of increased thickness, as membrane areas with higher cholesterol content (green, lower right). From Gahbauer et al, 2016<sup>54</sup>.

### 3. Lipid rafts

The first evidence of the lateral heterogeneity of membranes was observed in the 1970s<sup>55</sup>. Upon extraction of plasma membrane with cold non-ionic detergents, the membrane could have been separated in detergents-soluble membrane (DSMs) parts and detergent-resistant ones (DRMs). DRMs appeared to be enriched in cholesterol, sphingolipids and glycosylphosphatidylinositol (GPI)-anchored proteins and are referred to as lipid rafts<sup>56,57</sup>. However, it quickly became clear that DRMs do not reflect the native composition and organization of lipid rafts in living cells. For instance, the protein content can vary according to the choice and concentration of detergents used for the extraction<sup>58</sup>.

Since its initial formalization, the concept of lipid rafts has generated a huge amount of interest as well as controversy, due to the limitation in the available methodologies for the characterization of the physicochemical principles of lipid rafts homeostasis. To overcome these limitations in order to better investigate the identity and the physical and chemical properties of these domains, several biophysical and biochemical tools such as optical microscopy techniques, single-particle tracking (SPT) and model membrane technology have been developed<sup>59,60</sup>. In 2006, a new consensus definition of lipid rafts was coined, by which lipid rafts are small (10-200 nm in size), heterogeneous, highly dynamic (in terms of both lateral mobility and association-dissociation), functional membrane nanodomains, enriched in cholesterol and sphingolipids that segregate

proteins and compartmentalize cellular processes (Fig. 10). They have the potential to form microdomains (> 300 nm in size) upon clustering induced by protein-protein and protein-lipid interactions <sup>16</sup>. Lipid rafts are even characterized by the presence of gangliosides, lipidated proteins (GPI-anchor proteins) and transmembrane proteins <sup>61</sup>. Gangliosides represent a particular class of glycosphingolipids involved in cell-cell communication and were found to interact with rich-cholesterol ordered domains in plasma membrane <sup>62</sup>. Lipidated proteins insert into raft domains by GPI or palmitoyl anchors were some of the first proteins to be identified in DMRs <sup>63</sup>.

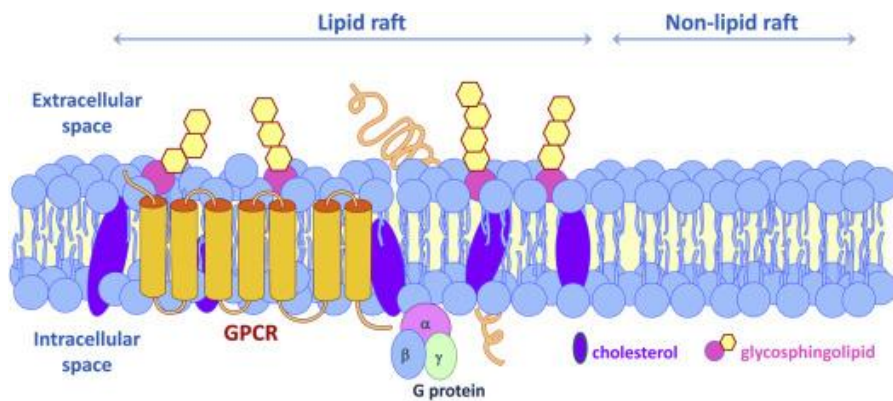


**Figure 10. Lipid raft organization in plasma membrane.** Rafts are enriched in phospholipids, glycosphingolipids, and cholesterol, and serve as active platform for receptors, such as G protein-coupled receptors (GPCRs), and other signaling molecules. From Villar et al., 2016 <sup>64</sup>.

Lipid rafts are present in both the inner and outer leaflets of asymmetric cell membrane and form functional platforms for the regulation of cellular processes <sup>65</sup>. However, it is very important to note that the plasma membrane displays a large variability in terms of raft abundance and localization of different proteins within lipid rafts, and this is dependent on cell types, generating a cell-specific organization of protein receptors and effectors <sup>16</sup>. Recently, several studies have shown the presence of these domains in cells using different biophysical and biochemical approaches, such as super-resolution fluorescence microscopy techniques <sup>66,67</sup>, Raman spectroscopy <sup>68</sup> as well as small-angle neutron scattering (SANS) <sup>69</sup>, and suggesting a key role for membrane heterogeneity in different cellular functions. However, the microscopy detection of lipid rafts *in vivo* remains the major challenge because of their dimensions and short lifetime, as well as the precise identification of their exact nature and role in various cellular phenomena.

### 3.1 Cellular functions of lipid rafts

The general function globally accepted and attributed to lipid rafts (and to membrane lipid order phase in general) is to segregate and cluster specific elements, such as proteins, regulating their

interactions with other membrane components and thus compartmentalize cellular processes<sup>4</sup>. Lipid rafts can regulate the activity of their associated components in different ways. For example, they co-localize molecules triggering reactions as in case of enzymes and substrates (Fig. 11 A), or they can directly affect the conformation of the proteins modulating their activities (Fig. 11 B)<sup>70,71</sup>. Here are reported some examples of lipid rafts in cell functions.

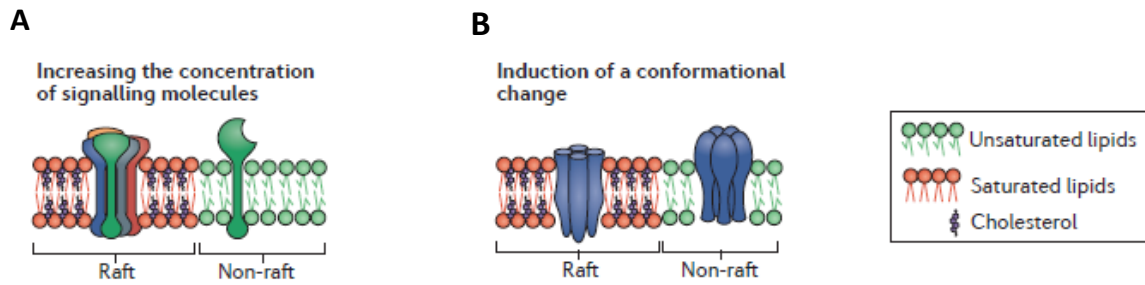


**Figure 11. Mechanisms by which lipid rafts can modulate the activity of their assembled molecules creating a catalytic platform. (A)** Molecules can be brought together, increasing the probability of their interaction, and thereby triggering a cascade pathways. **(B)** Protein receptors can be activated by a raft-dependent modification of their conformation. *From Sezgin et al., 2017*<sup>72</sup>.

- **Intracellular trafficking.** Lipid rafts seem to play a key role in the non-classic, clathrin-independent, endocytic pathway which involves the activity of a specific subset of rafts, called caveolae (Fig. 12). They are flask-like plasma membrane invaginations of 50-100 nm in diameter by which cell internalizes several membrane components and extracellular ligands<sup>73</sup>. Caveolae are enriched in specific raft proteins, called caveolins, whose oligomerization is the key determinant for the formation of these membrane invaginations. They are expressed in various tissues and cell types such as smooth muscle, fibroblasts, endothelial cells, and adipocytes. The functions of caveolae include endocytosis, calcium signaling, and regulation of various signaling events, as well as they can be used by pathogens to penetrate the cell, as the Simian Virus 40 (SV40)<sup>74</sup>. In this context, exosomes (EXOs) need a special mention (see Appendix A). EXOs are small extracellular vesicles (EVs) ensuring transport of molecules between cells and throughout the body. EVs contain specific signatures (RNA, DNA and proteins) and, functioning as inter-cellular messengers, have been shown to strongly impact on the fate of recipient cells<sup>75,76</sup>. EXOs have been proposed to play an important protumorigenic role, stimulating tumor cells growth, suppressing the immune response and even being part of the cancer progression and the metastatic process. Recent findings have demonstrated raft domain involvement in molecule sorting in EXOs which appeared to be enriched in GPI-anchor proteins that are usually present in DRMs of several types of cells<sup>77</sup>.

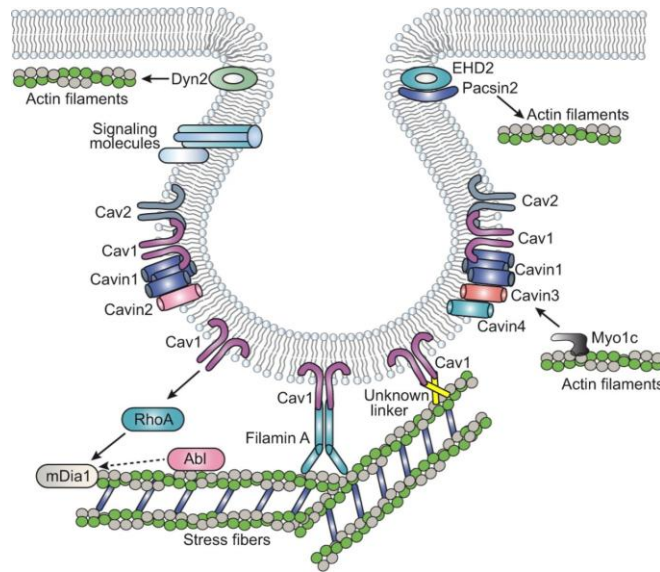


**Figure 12. Structure and composition of caveolae, a special type of lipid rafts.** Caveolins, cavins and pacsin2 are the main proteins that shape caveolae, whereas Dyn2, EHD2 and filamin A regulate their dynamics. Caveolae have functional or physical association with the cytoskeleton. Filamin A is the main protein mediating a linkage with stress fibers, but other yet unidentified linkers might exist (indicated as unknown linker). Regulators of stress fibers (Abl kinases and mDia1) that influence caveolae organization and trafficking are shown next to RhoA, the main regulator of stress fibers, which is regulated by Cav1. *From Echarri and Del Pozo, 2015*<sup>78</sup>.

- Communication with cytoskeleton.** Proteins involved in the stabilization of microtubules, such as Rho, RacGTPases, chaderin, actin, tubulin, and myosin, have been isolated in raft domains<sup>79,80</sup>. Lipid raft interactions with cytoskeleton are important for several biological processes, such as signaling, migration and cell adhesion. During adhesion, rafts are internalized in an actin- and microtubule-dependent manner allowing cells to detach from the extracellular matrix whereas, upon new adhesion events, rafts return to the cell membrane<sup>81</sup>. Moreover, rafts-cytoskeleton interactions are important for cell fate and cell mechanical adaptation<sup>82</sup>.
- Immune signaling.** Several studies have demonstrated that lipid rafts modulate various innate and adaptive immune responses. Various immune cells, such as B cells, T cells, basophils and mast cells, present protein receptors associated with lipid rafts and involved in signaling pathways leading to inflammation. Immunoglobulin E (IgE)-mediated signaling pathway was the first one that was shown to be associated with lipid rafts<sup>83</sup>. The signaling cascade initiates when IgE binds its receptor (FcεRI) on the surface of mast cells and basophils, increasing their association with lipid rafts. The effect is the recruitment of various molecules which cause the degranulation of mast cells<sup>84</sup>. Several other immune-associated GPI-anchor proteins have been found in DMRs suggesting their

preferential association with lipid rafts. Other immune receptors were found in DSMs of immature cells, but they translocate to DMRs upon receptor activation<sup>85-88</sup>. Moreover, it was shown that lipid rafts alter cytokine signaling, which is regulated by compartmentalization of cytokine receptors on raft domains creating a signaling platform for the recruitment of kinases and adaptor molecules.

- **Synaptic transmission and plasticity.** Lipid rafts were demonstrated to be involved in neuronal communication, being present in neurons and glial cells<sup>89,90</sup>. They contribute to neurotransmitter exocytosis at pre-synaptic terminals, and to cluster neurotransmitter receptors and their downstream effectors. The Ca<sup>2+</sup>-dependent release of vesicle content at synaptic terminus, is impaired by decreased cholesterol levels<sup>91</sup>. Moreover, a large number of proteins involved in this exocytic process, such as SNARE proteins (SNAP25, VAMP2 and Syntaxin), have been found in DMRs<sup>92</sup>. Several studies have been focused on correlation between cholesterol and synaptic plasticity. The synaptic plasticity is affected by the shuttling of several synaptic proteins between rafts and non-rafts domains, leading to strengthen or weaken the synaptic activities over the time.

### 3.2 Lipid rafts and diseases

Recent data have demonstrated that lipid rafts are linked to different kind of diseases such as cancer, cardiovascular diseases and neurodegenerative diseases as well as host-pathogen interactions. Rafts provide a specific environment for signaling molecules and protein receptors, such as G-proteins or members of the tyrosine kinase Src family (SFks), which are associated with the onset of many kind of diseases.

- **Cancer.** Lipid rafts are implicated in signaling pathways in cancer progression as well as they play a critical role in cancer cell adhesion and migration. Alternation of cell adhesion and migration are directly correlated with aggressive invasion and metastatic spread of cancer, and these processes involve remodeling of extracellular matrix of the tumor microenvironment and adhesion molecules at the cancer cell surface<sup>93,94</sup>. Several studies have demonstrated that CD44, the major cell adhesion protein of cancer cells, is localized into lipid rafts and that rafts regulate functionality of this protein. Impairment of rafts by cholesterol depletion, leads to an increased shedding of CD44 in human glioma cells<sup>95</sup>. Cell-cell adhesion is facilitated by the activity of transmembrane receptors (integrins) which allow cells to bind extracellular matrix components or ligands on other cells. The

organization of lipid rafts in the plasma membrane can directly affect the activity of integrins and, therefore the adhesion process <sup>96</sup>. When integrins engage their extracellular ligands, they cluster and co-cluster a number of cytoskeleton proteins among which the SFKs are implicated in controlling signal transduction downstream of the integrins and are activated in lipid rafts. Rafts disruption have been shown to inhibit SFKs activity, abrogating adhesion of breast cancer cells <sup>97</sup>. Apoptosis is one other key cell process associated with lipid raft integrity. Apoptosis is a programmed cell death process which is extremely important for removing excess of cells, and for the development and the prevention of cancer. The process is characterized by a receptor-dependent pathway which requires the binding of a ligand to death receptors, such as Fas (CD95) or TNF (tumor necrosis factor), leading to a downstream cascade which concludes with an apoptotic cell death. Fas and other various molecules downstream of the signaling apoptotic pathway localize in lipid rafts. Alteration of raft integrity can prevent cell death with a possible onset of tumors and metastasis <sup>98,99</sup>.

- **Host-pathogen interactions.** During the infection process, pathogens take advantages of cellular lipids for their entire life cycle. The interactions range from membrane binding to release of infectious particles into host cells. Pathogenic microorganisms and both enveloped and non-enveloped viruses exploit cholesterol rich domains of plasma membranes (lipid rafts) to penetrate the cell and assembly platform for the production of viral envelope <sup>100</sup>. This phenomena is due to the enrichment of cellular receptors on lipid rafts which are targeted by viral and bacterial products, such as cholera toxin, allowing penetration of the pathogens and positioning viral envelope components in close proximity during assembly <sup>101-103</sup>. For instance, HIV takes advantage of lipid raft components for both entering to cell and assembling viral envelope. CD4 is the lipid raft receptor, which is targeted by HIV to penetrate the cell, and some reports have demonstrated that also the co-receptors CXCR4 and CCR5 can be localized to these domains <sup>104,105</sup>. At the same time, pathogens cause lipid raft disruption by the depletion of cholesterol, which leads to inactivation of immune responses facilitating the infectious process. Moreover, targeting lipid rafts alters host signaling and endocytic pathways which allow pathogens to reprogram cell lipid composition and host cell metabolism for the production of infective particles. Another effect of lipid rafts on virus infections is the formation of virological synapses, which represent the contact zones formed between virus and host cells, and facilitate the transmission of the infection <sup>106</sup>.

- **Cardiovascular diseases.** The involvement of lipid rafts in cardiac health and diseases is related to their activity as platform for receptor-signaling in endothelial cells of arteries and the heart muscle. In particular, the association of angiotensin II peptide to its receptor in raft domains can cause hypertension and pathological hypertrophy by its vasoconstriction activity<sup>107</sup>. Another example is represented by potassium ion channels Kv1, Kv2 and Kv4 in the heart, that are associated with both caveolae and caveolae-free rafts, and their disruption can cause hypertension, ischemia and heart failure<sup>108</sup>. Rafts are even involved in the pathogenesis of atherosclerosis, a disease of the blood vessels, that is characterized by extreme cholesterol deposition in arterial wall and subsequent uptake by macrophages<sup>109</sup>. The uptake causes a transformation of macrophages into foam cells, which are accumulated as plaques in blood vessels leading to stroke and heart attacks. The uptake of cholesterol by immune cells is mediated by lipoproteins and the process seems to be raft-dependent, being the LDL-receptor CD36 localized on raft domains<sup>110</sup>.
- **Neurodegenerative diseases.** Alterations of the molecular composition of lipid rafts are associated with several neurodegenerative disorders such as Parkinson's disease (PD), Alzheimer's disease (AD), Prion disease and amyotrophic lateral sclerosis<sup>99,111</sup>. Similar modifications in lipid raft matrix trigger processes involved in amyloidogenesis, aberrant protein misfolding and toxic signaling, in particular in early stages of different diseases<sup>112</sup>. Several protein markers of neurodegenerative disease, as alpha synuclein ( $\alpha$ S) for PD, A $\beta$  (amyloid-beta-peptide) for AD and the prion protein PrP<sup>C</sup>, have been demonstrated to be integrated into lipid rafts. In AD the accumulation of A $\beta$  leads to the formation of plaque which causes the progressive neuronal death. The amyloid precursor protein (APP) and the  $\beta$ - (BACE) and  $\gamma$ -secretase are the precursors involved in the A $\beta$  production and aggregation. APP translocates on rafts, where clustering with flotillin 1, regulates amyloid generation<sup>113,114</sup>. Moreover, BACE and  $\gamma$ -secretase modulate the A $\beta$  release through the binding of lipids present on these domains<sup>115,116</sup>. In Prion disease the accumulation of pathological PrP<sup>Sc</sup>, caused by the aberrant misfolding of PrP<sup>C</sup>, takes place in lipid rafts. In addition, alteration in lipid raft homeostasis, especially the cholesterol content, have been shown to affect the aggregation of the protein<sup>117</sup>.

## 4. Protein misfolding, aggregation and role of lipid rafts in Parkinson's disease

Several neurodegenerative disorders have as common feature the aberrant misfolding and the aggregation of specific proteins, called amyloid proteins. Amyloid proteins constitute a heterogeneous group of proteins characterized by the high propensity to adopt an incorrect conformation and the tendency to aggregate. The deposits found in patients with amyloid pathologies have in common many aspects. It was observed in fact, that in all of these cases there is the presence of amyloid fibrils composed by copies of the same protein. These fibrils are long (>1  $\mu\text{m}$ ), thin (10-20 nm), straight and unbranched. The protein, in these three-dimensional aggregates, is organized in  $\beta$ -sheet conformation, perpendicular to the main axis of the fibril <sup>118</sup>. Amyloid fibrils (either ex vivo or in vitro) are historically defined by three main criteria: green birefringence upon staining with Congo Red, fibrillar morphology, and  $\beta$ -sheet secondary structure. Moreover, amyloid fibrils have been widely studied both in tissue samples and in vitro studies by the use of fluorescent intercalating agents as Thioflavin T that inserts itself into the grooves formed by side chains of amino acids composing  $\beta$ -sheets <sup>118-120</sup>. The aggregation process is complex and includes different organization states of the proteins, as dimers, trimers, tetramers, soluble and spherical oligomers, linear or annular protofibrils, to reach the final aggregated product which is represented by the mature amyloid fibrils (Fig. 13).

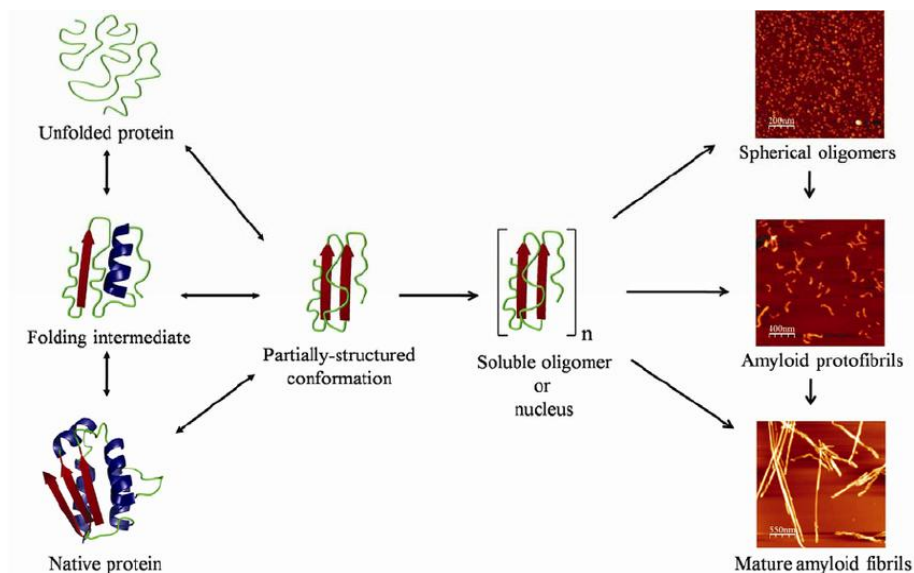


**Figure 13. Protein misfolding and amyloid formation.** Amyloid fibril formation starts from partially (un)folded conformers, which can form by partial unfolding of globular proteins, partial folding of natively unfolded proteins, or by conformational change in folding intermediates. The conversion of partially structured conformations into fibrils occurs through pre-fibrillar aggregates (spherical oligomers and/or protofibrils). The scale bars in AFM images of spherical oligomers, protofibrils and mature fibrils are, respectively 200, 400 and 550 nm. *From Kumar et Udgaonkar, 2011* <sup>121</sup>.

Several studies have been highlighted the involvement of lipid rafts in the pathological aberrant protein misfolding and aggregation at several levels. Moreover a great amount of data suggest that the interaction of misfolded protein species with the membrane, especially with lipid rafts, is one of the key event that cause neurotoxicity <sup>122</sup>. The use of model membranes for the investigation of the relation between amyloid proteins and lipid membranes has provided information about the mechanisms controlling the aggregation, the structure of aggregated species and the interaction with the cell membrane <sup>123</sup>. For that reason we present here a particular case study, focusing on the interaction of alpha synuclein ( $\alpha$ S), the central protein of Parkinson's disease, with artificial lipid bilayers. Despite the comprehension of this disease overall retains many unclear points, there is a substantial evidence that binding of  $\alpha$ S aggregates with the lipid membrane represents a relevant factor for neurotoxicity and development of this neurodegenerative disease.

#### **4.1 Parkinson's disease**

Parkinson's disease (PD) is one of the most common neurodegenerative disorder with increased prevalence at late age, affecting more than 1% of population over the age of 60 and 4% at the age of 80 years. Neurologically, PD is characterized by the loss of the integrity of dopaminergic neurons in *substantia nigra pars compacta* (SNPC), the area of the brain involved in the activation of the movements <sup>124</sup>. Although the exact mechanisms underlying the loss of dopaminergic neurons are still under debate, clinically this impairment culminates in different motor symptoms, such as slowed movements (bradykinesia), tremors, loss of automatic movements, rigid muscles and postural instability <sup>125-127</sup>. In addition, PD pathology of SNPC is always accompanied by disorders of other areas of central nervous systems (CNS) which can lead to other clinical symptoms, as cognitive impairment, gastrointestinal dysfunctions, sleep disorders and olfactory dysfunctions <sup>128</sup>. The main neuropathological hallmark of PD is the presence of cytoplasmic fibrillar inclusions called Lewy body. These abnormal aggregates are composed by amyloid fibrils of  $\alpha$ S associated with other proteins such as ubiquitin and neurofilament proteins <sup>129,130</sup> (Fig. 14).

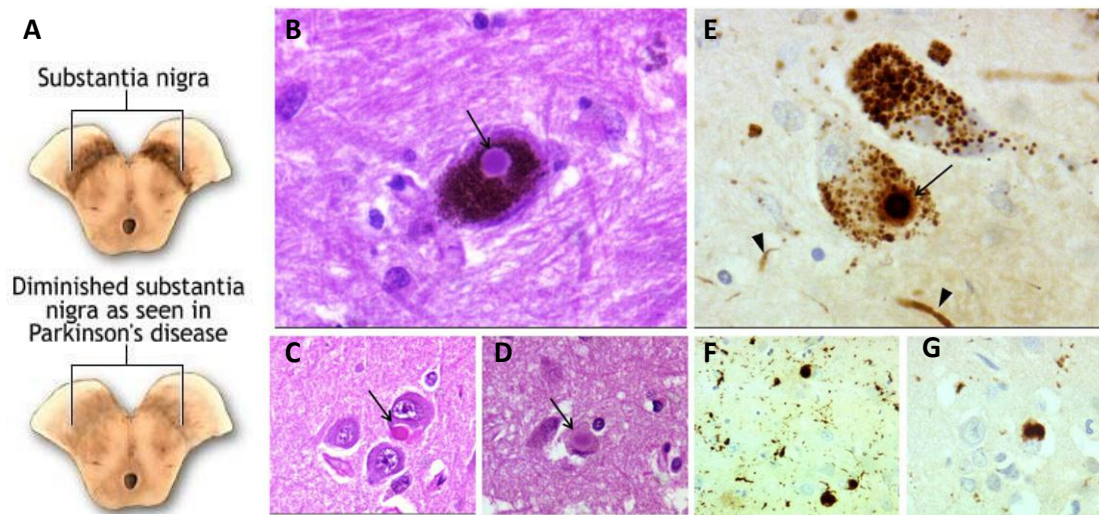


**Figure 14. Neurodegeneration of SNPC and Lewy bodies neuropathology.** (A) Parkinson's disease is characterized by alteration of SNCP. The loss of dopaminergic neurons is evident in post-mortem brains of PD patients as a depigmentation of this area. Lewy body in a neuron of the SNPC (B), in a pyramidal cell of the hippocampus (C), and in cingulate cortex (D) (arrows). (E) Lewy body (arrow) and Lewy neuritis (arrowheads) in the SNPC. (F,G) Cortical Lewy bodies. (B–D) hematoxylin–eosin staining; (E–G) anti- $\alpha$ -synuclein immunostaining. From Taipa et al, 2012<sup>131</sup>.

PD is considered a sporadic chronic disorder for 90% of cases, even though the causes are unclear with a possible role of the exposure to chemicals and a toxic environment<sup>132</sup>. The remaining 10% of cases is familial and a genetic correlation with the development of the disease was identified<sup>133</sup>. It has been discovered that DNA sequence variants lead to rare familial forms of the disease. Sporadic and familial forms of PD have many clinical and pathological aspects in common, as mitochondrial dysfunction, protein phosphorylation, oxidative stress, protein misfolding and impairment of the ubiquitin proteasome system (UPS). The first evidence of genetic contribution in the onset of PD have been reported in the 1997, with the discovery of a point mutation in the  $\alpha$ S gene (*SNCA*), the Ala53Thr (A53T), in members with a familial autosomal dominant PD history<sup>134</sup>. In addition, other several point missense mutations of *SNCA* gene, linked with PD, have been later discovered. These comprise A30P, E46K, H50D, G51D and A53E, highlighting the role of  $\alpha$ S in the initiation and development of PD<sup>135–140</sup>. Several other genes have been implicated in the disease, involving both dominant and recessive mutations. In particular, mutations in the leucine rich repeat kinase 2 (*LRRK2*) act in an autosomal dominant manner, whereas parkin, PTEN-induced putative kinase 1 (*PINK1*), *DJ-1*, are autosomal recessive genes. Defects in the ubiquitin carboxyl-terminal esterase L1 (*UCHL1*) gene were observed only in one case of familial PD and its correlation with the disease is still unclear<sup>141,142</sup>. Interestingly, PD was also associated with structural *SNCA* aberrations, i.e. duplications and triplications, suggesting that increased levels of  $\alpha$ S can promote its pathological aggregation leading to toxicity and resulting in disease conditions<sup>143,144</sup>. Transgenic animal models, expressing high levels of human *wild-type* or

mutant forms of  $\alpha$ S, have showed the formation of lesions very similar to those found in PD patients, providing evidence of the central role of  $\alpha$ S aggregates in the pathogenesis of PD<sup>145-148</sup>. For that reason much greater efforts have been carried out for studying the  $\alpha$ S in term of its biological functions, mechanisms and factors which are involved in its aggregation and its connection with the disease.

## 4.2 Alpha synuclein

Human alpha synuclein is a 140 amino acids (14.460 Da) protein codified by the *SNCA* gene and abundantly localized in neurons at presynaptic terminals<sup>143,149</sup>. It is considered an Intrinsically Disordered Protein (IDP) and lacks a defined secondary structure in solution. This characteristic is presumably due to the aminoacidic composition of the protein that has a high negative charge at neutral pH and low hydrophobicity<sup>150</sup>. The primary sequence of the protein can be divided into three main regions (Fig. 15):

- N-terminal tail (residues 1-60) which is composed by imperfect repetition of 11 amino acids, with a highly conserved hexameric motif (KTKEGV). It is predicted to form amphipathic  $\alpha$ -helices, similar to those of lipid-binding domains of apolipoproteins<sup>151,152</sup>.
- Central hydrophobic domain (NAC, residues 61-95) which is responsible for  $\alpha$ S aggregation and formation of  $\beta$ -sheet rich amyloid filaments<sup>153,154</sup>.
- C-terminal region (residues 96-140), that is rich in acidic residues and can block fibril assembly<sup>155</sup>.

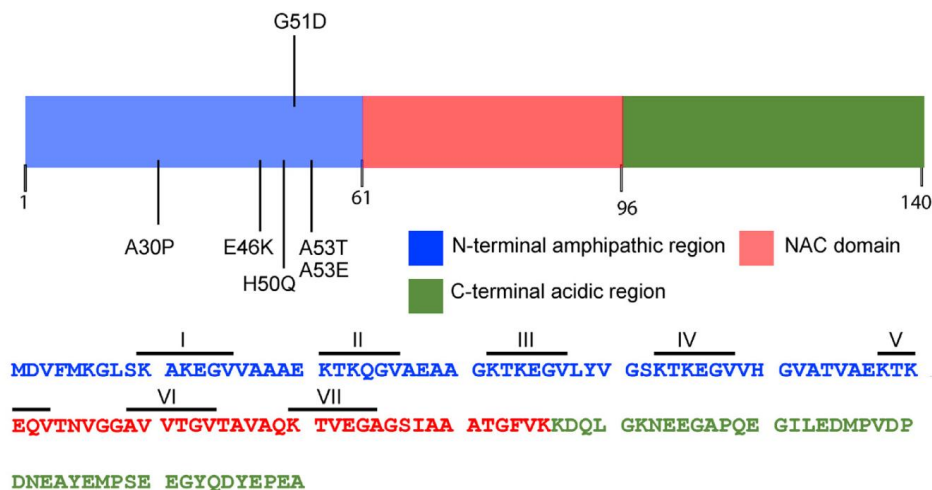


**Figure 15. Primary structure of  $\alpha$ S and position of mutations involved in PD.** The N-terminal domain, the central hydrophobic NAC region and the C-terminal tail are shown. The imperfect hexameric sequences (KTKEGV) are marked by roman numbers (I-VII) in the primary protein sequence. Arrows indicate point missense mutations associated with familiar PD cases. From Ghosh et al, 2017<sup>156</sup>.

In spite of several published studies, its biological function remains still controversial. Besides its involvement in the Parkinson's disease, a key role for  $\alpha$ S in different cellular processes have been proposed. The main function attributed to  $\alpha$ S is to support neurotransmitter release and to modulate vesicle trafficking at neuronal synaptic terminals (Fig. 16). The neurotransmitter secretion from presynaptic vesicles is strongly regulated by the activity of membrane fusion proteins, as SNARE proteins. With its chaperone activity,  $\alpha$ S maintains the SNARE structure during the assembly/disassembly cycle of presynaptic vesicles. During the assembly step, unfolded cytosolic  $\alpha$ S monomers bind presynaptic membrane turning into  $\alpha$ -helix conformation and leading to neuroprotection <sup>157,158</sup>. Moreover, binding to the membrane,  $\alpha$ S modulates the vesicle trafficking by reducing both the amount and the speed of vesicle recycling from synapses to the presynaptic area <sup>159</sup>.  $\alpha$ S is also involved in the regulation of dopamine (DA) biosynthesis. In vitro studies have been suggested that  $\alpha$ S downregulates the enzyme tyrosine hydroxylase (TH), the rate limiting enzyme in the synthesis of DA <sup>160</sup>. Moreover,  $\alpha$ S can modulate DA uptake. DA uptake is due to the activity of the membrane protein dopamine transporter (DAT), which performs the re-uptake of DA from the synapse and its delivery back to the presynaptic terminal. In normal brain,  $\alpha$ S controls the level of DA by decreasing DAT activity <sup>161</sup>. On the contrary, in PD brains, the direct binding of  $\alpha$ S to DAT via its NAC sequence leads to the membrane clustering of the transporter inducing an increased uptake of DA in neurons. Therefore,  $\alpha$ S aggregation or reduced expression of the protein can cause cell damage as a consequence of the oxidative stress which is related to DA metabolism <sup>162</sup>. Other functions attributed to  $\alpha$ S are the role in neuronal differentiation by the activation of ERK/MAPK pathways <sup>163</sup>, the maintenance of polyunsaturated fatty acids levels <sup>164</sup>, and the suppression of apoptosis in dopaminergic neurons by reducing the protein kinase C activity <sup>165</sup>.

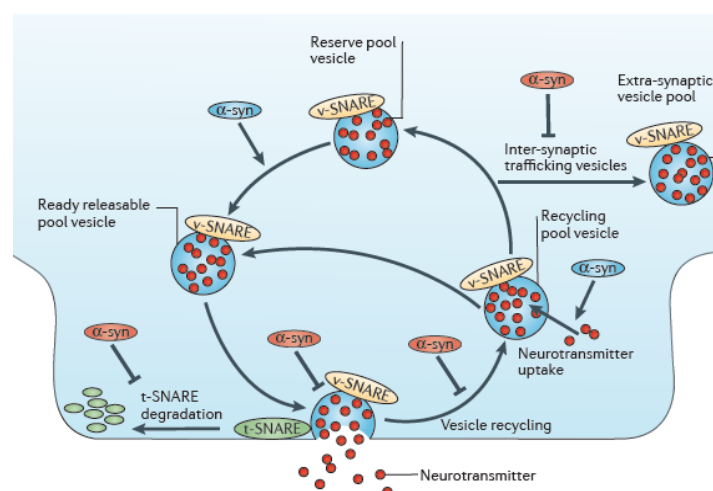


**Figure 16. Schematic representation of  $\alpha$ S functions in regulating synaptic vesicles dynamics.** At presynaptic terminals,  $\alpha$ S regulates vesicle trafficking and refilling, as well as, it interacts with SNARE proteins (t-SNARE and v-SNARE) on vesicles enhancing neurotransmitter release ( $\alpha$ S blue). Accumulation of  $\alpha$ S impairs vesicle recycling and trafficking influencing the stability of SNARE-assembly complex ( $\alpha$ S red). From Lashuel et al, 2012 <sup>166</sup>.

### 4.3 Alpha synuclein aggregation pathway

One of the key molecular event involved in the pathogenesis of PD is the aberrant misfolding and aggregation of  $\alpha$ S<sup>167</sup>. There are different  $\alpha$ S aggregates that have been associated with the pathogenesis of PD, including oligomers, protofibrils, and fibrils (Fig. 17). Several studies have been performed for investigating the  $\alpha$ S aggregation and the mechanisms which are at the basis of this pathogenic process. Typically, the unstructured  $\alpha$ S is able to self-assemble *in vitro* into highly ordered aggregates, giving rise to amyloid fibrils, which are the main components of Lewy bodies in dopaminergic neurons and the neuropathological hallmark of PD<sup>168,169</sup>. Thus, it has been shown that the fibrillar forms obtained *in vitro* resemble the fibrils extracted from the brain of PD patients<sup>169,170</sup>.

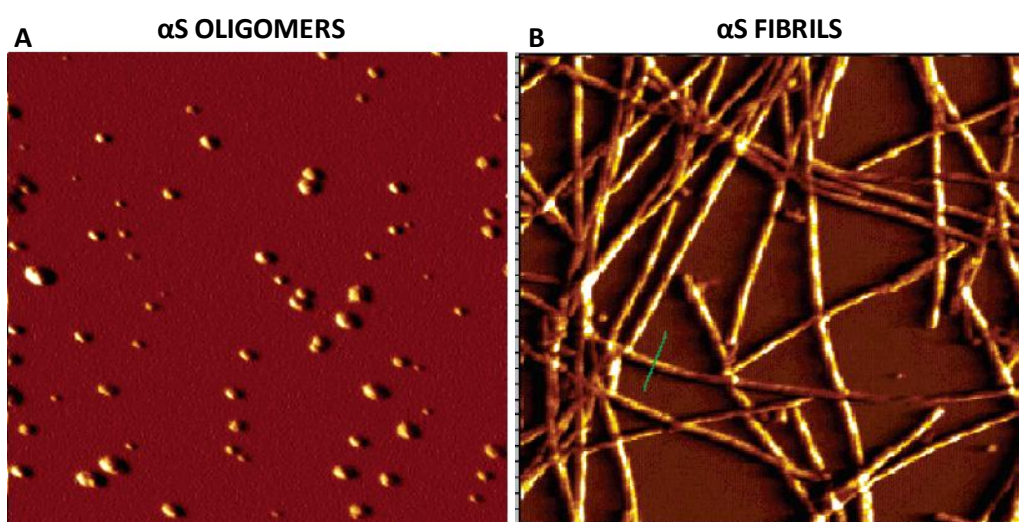


**Figure 17. Atomic Force Microscopy images of  $\alpha$ S oligomers (A) and fibrils (B).** The oligomers are 5-7 nm in height. The fibrils show the characteristic twist of mature fibrils and are 10 nm in height. The images are 3  $\mu$ m square. Adapted from Fink, 2006<sup>171</sup>.

Although several factors have been shown to promote *in vitro* aggregation and fibrillization of  $\alpha$ S (pH, temperature, membrane-binding, metal ions), many aspects are still unknown and the entire biochemical process seems to be highly complex. The abnormal aggregation and accumulation of  $\alpha$ S starts from a partially folded intermediates which contain hydrophobic patches on its surface enhancing hydrophobic interactions between molecules involved in the aggregation process<sup>172,173</sup>. These interactions can form an amyloidogenic nucleus which recruits soluble protein to form fibrils<sup>169</sup>. During the aggregation process,  $\alpha$ S undergoes a change in the secondary structure from an unfolded random coiled into a  $\beta$ -sheet structure in which  $\beta$ -strands are perpendicular to the main axis of the fibril<sup>171</sup>. *In vitro* aggregation of  $\alpha$ S follows a typical nucleation-dependent

model and the entire kinetics can be measured by Dynamics Light Scattering, Fourier Transform Infrared Spectroscopy (FTIR) and Fluorescence Resonance Energy Transfer (FRET) measurements<sup>171,174</sup>. The aggregation process is characterized by an initial lag phase, where transient early stage  $\alpha$ S aggregates, called oligomers, are observed (Fig. 18 A). Several oligomeric species of different morphologies, including spherical, chain-like, and annular oligomers, have been observed prior to  $\alpha$ S fibril formation<sup>175</sup>. Usually, their concentration grows up to 15-20% at the end of the lag phase, and rapidly decrease as soon as fibril growth proceeds during the elongation phase. The final phase is called stationary phase and the fibrils formed remain in equilibrium with the soluble proteins<sup>171</sup>. The entire process is known as primary nucleation and is strictly concentration-dependent (Fig. 18 B). An increase of the concentration of  $\alpha$ S in solution enhances the rate of fibrillization<sup>176</sup>. In addition, it has been discovered that mature fibrils can even trigger a secondary nucleation process. This process is characterized by the fragmentation of the pre-formed fibrils leading to an increased number of ends for fibrils elongation as well as the interaction of monomers with the surface of fibrils (Fig. 18 B)<sup>177</sup>.

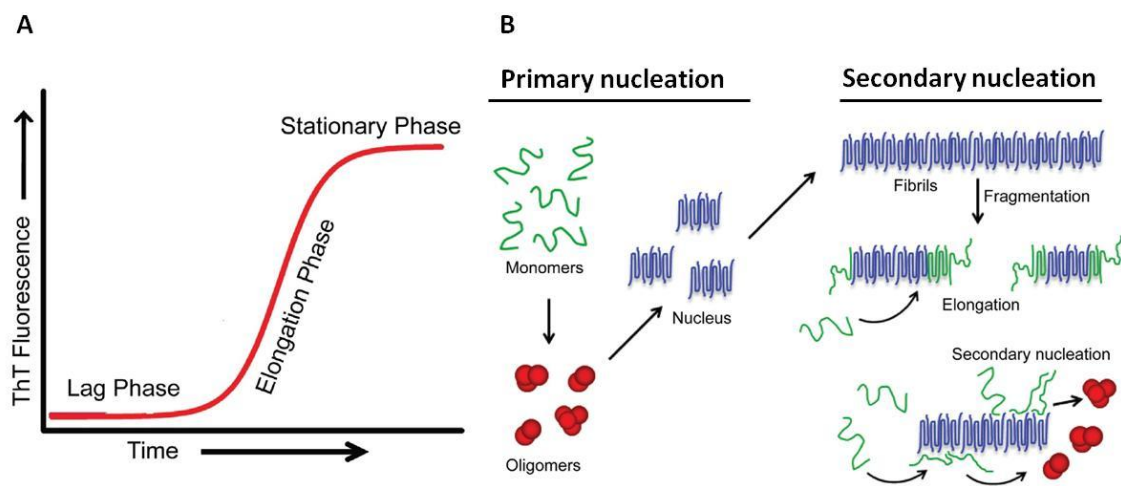


**Figure 18. Aggregation pathway of  $\alpha$ S.** (A) Sigmoidal growth curve of formation of  $\alpha$ S fibrils with the three distinct phases (lag phase, elongation phase, stationary phase). (B) Schematic illustration of primary and secondary aggregation pathway of  $\alpha$ S. Adapted from Ghosh et al 2017<sup>156</sup>.

Genetic mutations associated with familial PD can alter the aggregation kinetics of the protein as well as the propensity to form fibrils and/or oligomers. The mutant A53T, as well as the E46K species, display an accelerated fibril formation whereas the mutant A30P shows an enhanced oligomer formation and a decreased fibril-formation rate compared to the wild type  $\alpha$ S<sup>178-180</sup>. Several mechanisms have been proposed for explaining the different aggregation behavior of the mutant  $\alpha$ S species. They include modifications of the physicochemical properties and the secondary protein structure affecting the intra-molecular interactions and, therefore, the

formation of the hydrophobic patches on the surface of the protein. Despite the aggregation process of wild-type  $\alpha$ S and the mutant species has been extensively studied in different conditions both *in vivo* and *in vitro*, the exact structure of the aggregated species which are responsible for the neurodegeneration in PD remains not totally clear. Recently, it has been highlighted that the oligomers represent the main protein toxic species which contribute to the development and the pathogenesis of PD<sup>181</sup>. The role of oligomers in neuronal dysfunctions, cytotoxicity and cell death is referred as “oligomers hypothesis”<sup>182–184</sup>. Strong indirect evidences support the existence of various  $\alpha$ S oligomeric species *in vivo* under pathophysiological conditions. SDS-resistant dimers, low and high molecular weight oligomers have been detected in the brain of PD patients and in brains of transgenic animal models of synucleinopathies<sup>147,185,186</sup>. Accumulation of  $\alpha$ S oligomers has been shown to alter membrane permeabilization<sup>187</sup>. Moreover, it has been demonstrated that in transgenic mice overexpressing  $\alpha$ S the accumulation of oligomers was associated with the loss of several presynaptic proteins, resulting in the disruption of the synaptic vesicles and eventual neurodegeneration<sup>188,189</sup>. Conversely,  $\alpha$ S amyloid fibrils also play a role in the spread of the disease. Exogenous added of  $\alpha$ S fibrils can penetrate inside the cell and promote the aggregation of endogenous  $\alpha$ S into Lewy body-like cytoplasmic inclusions<sup>190,191</sup>. So, the necessity to better understand the mechanisms that trigger the toxicity and the role of the different  $\alpha$ S protein species is essential for the development of therapies against PD.

#### 4.5 Alpha synuclein interaction with biological membranes

Interaction of  $\alpha$ S with biological membranes has been extensively studied using both cellular and model membrane systems, being  $\alpha$ S-lipid interactions one of the key factors that can trigger  $\alpha$ S aggregation<sup>123,192</sup>. It has been demonstrated that lipid-binding by  $\alpha$ S is one factor that can increase several-fold the protein aggregation<sup>193–199</sup>. The binding of monomeric  $\alpha$ S to a membrane requires two steps, involving the N-terminal tail and the hydrophobic NAC region. After the first anchoring of the N-terminal domain to the membrane,  $\alpha$ S undergoes a structural transformation to  $\alpha$ -helix. During this process the C-terminal domain displays only weak interactions with the membrane<sup>200–202</sup>. NMR spectroscopy experiments performed with micelle-bound  $\alpha$ S have suggested that the first 100 residues of  $\alpha$ S are directly involved in the interaction and form two curved helices, the helix N (residues 3–37) and helix C (residues 45–92) with a linker represented by residues 38–44, maintaining the C-terminal tail unfolded<sup>203</sup>. Several studies performed on artificial lipid bilayers containing biologically relevant lipid molecules have demonstrated that  $\alpha$ S exhibits preferential binding for negatively-charged phospholipids such as phosphatidylinositol (PI), phosphatidylglycerol (PG) and phosphatidylserine (PS)<sup>204,205</sup>. This protein behavior is related to the presence of positively-charge lysine residues in the N-terminal tail, promoting electrostatic

interactions with the negatively-charge membrane surface <sup>203</sup>. In general, lipid composition and physical properties of membranes, as charge, curvature and packing defects, are the main factors that modulate lipid-binding properties of monomeric  $\alpha$ S <sup>206,207</sup>. Moreover, missense mutations that cause rare inherited forms of PD can alter the membrane binding ability of  $\alpha$ S. For example, the mutant A30P and A53E are characterized by a weaker interaction with the membrane, whereas A53T and E46K show higher membrane-binding propensity <sup>180,208</sup>. Membrane-binding is facilitated by lipids with small headgroup and polyunsaturated chains because they are responsible of a less packing of the bilayer, leaving more defects available for  $\alpha$ S insertion in membrane <sup>209,210</sup>. Moreover, the curvature of lipid membrane seems to be crucial in  $\alpha$ S membrane-interaction. Monomers exhibit a preference binding for small unilamellar vesicles (SUVs, 10-100 nm in diameter), due to the higher membrane curvature than large unilamellar vesicles (100 nm - 1  $\mu$ m in diameter) <sup>211,212</sup>. For this reason, complementary measurements with different surface techniques on planar supported lipid bilayer could elucidate the role of  $\alpha$ S-lipid membrane interaction removing the contribution of membrane curvature.

According to the physiological function of  $\alpha$ S in presynaptic vesicles,  $\alpha$ S interaction/colocalization with gangliosides (GMs) have been described using circular dichroism (CD) spectroscopy and molecular simulations <sup>213,214</sup>. GMs are glycosphingolipids composed of a ceramide backbone and one or more sugars as headgroup and are supposed to bind  $\alpha$ S through the formation of hydrogen bonds between sugar alcohols and  $\alpha$ S side chains <sup>214</sup>. The ganglioside GM1 is enriched into lipid rafts, liquid-ordered domains of cell membranes, and involved in many cellular processes. A study has demonstrated that, in HeLa cells,  $\alpha$ S colocalizes with GM1, supposing that this interaction is essential for synaptic localization of the protein. The same procedures have been performed on the detergent resistant membranes extracted by HeLa cells and supposed to be raft domains of the cell, demonstrating  $\alpha$ S association <sup>213</sup>. The situation is anyway controversial and the binding of  $\alpha$ S to lipid rafts is still under debate.

As for native  $\alpha$ S, several studies have been concentrated in elucidating the activity of aggregated species of  $\alpha$ S in the binding of biological membranes. Especially oligomers activity has been extensively investigated, being considered the protein intermediates which display neurotoxicity and membrane perturbation in PD <sup>215</sup>. As with monomers, the N-terminal domain plays a key role in the interaction of oligomers with lipid bilayers. Deletion of amino acidic residues 2-11 suppresses oligomers interaction with LUVs <sup>216</sup>. Oligomers show preferential affinity for liquid-disordered phases of membranes and in general they display much more affinity for biomembranes compared to monomers, without being affected by high membrane curvature or packing defects <sup>217,218</sup>. The cellular disfunctions caused by the interactions of oligomers with biological membranes are due to the destabilization and permeabilization of the membrane by the protein, which lead to alteration of the calcium flux, dispersion of intra-vesicular dopamine

and depolarization of mitochondrial membrane, all phenomena potentially involved in PD<sup>215,219</sup>. Different mechanisms of membrane permeabilization have been proposed for  $\alpha$ S oligomers, and comprise membrane disruption, generation of membrane pores and lipid-extraction from the bilayer (Fig. 19). Several evidences based on electrophysiology, vesicle dye leakage assay and atomic force microscopy, have demonstrated the existence of a membrane pore-like mechanism by  $\alpha$ S oligomers<sup>220,221</sup>. Soluble  $\alpha$ S oligomers obtained by cold-induced dissociation of amyloid fibrils have been shown to form cation-selective pore-like channels in a variety of planar lipid bilayers (for instance PC and PC/PS) in the presence of a trans-negative potential<sup>222</sup>. Similar results have been observed with iron-induced  $\alpha$ S oligomers<sup>124</sup>.

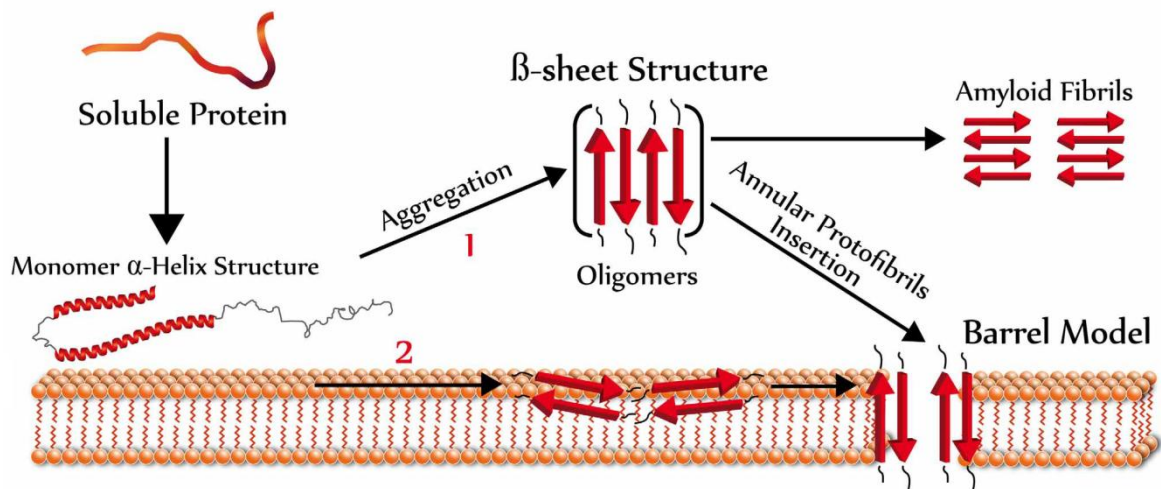


**Figure 19. Barrel model for  $\alpha$ S oligomer pore formation on lipid membrane.**  $\alpha$ S oligomers, enriched in  $\beta$ -sheet structures, form ring structures with a central pore. The oligomers could occur in the extracellular space (1) or at the plasma membrane (2). From Pacheco et al, 2012<sup>223</sup>.

#### 4.6 Alpha synuclein and metal ions in Parkinson's disease

In addition to membrane-binding, some studies have been focused on the relation between PD progression and metal ions such as iron, copper and other biologically relevant metals. Based on epidemiological studies, exposure to specific metals has been considered a risk factor for PD<sup>224-226</sup>. Elevated concentrations of several different metals have been found in the brain of PD patients. In details, biochemical analysis of Lewy bodies in SNPC of PD brain has revealed high levels of iron and aluminum as well as a decrease in  $\text{Fe}^{2+}/\text{Fe}^{3+}$  ratio and an increase in the ferritin, a  $\text{Fe}^{3+}$ -binding protein<sup>227-229</sup>. Several studies have demonstrated the effect of different metal ions in promoting the in vitro aggregation of  $\alpha$ S, by the initial formation of stable protein-metal complexes which lead to the exposure of hydrophobic patches on the surface of the protein, enhancing the aggregation process<sup>230</sup>. These metal-protein products have been characterized by

Nuclear Magnetic Resonance (NMR) spectroscopy, highlighting the presence of metal-binding sites mainly located at C-terminal domain of  $\alpha$ S<sup>231</sup>. The mapping of this region has identified three amino acidic residues, Asp121, Asn122, Glu123, which are involved in the binding of many different metal ions with very low selectivity. Moreover, a weak metal-binding site is also present at the N-terminal tail of  $\alpha$ S, but there is a general consensus that the metal-induced  $\alpha$ S aggregation involves exclusively the C-terminal domain of the protein<sup>231</sup>.

Particularly interesting is the role of iron and globally the cell iron homeostasis that is now accepted as one of the factors that is involved in the neurodegeneration of PD. It has been demonstrated that iron is accumulated at high concentration in the brain of PD patients and that its amount strongly correlates with disease stage and severity<sup>232,233</sup>. Beside the effect of iron in promoting in vitro aggregation of  $\alpha$ S, the role of iron in the pathogenesis of PD is also related to the redox chemistry supported by the metal. Iron is involved in the production of the reactive oxygen species (ROS), and pathological iron accumulation promotes oxidative stress and neurotoxicity leading protein aggregation, glutathione consumption, lipid and nucleic acid modifications<sup>234</sup>. Several experimental evidences have shown that iron and  $\alpha$ S display a strong interconnection in cell, nevertheless it is not clear whether iron triggers  $\alpha$ S aggregation or if increased levels of the protein lead to iron accumulation. Neurons over-expressing  $\alpha$ S have been shown to display increased iron levels compared to cells expressing basal levels of the protein<sup>235</sup>. At the same time, it has been demonstrated that treatment of cell cultures overexpressing- $\alpha$ S with an excess of iron stimulates the formation of  $\alpha$ S aggregates. As expected, the aggregation of  $\alpha$ S is dependent on the amount and the species of protein expressed<sup>236</sup>. Moreover, it has been shown that  $\alpha$ S RNA sequence contains an iron-response element (IRE) binding site in its 5'-untranslated region, highlighting that iron can control the expression of the protein at translational level<sup>237</sup>. This finding strengthens further the pathological interplay between iron and  $\alpha$ S in the neurodegeneration of PD, opening to new therapeutic approaches that can target the iron amount in neurons.

## **5. Artificial model membranes: a great tool for studying lipid raft domains**

Biological membranes display a huge complexity and dynamism being composed by more than one thousand different lipid species and several kinds of membrane proteins. The existence of lipid domains, lipid asymmetry and the coexistence of phases are some of the reasons why membranes are so extremely complex. Many cellular processes depend on the ability of the membrane to compartmentalize different areas, regulating the communication between the

extracellular environment and the cytoplasmic side. The difficulty of studying the plethora of biological processes of cell membranes in real-time in living systems has been motivated the development of a wide variety of different artificial model systems which mimic the situation of a real membrane in terms of lipid composition and membrane asymmetry<sup>238</sup>. Particularly, the study of lipid rafts represents a big challenge in membrane biophysics because they are small (10-200 nm) and highly dynamic<sup>22</sup>. Model membranes are very useful tools to chemically and biophysically investigate these functional domains as well as their interactions with other lipids and membrane proteins, revealing functional details that can be transferred to the investigation of real cellular membranes<sup>239</sup>. Several different model systems are available to study lipid phase separation and lipid-biomolecules interactions, displaying advantages and disadvantages according to the purpose for which they are used. Here we report some examples of model membranes together with their biological applications and methods of preparation.

## 5.1 Membrane models

Supported lipid bilayers and liposomes represent the most common artificial membrane systems. Supported lipid bilayer (SLBs) are stable and robust biomimetic model membranes typically made by a single planar lipid bilayer supported onto a clean and solid surface such as mica, glass or quartz<sup>240,241</sup>. They are used to study lipid phase behaviour and lateral organization of biological membranes using the common surface analytical techniques such as atomic force microscopy (AFM)<sup>242</sup>, fluorescence microscopy<sup>243</sup>, infrared spectroscopy (IR spectroscopy)<sup>244</sup>, X-rays and neutron reflectivity<sup>245,246</sup>. They are also suitable for studying lipid-protein interactions and in general interaction of biomolecules with the lipid bilayer. However, the presence of a space that is only 1-2 nm wide between the bilayer and the solid support renders these systems not so suitable for studying transmembrane proteins, which mostly appear immobile in the SLB<sup>247</sup>. For that reason, many modifications of planar SLBs, such as tethered<sup>248</sup> or polymer cushioned lipid bilayer<sup>249</sup>, have been developed in time to expand the biological applications. These systems allow to increase long-term membrane stability and to introduce more space between the bilayer and the solid support in order to better study big transmembrane proteins, avoiding problems of denaturation and interfered mobility along the membrane.

Liposomes are lipidic vesicles formed by the hydrophobic effect when lipids are dispersed in aqueous solution. They are suitable to study membrane phase behavior, and membrane processes such as cell adhesion, membrane pore formation and molecular recognition. They can be prepared as multilamellar (multiple layers) or unilamellar (single layer) by different methods as extrusion, sonication and electroformation<sup>250</sup>. Unilamellar vesicles are easy to prepare and to manipulate and are classified according to their dimensions as small (SUVs, 10-100 nm), large,

(LUVs, 100 nm - 1  $\mu\text{m}$ ) and giant unilamellar vesicles (GUVs, > 1  $\mu\text{m}$ ) (Fig. 20) <sup>251</sup>.

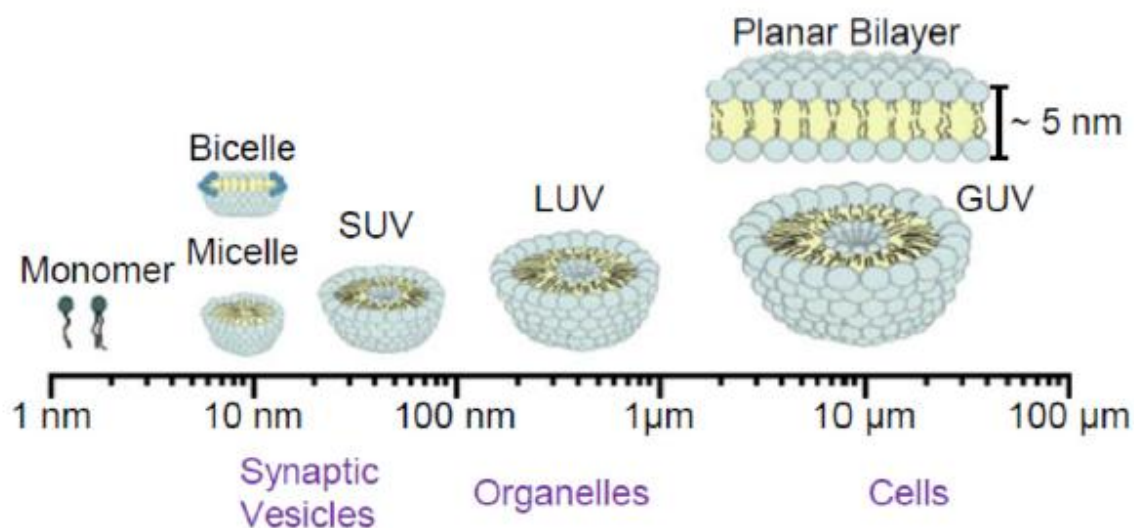


Figure 20. Schematic representation of different model artificial lipid bilayer commonly used in biophysical research and their approximate size. Adapted from Pfefferkorn et al, 2012 <sup>206</sup>.

Generally, different criteria have to be taken into account in the choice of the proper model system. Each model should be chosen considering advantages, disadvantages, the experimental information needed and the feasibility of the experiment <sup>252</sup>. For instance, planar SLBs are more stable than liposomes and are more suitable for studying membrane-active insertion of molecules within the bilayer. Moreover, not all lipid compositions can be represented in liposome system, as a membrane made by only sterols. Finally, the choice of lipid mixture is important because increasing the complexity of the system could be render the biophysical interpretation of results more difficult. It is therefore essential to design the experiments evaluating the balance between its complexity and feasibility <sup>252</sup>.

## 5.2 Model membrane preparations

Planar SLBs can be prepared using different methods. The most useful are briefly described:

- 1. Langmuir-Blodgett (LB)/Langmuir Schäfer (LS).** This technique is a procedure for the fabrication of mono- or multilayer membrane. The apparatus consists in a Teflon bath with moveable barriers. Lipids are deposited at air-water interface dissolved in solvents. The movement of the barriers is used to compress lipids, creating a lipid monolayer called Langmuir film. During the compression of lipids, a pressure vs area isotherm can be

recorded, giving information about the lipid packing (Fig. 21). Usually, the surface pressure of the monolayer is set to the value of 32 nN/m, which matches that of biological membranes.

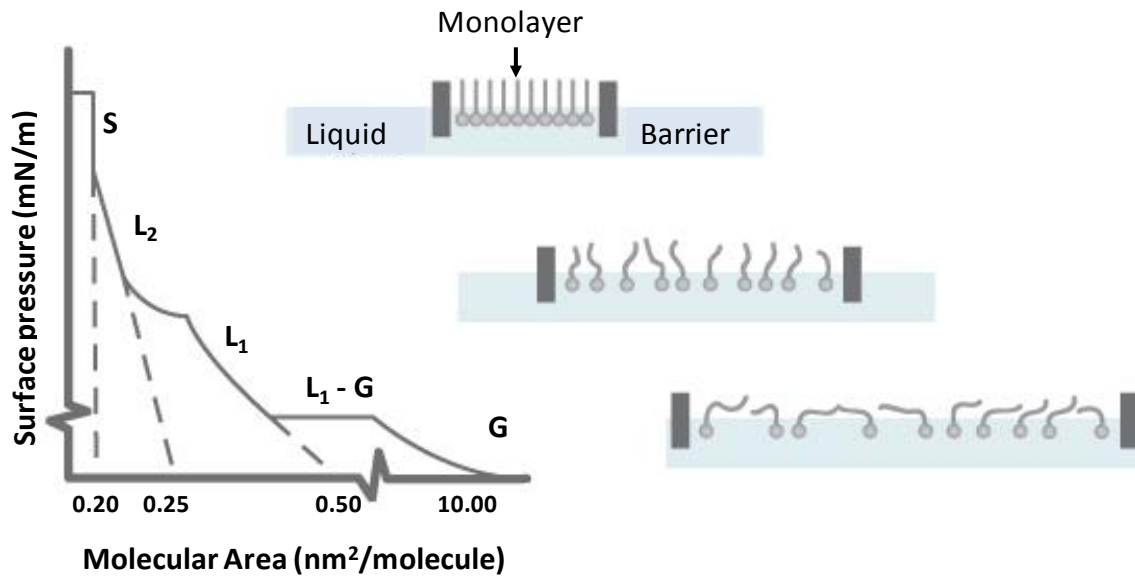


**Figure 21. Theoretical surface pressure vs area isotherm of a Langmuir film and molecules in different phases.** At low pressure, the area covered by lipid molecules is high because of the lack of layer organization (gas phase, G). Increasing the lateral pressure, the molecules start to standing up (liquid phase,  $L_1 - L_2$ ) until the formation of a uniform monolayer (solid phase, S).

The first lipid monolayer is then transferred to the solid support by quickly immersing a clean hydrophilic slide into the water subphase and slowly retracting it through the interface, forming the so-called Langmuir-Blodgett film (in case of vertical deposition) or Langmuir-Schaefer film (in the case of horizontal deposition) (Fig. 22). At this point, it is possible to transfer a second lipid monolayer from the LB trough to the substrate, completing the bilayer formation.

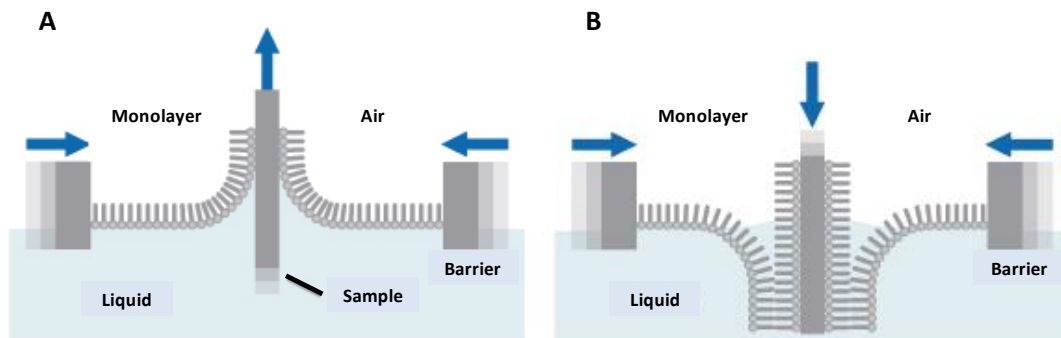


**Figure 22. Schematic representation of Langmuir-Blodgett technique.** (A) After the formation, the first lipid monolayer is transferred to on a solid hydrophilic support moved through the solution with constant lifting speed. (B) A second layer is obtained with the subsequent immersion of the support.

Repeated deposition can be achieved to obtain well-organized multilayers on the solid substrate. LB and LS cycles can also be combined to obtain desired structures and thicknesses. The most common multilayer deposition is the Y-type multilayer, which is produced when the monolayer is deposited in both up and down directions. When the monolayer is deposited only in the up or down direction the multilayer structure is called either Z-type or X-type (Fig. 23).

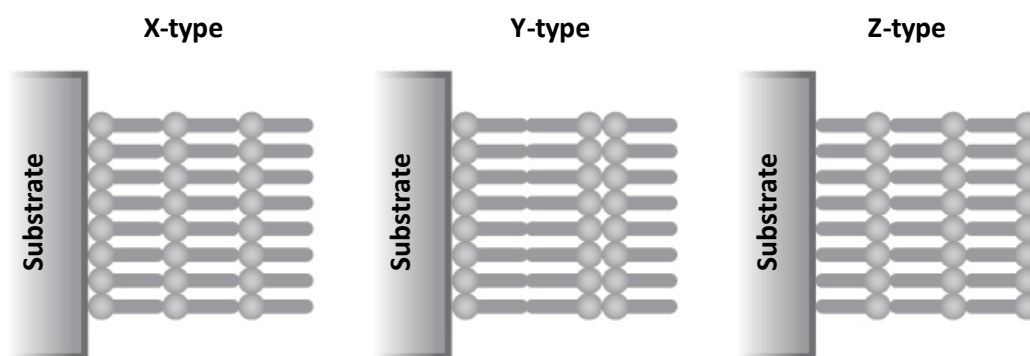


**Figure 23. Three possible lipid membrane configuration using Langmuir-Blodgett technique.** The Y-type represent the typical lipid bilayer, in which the hydrophobic tails of one monolayer are in contact with the tails of another one. The X- and Z-type are characterized by the formation of stacked lipid monolayers in which lipid head groups are in contact with the tails of another monolayer.

The main advantages of LB/LS method is the possibility to produce lipid bilayers that maintain lipid asymmetry for several hours<sup>253</sup>. Moreover, it allows a precise control of the monolayer thickness and packing density<sup>254</sup>. However, the main disadvantage of the process is during the transfer of the monolayer, which can leads to the mixing of the subphases.

**2. Direct vesicle fusion.** It is the most common method to produce SLBs<sup>255</sup>. Typically, SUVs or LUVs of specific lipid composition are placed in contact with a flat and clean hydrophilic surface and after a certain time of incubation (in the range of minutes) the vesicles rupture to form a continuous lipid bilayer, and the excess of vesicles is removed by buffer washing. The fusion of vesicles on the surface is affected by the lipid composition, size, surface characteristics, pH, and ionic strength<sup>256</sup>. The mechanism is not completely understood but it is known that the process involves adsorption of the vesicles on the surface, deformation, flattening and rupture to form a continuous SLB (Fig. 24). The simplicity of the process makes this technique a great approach for producing SLBs of different lipid composition. However, the main disadvantage is represented by the impossibility to produce SLBs with lipid asymmetric composition.

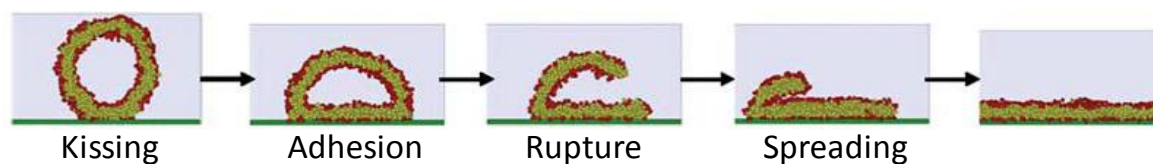


Figure 24. Simulation of vesicle fusion process onto hydrophilic surface. From Wu et al, 2013<sup>257</sup>.

**3. Drop-casting.** Lipids are dissolved in organic solvents such as chloroform, decane, acetone, alcoholic solvents or a mixture of them. Lipid solution is then directly spread on a solid support and let to evaporate favoring the self-assembly of lipids (Fig. 25). The main advantage of this method is that it is easy and fast to be performed, and it does not require any specific instrumentation<sup>258,259</sup>. It is used especially for structural studies by NRM or X-ray scattering experiments because of the multilamellar characteristics of the membrane obtained. However, it is difficult to control the exact number of layers formed and it is not suitable for transmembrane protein incorporation into the bilayer.

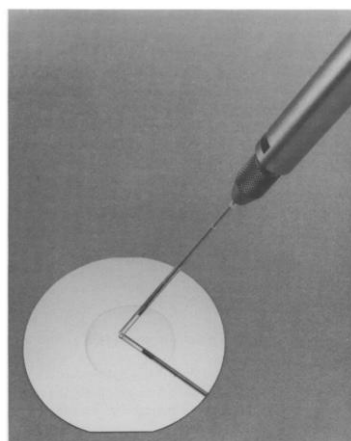


Figure 25. Drop casting of lipid solution. The picture depicts the deposition process of lipids by solution spreading. A syringe is used to deposit a drop of lipid organic solution at the center of a silicon wafer support. From Seul et al, 1990<sup>258</sup>.

**4. Spin coating.** As for drop-casting method, spin coating is characterized by the spreading of lipid dissolved in organic solution on clean solid support. The substrate is then rotated using a spin coater, exploiting the centrifugal forces to obtain a well-oriented lipid film (Fig. 26)<sup>260</sup>. After the evaporation of residual solvent under vacuum, the lipid film is hydrated in a specific buffer. According to the rinsing process and buffer conditions, the membranes obtained are formed by one to three stacked lipid bilayers<sup>261,262</sup>. This method allows the incorporation of peptides or truncated integral proteins but it is not suitable for larger proteins which are denatured in the organic solvent. Recent

evidences have shown that the method can be apply to created membrane with a coexistence of Lo and Ld domains <sup>261</sup>.

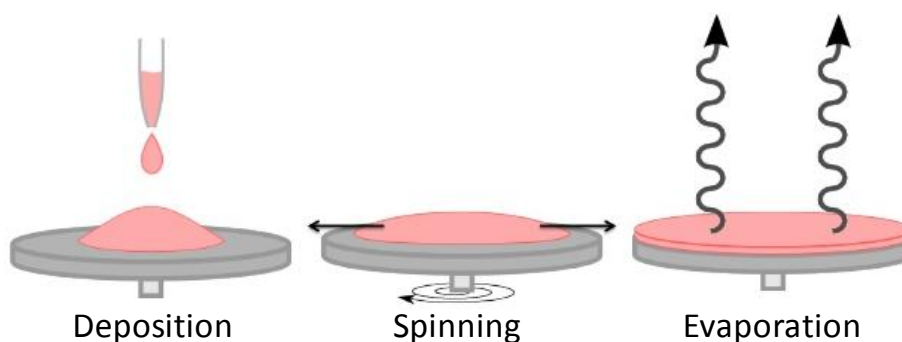


Figure 26. Schematic representation of spin coating procedure for the production of lipid bilayers.

## 6. Analytical techniques to characterized artificial lipid bilayers

Supported lipid bilayers offers practical advantages over liposome systems, allowing the application of a broad group of analytical techniques for characterization, imaging and analysis of these model membrane systems. Among several available techniques, AFM is considered a great and versatile tool to study artificial lipid bilayer. The main advantage of this method is the possibility to performed imaging of a lipid membrane in physiological environment with a nanoscale resolution. At the same time, AFM can provide information about the mechanical properties of the bilayer. Several AFM-based studies has been performed in order to investigate lipid rafts in model membranes and biomolecule interactions with these domains <sup>263,264</sup>. Frequently, AFM is coupled with other techniques, where the high resolution of AFM is combined with the chemical information gained from optical and spectroscopy techniques <sup>265</sup>. Here we report a description of AFM principles together with the different work modalities for the investigation of biological samples.

### 6.1 Atomic force microscopy

The Atomic force microscope (AFM) is a near field surface microscopy technique that was developed by Binnig et al. in 1986 <sup>266</sup>. It belongs to the scanning probe microscopy (SPM) family, a class of instruments that investigate the properties of a sample at or near the surface.

The AFM operates scanning a sharp tip over the surface of a sample and measures the interaction

between the tip and the sample. A typical AFM apparatus is characterized by a tip mounted on the free end of a flexible cantilever which is deflected in response to force changes between tip and the sample. The tip and the cantilever together are often referred to as AFM probe. During scanning the cantilever deflection is registered by the use of laser light that is localized on the upper surface of the cantilever, usually coated with a reflective layer. Change in position of the reflected laser light is recorded by a 4-quadrant photodiode and converted into an electrical signal. These electronic information are subsequently sent to a piezoelectric actuator which moves accurately the AFM probe and the sample in the X-Y plane in a raster manner. The number of lines scanned in a surface unit contributes to the resolution of the image. A Z-actuator, composed by piezoelectric material as well, controls the vertical movement of the tip (Fig. 27).

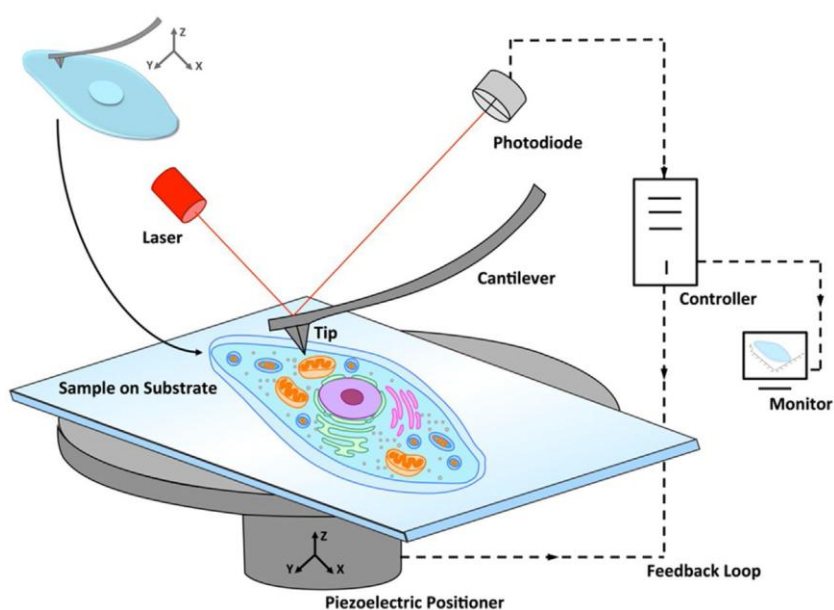


**Figure 27. Schematic representation of an Atomic Force Microscopy used to probe cells and their constituents in three-dimensions.** A laser beam is focused on top of the free end of a cantilever and reflected on a four elements photodiode, sensitive to the laser shifts during the raster-like scanning of the sample. *From Braet and Taatjes, 2017*<sup>267</sup>.

The central component of the AFM is the tip which is typically made of silicon–oxide or silicon nitride and has a radius of curvature of 10 nm for standard probes (Fig. 28 A). Smaller radii of curvature allow reaching higher resolution (Fig. 28 B). For this aim, carbon nanotubes (CNTs) terminated tips have been recognized among alternative choice for AFM probe due to the small diameter (<10 nm), robust mechanical properties and chemical inertness (Fig. 28 C). The soft microsized cantilever has a spring constant that may vary according to the sample and the application (from few tens of pN/nm to few tens of nN/nm),

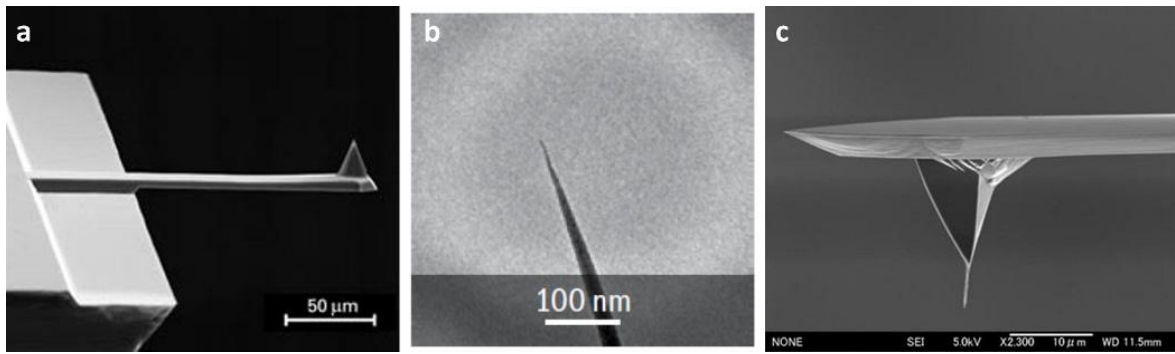


**Figure 28. Scanning electron microscopy of AFM tips. (A)** Example of one standard AFM probe. **(B)** High resolution AFM tip. **(C)** CNT-terminated AFM probe.

Knowing the stiffness of the cantilever, in first approximation, the Hooke's law gives the linearly relationship between the force required to deflect the cantilever and its deformation:

$$F = -kz$$

Where  $F$  is the force,  $k$  is the stiffness of the cantilever, and  $z$  is the distance the lever is bent.

AFM is a very versatile tool for obtaining 3D topographic images of a sample at high spatial resolution. Generally, AFM is able to acquire image data with lateral resolution (in the x-y plane) down to 0.3 nm and vertical resolution (in the z-axis) down to 0.1 nm<sup>268</sup>. Sample preparation for AFM imaging is minimal, without requiring any labeling, fixing or coating treatment. It can operate in air and aqueous environment, making it suitable to study biological samples in physiological conditions. Besides the imaging, AFM allows to quantitatively measure physical properties of a sample such as elasticity, stiffness, adhesion, surface friction, inter- and intramolecular interactions<sup>269</sup>. The AFM can work in different operational modes which differ mainly in the way the tip is moving over the sample. The primary modes of AFM imaging are contact mode and dynamic mode (tapping mode and non-contact mode). In contact mode (or static mode) the probe is maintained in constant contact with the surface of sample. Repulsive forces dominate the interaction between the probe and the sample. In ideal conditions, when the tip starts approaching the surface, long-range Van der Waals interactions predominate; when the tip is near (some Angstroms) to the surface, short-range repulsive forces dominate. From the measure of the cantilever deflection, it is possible to calculate the force of the interaction between the probe and the surface, qualitatively described by the Lennard-Jones potential curve (Fig. 29).

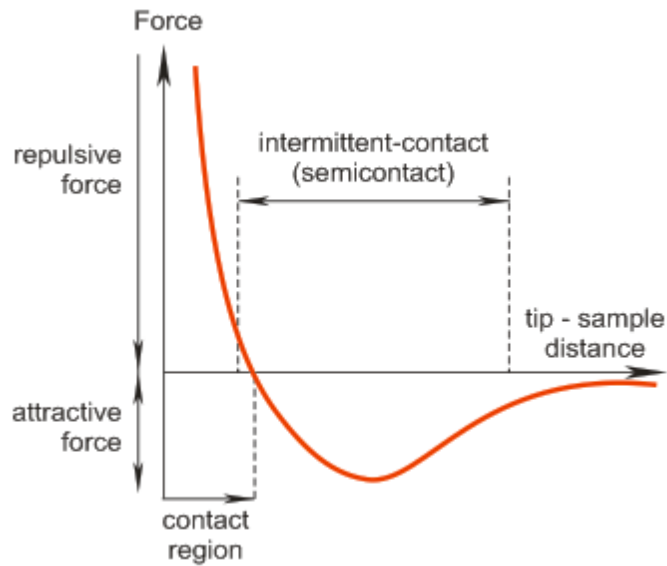


**Figure 29. AFM force-distance curve.** When tip is far from the surface, no deflection occurs. In intermittent-contact the tip is pulled toward the surface (attractive regime). In contact region, the tip is in hard contact with the surface (repulsive regime).

During the scanning, the deflection signal gives the vertical deflection of the cantilever. The error signal is the difference between the deflection signal and the AFM feedback system set-point value, and it is the input to the feedback. The output of the feedback guides the z-actuator, which moves the sample or the probe in the z-axis in order to maintain the interaction with the surface constant. In this way, it is possible to reconstruct the topographic profile of the sample (Fig. 30).

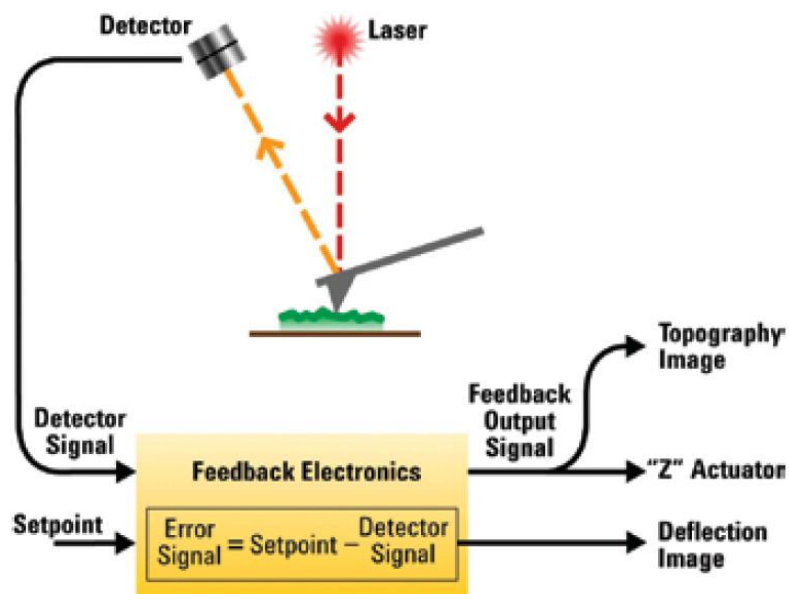


**Figure 30. Schemating diagram of AFM feedback system.** Adapted from "The AFM Almanac", Agilent Technology.

In dynamic mode, the AFM cantilever is driven to oscillate near its resonance frequency. The amplitude of this oscillation is used as feedback parameter for the imaging of the sample.

In Tapping Mode, the amplitude of the oscillation, influenced by long-range forces, controls the feedback system and the error signal (difference between the set-point and the amplitude) is the input for the feedback system. The output controls the z-actuator and the tip movement. Moreover, during the scanning it is possible to record the variation in the phase of the oscillation which can be thought of as a “delay” in the oscillation of the cantilever as it moves up and down in and out of contact with the sample. This signal is particularly useful in the case of a heterogeneous material because it gives information about the chemical properties of the sample, being sensitive to viscoelastic properties and adhesion forces, with little participation by elastic properties. Since the tip touches intermittently the surface, the damage of the sample is significantly reduced. Despite the difficulties of operating in tapping mode in liquid environment due to the significant damping of oscillation frequencies by the viscosity of the aqueous medium, it is widely applied in biology for the study of living cells, lipid membranes<sup>270</sup>, DNA molecules<sup>271</sup> and amyloid fibrils<sup>272</sup>.

In non-contact mode the tip is positioned at a certain constant distance from the surface (within few of nanometers) where attractive forces (electrostatic, magnetic, attractive van der Waals forces) predominate. Once the tip approaches the surface, it starts to feel it. Variations in the resonance frequency, the amplitude and the phase of the oscillation are linked to the characteristics of the surface and to the tip-sample interactions. All these parameters are monitored in order to reconstruct the topography of the sample.

The choice of AFM mode is based on the surface characteristics and on the sample hardness. Contact mode is preferred for hard surfaces, but there is the possibility of tip contamination or damage of the sample. For that reason, in case imaging of biological and soft samples, tapping mode or non-contact mode are favored.

## RESULTS AND DISCUSSION

### 7. Optimization of drop-casting method for the production of complex artificial model membranes

Model membranes represent a very useful tool for investigating the behavior of lipids within the bilayer and, in particular, biological events that take place on plasma membrane and that are difficult to be studied in living systems. Several techniques have been developed for the production of artificial membranes of different lipid composition, such liposome fusion, spin coating and solvent-assisted lipid bilayer formation<sup>239</sup>. The protocol for the formation of an artificial membrane system generally requires reproducibility and a high ratio of advantages over disadvantages. In the first part of my project I worked on the optimization of the drop-casting technique for the fabrication of model membranes containing lipid rafts. I focused on membranes with different lipid composition exploiting different parameters that can affect the quality of the lipid bilayer. Drop-casting is characterized by the spreading of organic lipid mixtures on a clean substrate in order to promote the self-assembly of lipids during the evaporation of the solvent and the consequent formation of SLB. I initially concentrated on the choice of the most suitable solvent, the concentration of lipids and the conditions for sample drying in order to reach the formation of homogeneous, well assembled and reproducible artificial membranes, ideally formed by a single lipid bilayer. Then I increased the complexity of my system by promoting the formation of two-component and three-component membranes with the final aim to produce a model membrane mimicking the presence of lipid rafts.

#### 7.1 One-component lipid bilayers

In the first step I produced one-component membranes made by DOCP. I tested different lipid concentrations and three different solvents in order to obtain a homogeneous membrane characterized by a small number of lipid bilayers. Type of solvents used and lipid concentrations are reported in Table 1. After the spreading of organic lipid solution on a clean substrate, glass in my case, the evaporation of the solvent represents the first critical step for the formation of model membrane of high quality. The drying process is usually performed in a clean cell incubator at a fixed temperature (30 °C) and with high percentage of humidity (80-90%). These parameters show the best results compared to the drying of sample performed at the temperature of the room and without any control of humidity. Another important parameter is

the solvent or the right mixing of different solvents, to prevent too fast desiccation hampering a proper self-assembly of the molecules.

<b>DOPC concentration (mg/mL)</b>	<b>1 0.1 0.01</b>
<b>Solvents</b>	<b>Isopropanol (IPA) Chloroform/Methanol 1:1 Chloroform/Decane 1:1</b>

**Table 1. DOPC concentration and solvents tested for the fabrication of one-component membrane on glass.**

Best results, as evaluated by AFM topography measurements, were obtained with the intermediate concentration (0.1 mg/mL) and with the use of chloroform/decane 1:1 as solvent. The high boiling point of decane (171.5 °C) mixed with chloroform (boiling point = 61 °C) allows in fact a slow evaporation which promotes a complete self assembly of lipids, obtaining a lipid bilayer that homogenously covers the glass support. After sample drying, I characterized the membrane by AFM working in tapping-mode in air at room temperature. AFM images show a discontinuous topmost lipid bilayer of DOPC characterized by an average height of  $5.3 \pm 1.0$  nm (Fig. 31 A-C). In order to quantify the total number of lipid bilayers obtained by this procedure, I used the scratch approach which consists of mechanical removing of all the lipid bilayers leaving only the hard, unstretchable glass substrate as reference. The calculation of scratch depth highlights the presence of a multistacked DOPC membrane, made by multiple lipid bilayers (in the range of 30-40) (Fig. 31 D-E). The use of smaller lipid concentration (0.01 mg/mL or <) produces the formation of small, dispersed and non-continuous lipid patches on the glass, and therefore is not suitable for the production of uniform and regular membrane bilayer (data not shown).

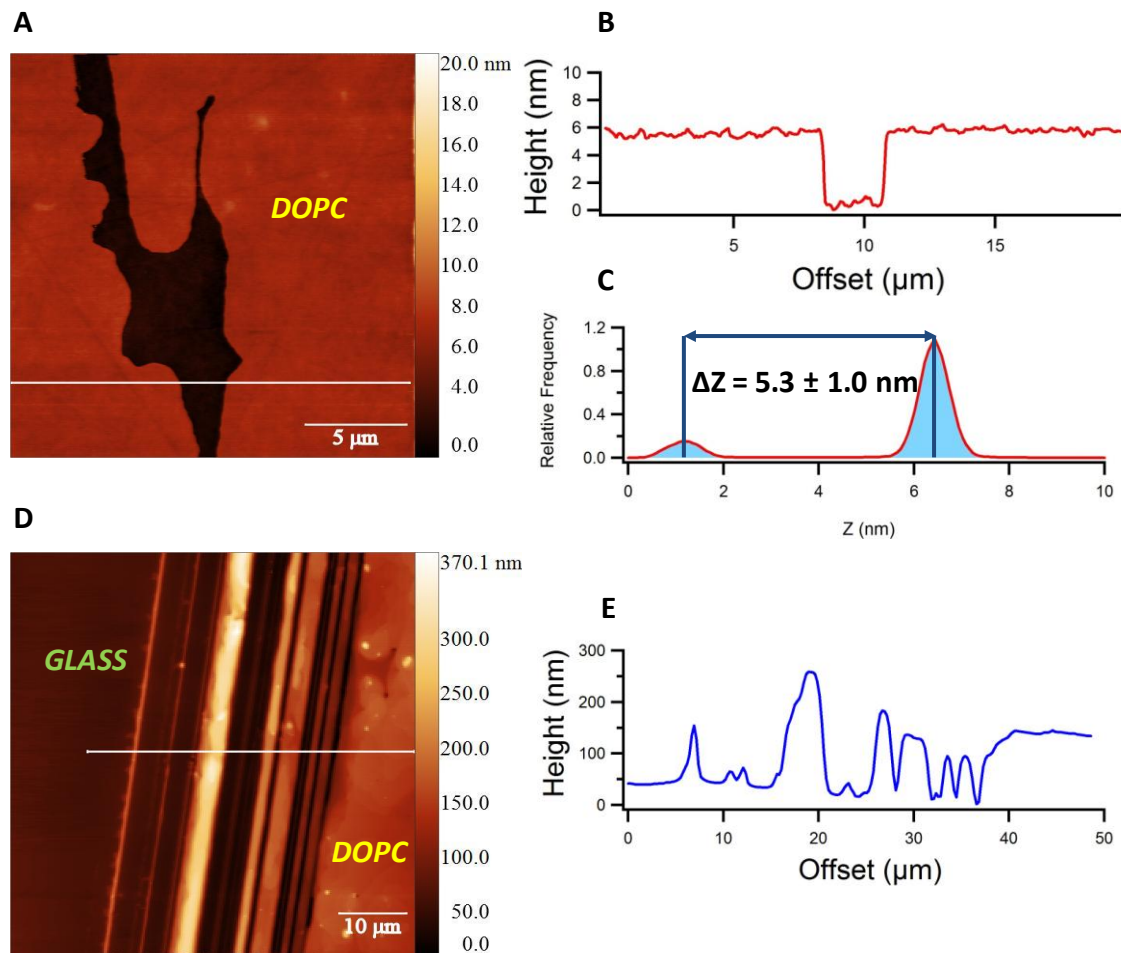


**Figure 31.** AFM images of a DOPC bilayer in air deposited on a glass surface. **(A)** AFM topography of flat lipid membrane with a central discontinuity which allows to measure the height of the lipid bilayer. **(B)** Height profile. **(C)** One DOPC bilayer is characterized by an average height of  $5.3 \pm 1.0$  nm. **(D)** AFM topography of the scratch made by a scalpel. On the right side, a DOPC membrane is present, whereas on the left side glass can be observed. **(E)** Height profile indicates the presence of a membrane formed by 30-40 lipid bilayers. AFM measurements were performed in tapping-mode in air at room temperature.

## 7.2 Two-component membranes

After the determination of the best parameters for the assembly of the membrane, my next step was to move to the production of binary lipid bilayers. I used DOPC in combination with sphingomyelin (SM) and I analyzed the obtained samples by AFM. From this moment on, I worked in a liquid environment in order to move towards more physiological conditions. The membrane was covered with Milli-Q H<sub>2</sub>O and gently rinsed in order to remove the upmost stacking lipid bilayers, ideally remaining with one single lipid bilayer. This model membrane system was built from DOPC and SM in 50:50 molar ratio. DOPC and SM are lipids characterized by different  $T_m$ : at environment temperature the DOPC is expected to be in fluid phase ( $L\alpha$ ) whereas SM is in solid state ( $S_o$ ) (see the extrapolation from the three-component phase diagram

at paragraph 2.1 for zero cholesterol molar concentration). AFM topography confirms this phase-separation picture, showing that the membrane is characterized by two coexisting phases, where the bright domains represent the SM in  $S_o$  phase surrounded by a fluid lipid matrix made by DOPC (Fig. 32 A). The SM domains are 0.2-1  $\mu\text{m}$  in lateral dimension and the height variation ( $\Delta Z$ ) between the  $S_o$  and  $L\alpha$  phase shows that these domains protrude from the fluid environment with an average height of  $1.5 \pm 0.9$  nm (Fig. 32 C). This value is in agreement with the current literature. A previous study on fully-hydrated DOPC bilayer on mica has in fact demonstrated that this one-component membrane has a full thickness of 5 nm<sup>273</sup>. Ovine brain SM phase behavior studied by polarizing light microscopy, differential scanning calorimetry and X-ray diffraction<sup>274</sup> showed that at 25°C, below the phase transition (37 °C), the measured lipid thickness was 6.35 nm. These values support the protrusion of around 1 nm of the SM domains in the fluid DOPC matrix measured in my membranes. However, the two phases appear very rough as in the presence of multiple lipid phases or of non completed phase separation. This effect can be observed in the graph of Fig. 32 C, where height distribution along the entire image (A) is shown. Two broad peaks, with a high error value are shown, indicating the presence of heterogeneous height distribution over the sample.

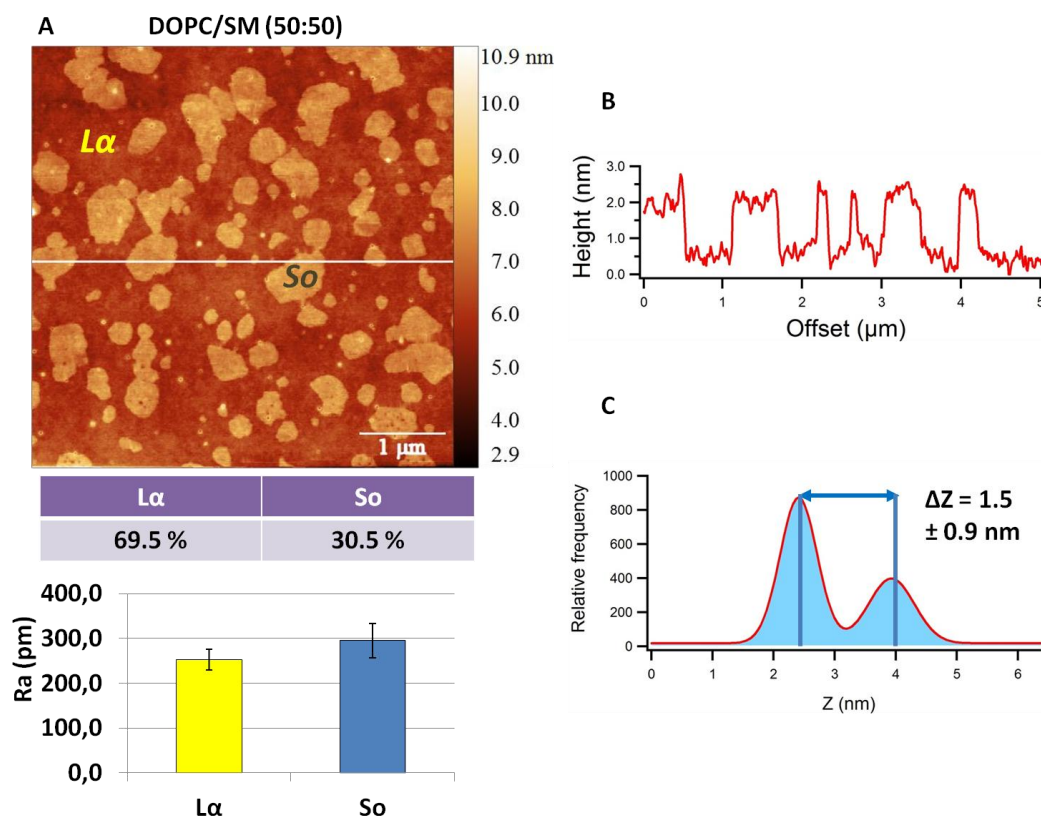


**Figure 32. AFM image of DOPC/SM membrane 50:50 in molar ratio in liquid environment . (A)** The AFM topography shows the presence of two lipid phases, the  $S_o$  (SM) and  $L\alpha$  (DOPC) and the relative ratio. Both phases display high values of roughness (Ra). **(B)** The height profile along the white line in (A) highlights the presence of rough phases. **(C)** Distribution of heights across the entire image (A). AFM measurements were performed in tapping-mode in Milli-Q  $\text{H}_2\text{O}$  at room temperature.

From the area of the two phases in the image of Fig. 32 A I can calculate a relative percentage of the two lipid phases ( $L= 69.5\%$ ,  $S_o= 30.5\%$ ) which does not match with the prediction made from the initial lipid mixture molar ratio (50:50). Imaging several areas on different binary membranes produced in the same conditions, I observed a high heterogeneity in the SM domains, which were characterized by different domain size and morphology, making this model system not so suitable for studying lipid phase behavior (Fig. 33). Therefore we can conclude that the drop-casting method is characterized by scarce reproducibility as well as a poor control of the lipid membrane composition. Clearly, the presence of multiple lipid bilayers before the washing step complicates the scenario and does not ensure to find the same distribution of lipid molecules in each lipid bilayers.

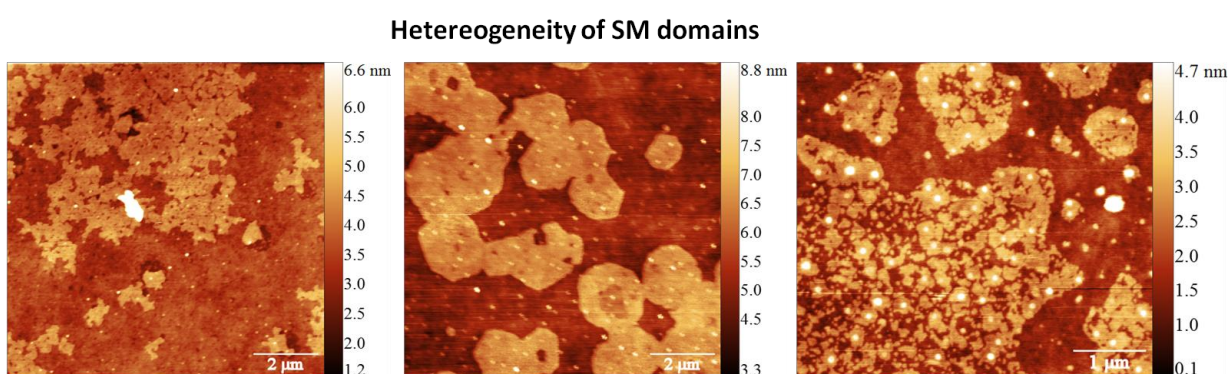


**Figure 33. AFM images of several SM domains in DOPC/SM model membranes.** SM islands have different morphology and cover different areas of membrane.

In order to quantify the thickness of the membrane after the washing treatment, I performed AFM nanoshaving<sup>275</sup>: by means of a hard (spring constant 0.76 nN/nm) silicon-nitride AFM tip, operated in solution at high speed and with the maximum range of oscillation on the sample, I was able to remove, in an area of the membrane of about  $1\ \mu\text{m} \times 1\ \mu\text{m}$ , all the lipid bilayers from the substrate, in a highly accurate way, creating a trench surrounded by walls consisting of lipid membrane (Fig. 34). In this way an absolute height measurement was possible. The hole in the bilayer shows that all lipids are extracted from the membrane. The depth of the hole of about 14.0 nm is compatible with the presence of two lipid bilayers (6.5 nm) underlying that the rinsing procedure allows to remove almost completely the excess of lipid bilayers from the system.

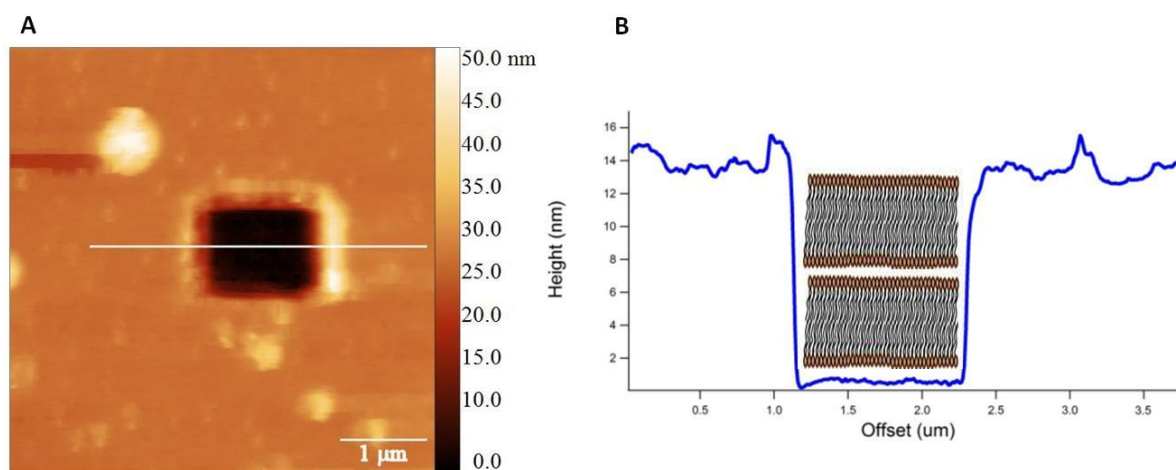


**Figure 34. AFM nanoshaving of DOPC/SM membrane 50:50 in molar ratio in liquid environment. (A)** The AFM topography shows that the nanoshaving of lipids takes place in a very small area (1  $\mu\text{m}$  x 1  $\mu\text{m}$ ) in clear mode. **(B)** The membrane is made by two lipid bilayers (depth of the hole is around 14 nm), underlying the feasibility of the washing treatment.

### 7.3 Three-component membranes

Here I introduced cholesterol in my model system to produce a ternary membrane made by DOPC, SM and cholesterol in 40:40:20 molar ratio. Cholesterol is a key lipid molecule in lipid rafts, interacting with high affinity with SM and changing the structure of the previous two-component membrane (see the three-component phase diagram of Fig. 7). AFM topographic analysis shows that cholesterol changes the morphology of the membrane which is now characterized by the presence of bright domains of bigger lateral dimensions compared to the binary membrane (Fig. 35). The distribution of height shows that a decrease in the  $\Delta Z$  of the two coexisting phases can be observed ( $\Delta Z = 1.0 \pm 0.7$  nm). This effect is due to the cholesterol interaction with SM which leads to a change in the phase of the sphingolipid from  $S_o$  to  $L_o$  phase, referred to as the phase of lipid rafts<sup>19</sup>. In particular cholesterol introduces a disorder factor in the SM domains which corresponds to a lipid phase characterized by intermediate features between the  $S_o$  phase and the fluid phase. In practice, the hydrophilic heads of SMs locally interact with cholesterol to screen its hydrophobic head. SM can interact with the OH group of cholesterol by its phosphate oxygen, whereas its NH group is involved in intermolecular H-bonds between SM molecules. The intercalation of cholesterol causes a worse packing of SM acyl chains with a decrease of the thickness of the SM islands. The effect of cholesterol on DOPC/SM membranes has been extensively studied. An AFM-based work has shown that DOPC/SM/Chol membrane with 10-40% mol Chol displayed a decrease of  $\Delta Z$  ( $L_o$ - $L_\alpha$ ) from 1.2 nm in 10% Chol to 0.6 nm in 40% Chol

However, also with this lipid composition, raft domains and the fluid lipid matrix appear not so flat and clean, in agreement with a non optimal self-assembly of the lipids.

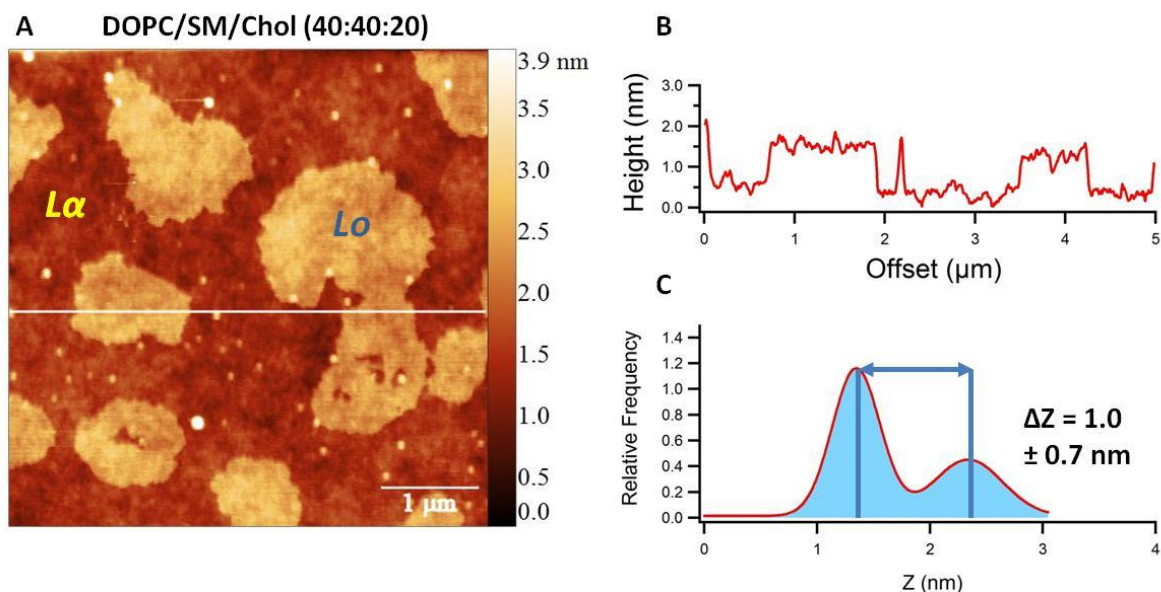


**Figure 35.** AFM image of DOPC/SM/Chol membrane 40:40:20 in molar ratio in liquid environment. (A) The AFM topography shows the presence of two lipid phases, the  $L_o$  (SM-Chol) and  $L\alpha$  (DOPC) phase. (B) The height profile highlights the presence of rough phases as in the previous binary membrane. (C) Distribution of height. AFM measurements were performed in tapping-mode in Milli-Q  $\text{H}_2\text{O}$  at room temperature.

As for the DOPC/SM membrane, I investigated several areas of different ternary membranes. Also in this case there is a high heterogeneity in the morphology of the bilayers, highlighting again the low reproducibility of the drop-casting method (Fig. 36).

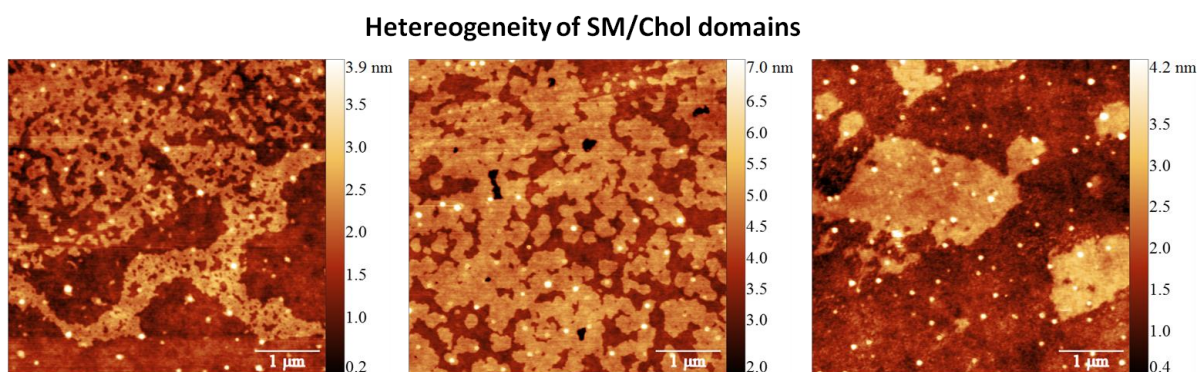


**Figure 36.** AFM images of several SM domains in DOPC/SM model membranes. SM islands have different morphology and cover different areas of membrane.

## 7.4 Application of drop-casting method to study membrane-carbon nanotube interactions

Despite disadvantages as poor reproducibility, poor control of lipid composition and phase separation in samples produced by drop-casting, this method is suitable for the study of interactions between artificial cell membranes and nanostructured biocompatible materials, as carbon nanotubes (CNTs). CNT-based biomaterials have promising features for the design and development of bioelectronic prosthetic devices for novel neural interfaces (see Appendix B). CNTs are conductive nanomaterials which were shown to improve the growth of axons, when used to interface cultured neurons<sup>277,278</sup>. Moreover, they have been shown to enhance the synaptic connections between neurons<sup>279,280</sup>. Improvement of cell-cell communication is fundamental in neural networks, however the role and dynamics of CNTs interaction with the cellular surface remain poorly understood. In this framework, I was involved by the group of Prof. Laura Ballerini from SISSA (Scuola Internazionale Superiore di Studi Avanzati) to study if multi-wall (MW) CNTs, once interfaced to neurons, affect synaptic transmission by modulating lipid membrane structure and dynamics<sup>281</sup>. The investigation focused in particular on cholesterol, which is present in large amount on neuronal membranes and is known to regulate presynaptic vesicle release. My involvement in the study was about the application of drop-casting for the production of supported lipid membranes (SLMs) directly on MWCNTs substrates supported by glass to study the interaction between these nanostructures and artificial lipid bilayers. I prepared a binary membrane made by DOPC and cholesterol in a 2:1 ratio and used the AFM for the topographic analysis of the membrane interfaced to control substrates (as glass) and MWCNTs (Fig. 37 A-C) in liquid environment. I found that lipid islands grown on MWCNTs and on control glass substrates display similar morphology (Fig. 37 A and C). However, AFM reveals the ability of MWCNTs to pierce the membrane through the SLB entire thickness (Fig. 37 C), with the occasional appearance of localized areas where multiple lipid bilayers are piled on the surface, a condition that was not present in the control sample as can be appreciated by the relative height profiles of Fig. 37 A and C.

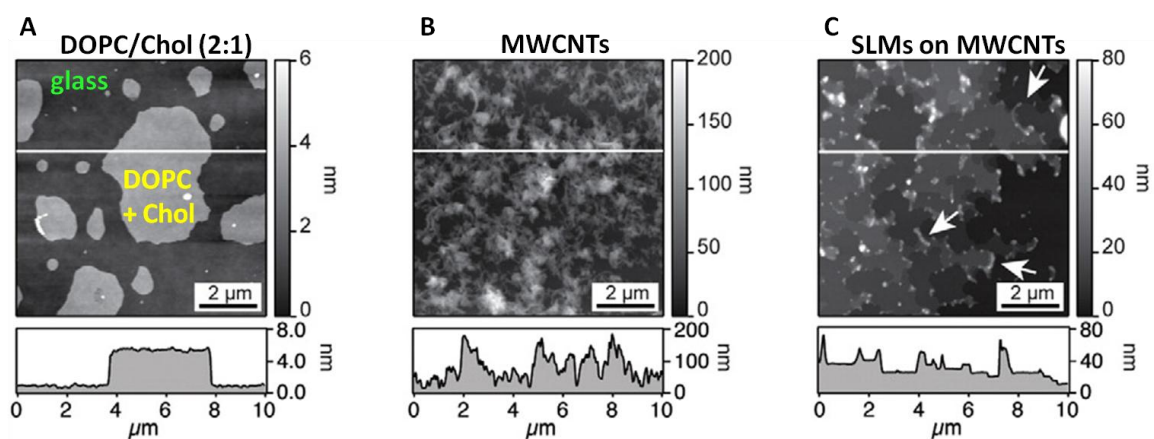


**Figure 37. AFM images of the interaction between SLBs and MWCNTs.** (A) AFM Topography of an incomplete SLB made by DOPC and cholesterol (2:1 ratio) deposited on a control glass surface. The height profile shows that the lipid islands has average height of  $5.0 \pm 0.2$  nm (B) Topography of a MWCNTs carpet deposited on glass via drop-casting. (C) Topography of SLBs deposited on a MWCNTs substrate. White arrows point the MWCNT ability to pierce SLBs, indicated by CNTs emerging from the upper membrane layer. AFM measurements were performed in tapping-mode in liquid buffer at room temperature.

AFM measurements were coupled with Micro-Raman spectroscopy analysis (Fig. 38). Raman spectroscopy is frequently associated to AFM imaging, providing a spectroscopical fingerprint by which molecules can be identified. The idea was to chemically identify the CNT component which pierces the SLBs. The vibrational Raman spectrum of lipids (in red) is characterized by peaks associated with C–N stretching ( $715\text{ cm}^{-1}$ ), C–C stretching ( $1090\text{ cm}^{-1}$ ),  $\text{CH}_2$  deformation ( $1305\text{ cm}^{-1}$  and  $1440\text{ cm}^{-1}$ ), and C=C stretching ( $1655\text{ cm}^{-1}$ ) vibrations. The Raman spectrum of MWCNTs alone on glass (Fig. 38 C, in green) shows two broad peaks centered at  $1350\text{ cm}^{-1}$  and  $1590\text{ cm}^{-1}$  that are commonly assigned to the presence of disorder in graphitic materials and to the tangential vibrations of the carbon atoms, respectively. When SLBs were deposited on glass (Fig. 38 B, in orange), the strong contribution of the substrate was evident. Here the peak at  $1440\text{ cm}^{-1}$  corresponding to  $\text{CH}_2$  deformation in lipids was also visible in spite of the low amount of lipid forming the membrane. In SLMs on MWCNTs, the characteristic two peaks at  $1350\text{ cm}^{-1}$  and  $1590\text{ cm}^{-1}$  present on the tubular structures protruding from the membrane (imaged in Fig. 38 D) confirm the presence of MWCNTs, as suggested by the AFM morphology analysis. In this spectrum (in blue in Fig. 38 A, blue arrow), the peak at  $715\text{ cm}^{-1}$ , attributed to lipid species, is evident as well. This can be due to the laser spot diameter (about  $500\text{ nm}$ ) which is larger compared with MWCNTs diameter ( $50\text{--}250\text{ nm}$ ), resulting in a contribution of the surrounding SLBs to the nominal MWCNT Raman spectrum.

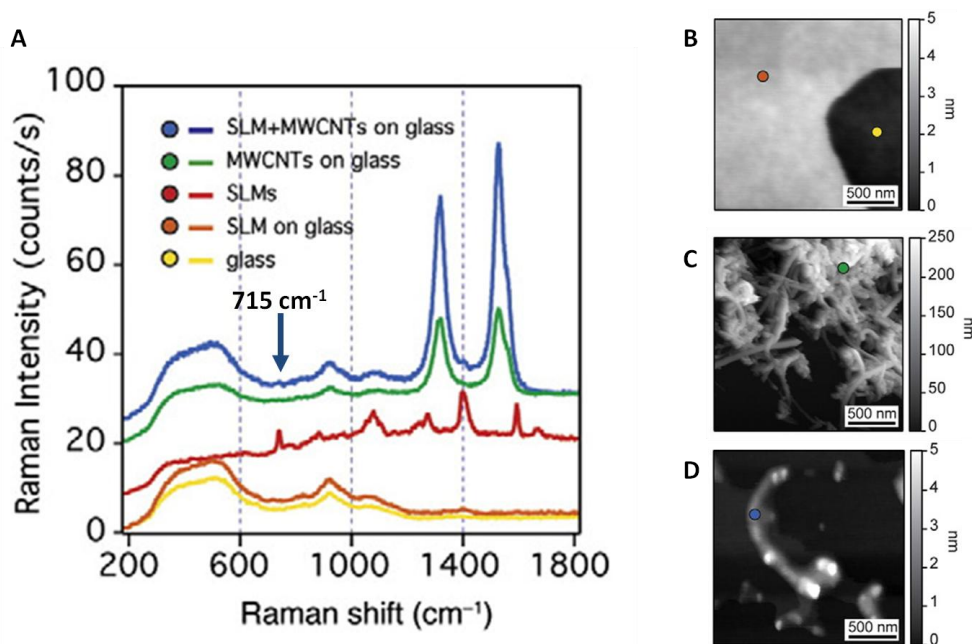


**Figure 38. Raman spectroscopy of model membrane on MWCNTs.** Raman spectra were acquired in the highlighted areas (colored dots) in the AFM images B,C and D acquired at high magnification (glass substrate in yellow, SLB on glass in orange, MWCNTs on glass in green and SLB above MWCNTs in blue). The spectra of MWCNTs with (blue spectrum) and without (green spectrum) SLM were vertically shifted for illustrative purpose. The reference spectrum of lipids (red spectrum) was acquired on a many-layer membranes sample (not shown) in order to minimize Raman signal from the underlying glass surface.

## 7.5 Discussion

The use of the drop-casting method for the fabrication of complex model membranes highlighted some disadvantages especially when the system is made by two or more lipid species. Too many parameters such as temperature, humidity and the type of solvent chosen affect the entire self-assembly process of lipids. Even when the best parameters are chosen, the method is not very reproducible, giving rise to membrane of good quality in only the 30% of experiments. With two- or three-component bilayers, I noted that the membrane seems to be characterized by multiple lipid phases in both fluid phase and ordered lipid domain phase, which are not flat as in the presence of good self-assembly or unique lipid phase. The presence of ripple intermediate phase could be a hypothesis for explaining the presence of non homogeneous lipid phases. The ripple phase is an additional lamellar phase characterized by a periodic one-dimensional undulations on the surface of the membrane, corresponding to a partially-disordered lipid phase<sup>282</sup>. This phase has been shown to exist in multilamellar bilayers of saturated PCs or saturated lipids with other headgroups, and only for temperatures above the pre-transition and below  $T_m$ <sup>283,284</sup>. Considering that the  $T_m$  of SM is 37 °C and the self-assembly of the lipids in the drop-casting was performed at

30 °C (above the pre-transition temperature of SM), it is possible that the system involves a partial presence of ripple phases. However, I was not able to directly visualize by AFM the presence of peculiar structural features on the surface related to this lipid phase.

Another feature that has to be taken into account is the cleanliness of the membrane. The presence of small bright spots (especially in ternary membrane) of 1-2 nm in height makes it difficult to introduce a further complexity in the system as the insertion of a lipidated-protein or GMs, involves heights similar to the ones of contaminating structures. Moreover, the hydration step could destabilize the membrane and create artifacts, with the risk to wrongly interpret the experimental data. Generally the method is suitable for the production of multistacked lipid bilayers that are required for the application of techniques based on X-ray scattering or NMR spectroscopy, for the sake of signal intensity. A functional example of drop-casting application in the field of lipid nanotechnology was the study of the interaction between membranes and MWCNTs. This study has highlighted the ability of CNTs to pierce the lipid bilayers, supporting the hypothesis that these nanomaterials are able to locally interact with the structure of lipid molecules modulating the synaptic activity of neurons <sup>281</sup>. These results supported the findings from neuronal cultured cells in which the MWCNTs microenvironment has been shown to promote the construction of more synapses <sup>279,280,285</sup>.

After having tested the suitability and feasibility of drop-casting in model membrane technology, I decided to move toward a more established method for the production of complex lipid bilayer, the direct vesicle fusion method. Then, I compared the two methods in order to find the technique with the higher benefits/disadvantages ratio for mimicking lipid raft of cell membrane.

## 8. Raft-like lipid bilayers by direct vesicle fusion and applications in biomolecule-lipid interactions

The generation of SLBs onto a solid support by the direct fusion of lipid vesicles is one of the most characterized methods in model membrane technology. This method is easy and reliable and can drive the formation of complete layers within few hours. It is widely accessible since it does not require advanced equipment and allows the production of very high quality SLBs. These advantages confer to vesicle fusion an important role in advanced SLB-based research platforms, particularly for the fabrication of complex, multicomponent SLBs that more accurately mimic native cell membranes<sup>286</sup>. Vesicle fusion has also the remarkable advantage that the same preparation protocol can be used for all lipid vesicle compositions highlighting the strong versatility of the method.

In order to produce flat, homogeneous symmetric membranes with multiple lipid composition I started from a batch of binary and ternary multilamellar vesicles, which then underwent extrusion through a polycarbonate filter with a defined pore size of 100 nm for the formation of controlled unilamellar vesicles of the same size (see paragraph 5.1). The extrusion method in fact allows for the best homogeneity of LUVs (large unilamellar vesicles) size distribution in the final suspension when compared with other methodologies, as sonication, homogenization and freeze-thaw sonication<sup>287</sup>. The only prerequisite in this procedure, especially when it is about complex lipid compositions, is the extrusion temperature, which should be above the  $T_m$  of the various lipids. In this manner, I first produced a ternary membrane made by DOPC, SM and cholesterol playing with the relative concentration of the three molecules to find the highest stability conditions mimicking physiological membranes composition (DOPC/SM (50:50) + 5% Chol, DOPC/SM (66:33) + 5% Chol, DOPC/SM (66:33) + 20% Chol). Finally, I used such ternary SLBs for studying the distribution in the membrane of the GM1 ganglioside, a lipid raft marker, as well as of a pathological lipidated-protein PrP<sup>C</sup> in order to investigate the potential of this model membrane tool in the study of lipid raft-biomolecule interactions.

### 8.1 Ternary membranes

I first produced a membrane made by DOPC and SM (50:50 in molar ratio) with 5% of cholesterol, in order to mimic raft-like domains. Despite cholesterol concentration in real cellular membrane varies between the 15% and 50% of the total lipid composition<sup>288</sup>, I started from a low cholesterol concentration (5% molar) to study its role in the formation of artificial membranes. As we will see

in the next paragraph, the chosen concentration allows to create stable lipid raft domains and to distinguish them morphologically from the rest of the membrane.

The membrane was fabricated on freshly cleaved mica. I used  $\text{CaCl}_2$  salt solution (5 mM) to better promote the initial adsorption and rupture of LUVs on mica surface. Divalent cations, such as  $\text{Ca}^{2+}$  and  $\text{Mg}^{2+}$  are commonly used to promote SLB formation, especially with negatively-charged vesicles<sup>289,290</sup>. However, the same procedure performed in Milli-Q  $\text{H}_2\text{O}$  produced a high quality SLB as well (data not shown), without any measurable variations of membrane morphology. Overall, with the lipid composition of my model membranes (DOPC/SM/Chol), the presence of divalent cations for the formation of SLBs does not appear to be essential. Moreover, the following rinsing step removes almost completely any presence of such divalent ions, leaving the membrane incubated in only Milli-Q  $\text{H}_2\text{O}$ .

I successively analyzed the lipid bilayer formation by AFM working in tapping-mode in liquid environment. Extended SLBs form within 15 minutes of vesicle incubation. After a gentle rinse, to remove the excess of vesicles, the sample can be analyzed by AFM. In analogy with the measurements shown in the previous chapter, AFM topography analysis shows a membrane characterized by two coexisting phases, due to the different physical state of SM and DOPC at environment temperature (Fig. 39). Comparing the SLBs obtained by vesicles fusion with the ones produced by drop-casting, it is possible to note that the morphological quality of the new mixed lipid bilayers appears to be much higher here: the flatness of the membrane produced by direct vesicle fusion is appreciable from the AFM topographic image (Fig. 39 A). The two phases,  $L\alpha$  and  $S_o$ , are very well separated in the plane of the bilayer, without any presence of intermediate phases or contaminating bright spots. The roughness values measured on  $L\alpha$  and  $S_o$  phase domains are reported in Fig. 39 D, in comparison with the same values on drop-casting prepared membranes (see paragraph 7.2). The SLB produced by vesicle fusion shows a 3-fold decrease of roughness for both lipid phases with respect to the drop-casted lipid bilayer (vesicle fusion:  $L\alpha=73.7 \pm 1.6$  pm,  $S_o=115.6 \pm 8.1$  pm; drop casting:  $L\alpha=252.8 \pm 23.5$  pm,  $S_o=294.9 \pm 38.5$  pm). The distribution of topographic heights shows that the ordered lipid areas (SM+Chol) protrude from the fluid DOPC phase with an average height of  $1.2 \pm 0.2$  nm. Moreover, the ratio of the surface covered by the two phases ( $L\alpha:S_o$ ) on the membrane is 47.0:53.0 and matches almost perfectly with the initial lipid molar ratio, underlying that the vesicle fusion method allows a very good control of lipid membrane composition.

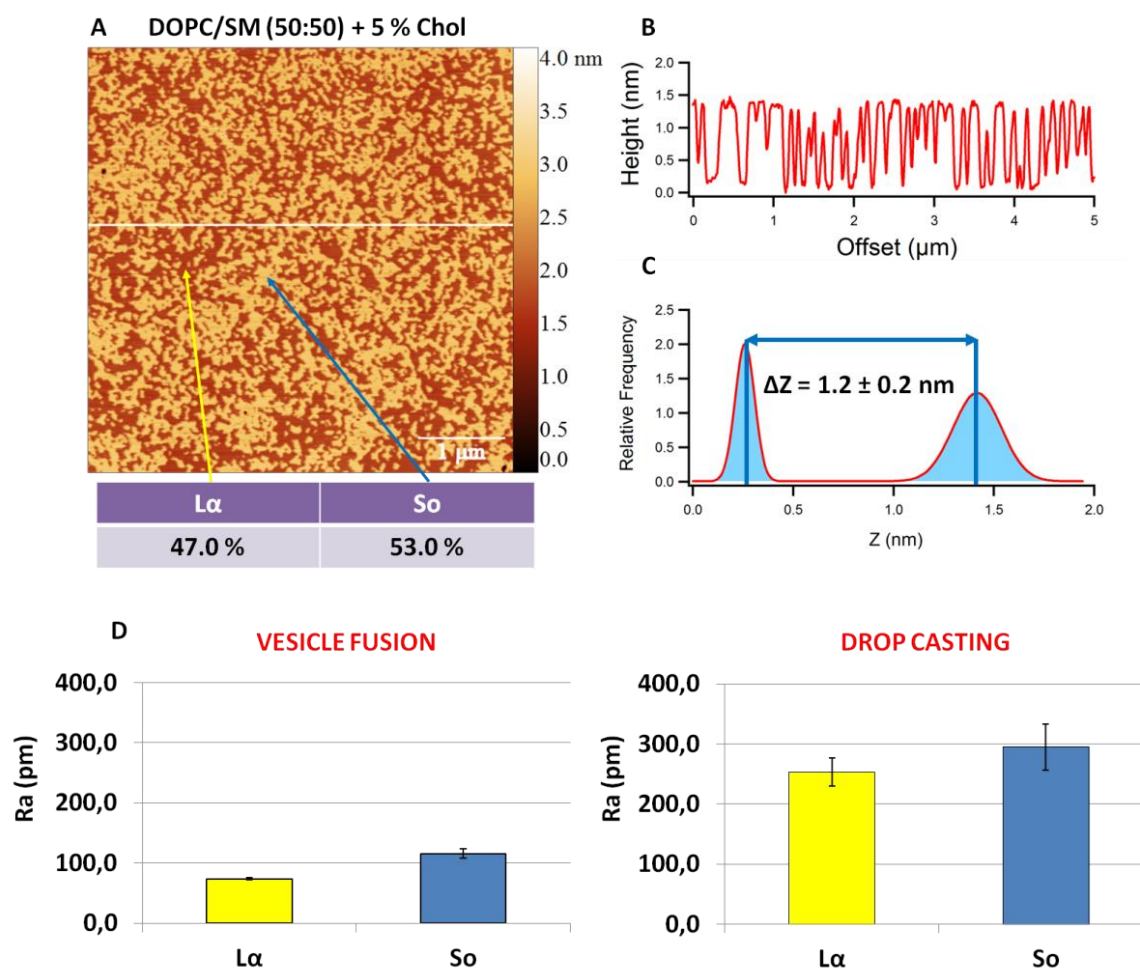


**Figure 39.** AFM image of DOPC/SM membrane (50:50 in molar ratio) with 5% of cholesterol in liquid buffer. **(A)** The topography image shows the coexistence of two lipid phases, the So (SM+Chol) and L $\alpha$  (DOPC). The relative surface ratio is indicated. **(B)** The height profile highlights the presence of good lipid phase separation. **(C)** Distribution of height. **(D)** Roughness comparison of drop-casting and vesicle fusion method, for both lipid phases. AFM measurements were performed in tapping-mode in Milli-Q H<sub>2</sub>O at room temperature.

In the same way as for drop-casted SLBs, I used AFM nanoshaving for the quantification of the bilayer thickness after the rinsing step (Fig. 40). AFM topography shows that only one single lipid bilayer (height around 6.5 nm) is present on the mica surface, highlighting the strength of the vesicles fusion method for obtaining a homogeneous, clean and highly reproducible SLB system for the study of lipid rafts behavior.

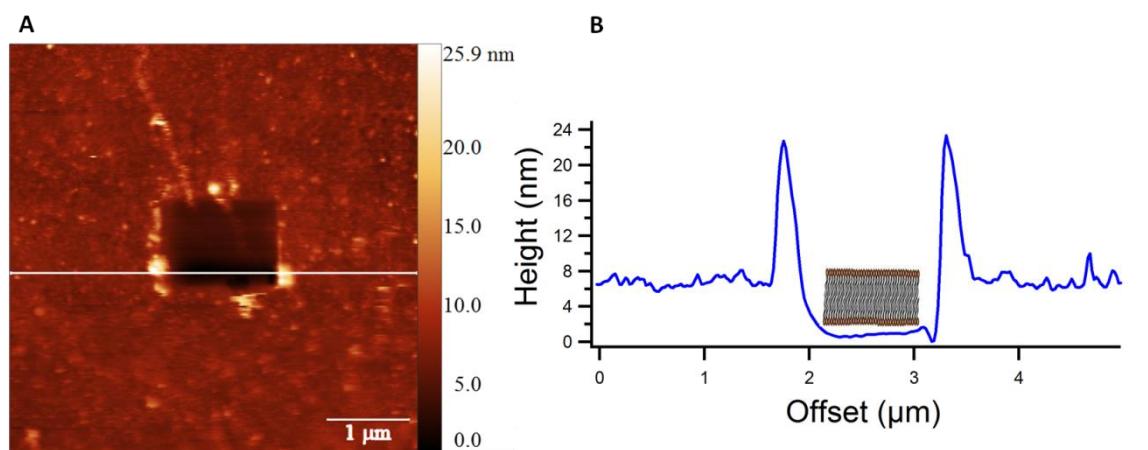


**Figure 40. AFM nanoshaving of DOPC/SM membrane (50:50 in molar ratio) + 5% Cholesterol in liquid buffer. (A)** AFM topography image shows a hole of (1 μm x 1 μm) in correspondence of nanoshaving **(B)** AFM topographic profile across the hole area showing that the depth of the hole corresponds to one single lipid bilayer (around 6.5 nm). AFM nanoshaving was performed in tapping-mode in Milli-Q H<sub>2</sub>O at room temperature.

Although the SLB obtained so far were already of high quality, I decided to change the lipid ratio introducing an asymmetry in the composition to better follow the evolution of raft-like domains. In particular, I focused on the production of membranes made by DOPC and SM (66:33 in molar ratio) with 5% cholesterol. After AFM characterization, I increased the concentration of cholesterol to 20% maintaining the same DOPC:SM ratio (DOPC/SM (66:33) + 20% Chol) in order to investigate possible morphological changes within the different lipid phases induced by cholesterol. 20% of cholesterol is a reasonable physiological value for plasma cell membrane<sup>291</sup>. The membrane characterized by 5% of cholesterol shows single raft-like domains that protrude from the fluid phase with an average height of  $1.1 \pm 0.2$  nm (Fig. 41 A, C). These lipid islands have heterogeneous lateral size distribution in the range of 0.2 – 1.0 μm. Even in this case the surface ratio of the two coexisting phases (L $\alpha$ :S $\alpha$ ) derived from AFM images is 64.2:32.8 and matches well with the initial lipid composition (Fig. 41 E). The membrane with 20% of cholesterol displays a different morphology having raft domains with a more dendritic shape and being characterized by a higher raft surface coverage (L $\alpha$ :L $\alpha$  (57.0:43.0),) compared to the membrane with lower cholesterol content (Fig. 41 B, F). This ratio can be rationalized assuming that cholesterol is mostly sequestered by the SM in the solid ordered phase, increasing its fluidity and promoting a S $\alpha$  to L $\alpha$  transition [REF]. Assuming the same occupied surface per molecule (which is not exactly true since since there are not reference values for the intrinsic volume of cholesterol<sup>292</sup>) we calculated the excess surface that is due to 20% cholesterol-induced lipid ordering from the relative molar percentage, finding DOPC/SM+Chol = 54:47, not far from the measured one. Indeed, the entire volume occupied by the different phases change by changing chol content. The hydrophobicity of cholesterol (contains only one OH group per molecule), normally screened by sequestering

adjacent, polar lipids, introduces to the membrane a certain level of viscosity and dynamic clustering of chol-SM aggregates, reducing the rafts height with respect to the fluid, disordered lipid phase around. This explanation is supported by the 20% decrease of the average  $\Delta Z$  (Lo-L $\alpha$ ) value ( $0.9 \pm 0.2$  nm) measured and by the slight increase of the ordered phase roughness when moving from 5% to 20% chol (Fig. 41 D). Finally, lipid-raft domains appear more dendritic when the level of cholesterol is increased to 20%. This is a sign of diffusion-limited aggregation, which is in agreement with the dynamic molecular clustering described above. Further studies are required to corroborate this hypothesis.

Given the higher flatness of the lipid rafts in correspondence to the (DOPC/SM (66:33) + 5% Chol) membrane, and since our ultimate goal is to shed light on the interaction of biological relevant biomolecules with lipid-raft containing membranes through topographic AFM measurements, we decided from this moment on to use such SLB composition as model systems for further studies.

DOPC/SM (66:33)

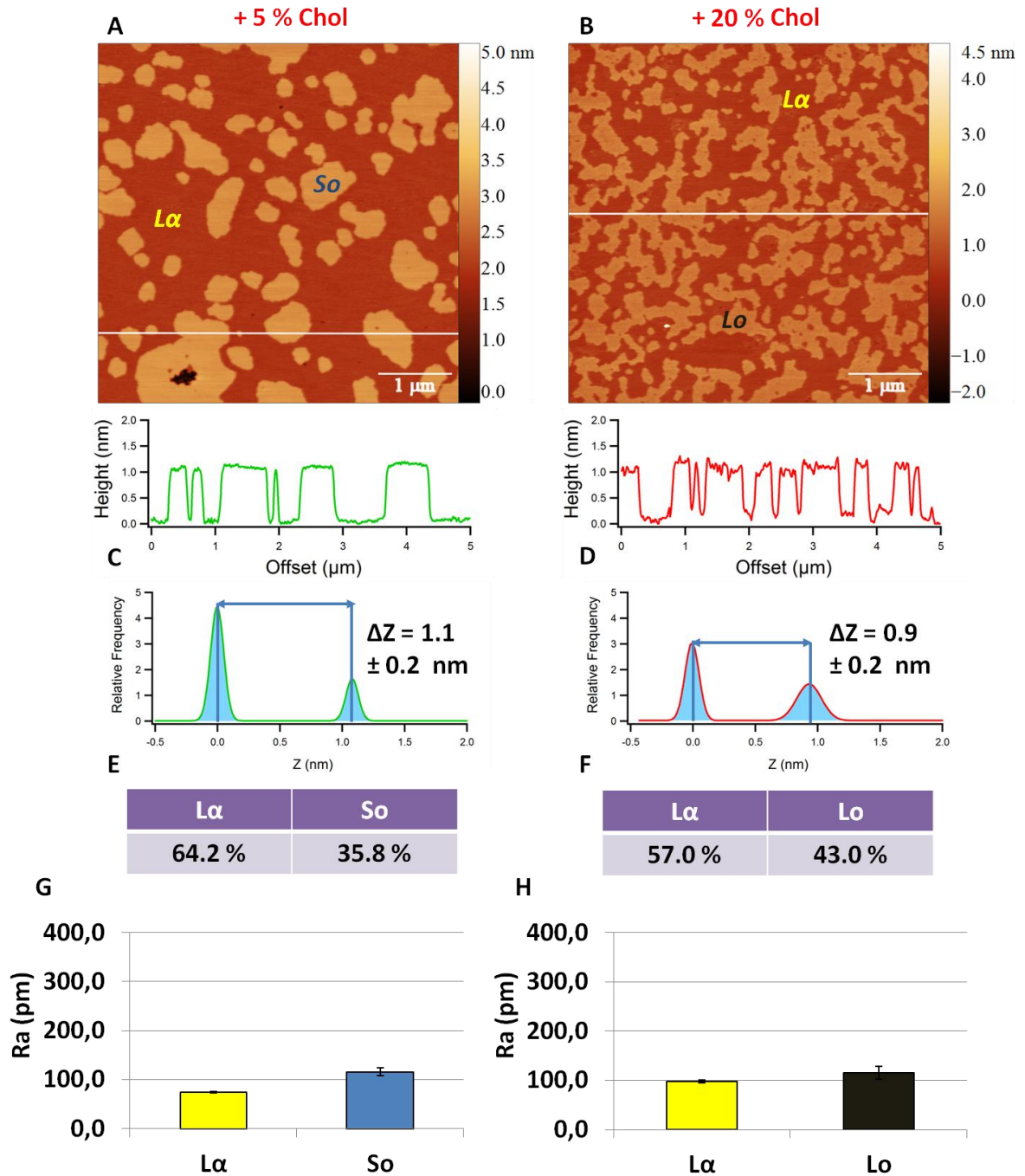


**Figure 41. AFM images of raft-like membranes (DOPC/SM (66:33)) in presence of 5% (A) and 20% (B) of cholesterol, respectively.** The membrane with higher cholesterol content shows a higher lipid raft coverage and a decrease in the  $\Delta Z$  (Lo-L $\alpha$ ) value compared to the membrane with 5% of cholesterol. AFM measurements were performed in tapping-mode in Milli-Q H<sub>2</sub>O at room temperature. (C-D) Height distribution for 5% chol and 20% chol membrane, respectively). (E-F) Lipid phase ratio. (G-H) Roughness of lipid phases are similar in both membranes. AFM images were collected in tapping-mode in Milli-Q H<sub>2</sub>O at room temperature.

## 8.2 Stability of SLB in aqueous solution

Before incubating biomolecules with the prepared membranes, the stability of planar lipid bilayers in Milli-Q H<sub>2</sub>O as a function of time needs to be assessed. In particular, I focused on our most promising three component model membrane mixture (DOPC/SM 66:33 + 5% cholesterol) focusing on its structural integrity and on the possible morphological changes in the coexisting two lipid phases after a prolonged incubation in liquid environment. After 24 hours in Milli-Q H<sub>2</sub>O, the membrane maintains almost the 95% of its structural integrity, remaining clean and with very flat domains (Fig. 42). The topographic height variation  $\Delta Z$  between the S<sub>o</sub> and L $\alpha$  phase ( $1.2 \pm 0.3$  nm) does not change with respect of the same value of the as-prepared membrane (see for reference the image in Fig. 41), as well as the relative ratio between L $\alpha$  and S<sub>o</sub> phase (66.5:33.5). However, there is clear evidence for the formation of defect sites, in the form of damaged areas (black holes, indicated by red arrows in the AFM images of Fig. 42) which seem to be essentially located at the level of the L $\alpha$  phase. This phase is usually more prone to destabilization by environmental factors, being less packed and less ordered than the ordered domains [REF]. The black circular holes have a depth of 2.5-3.0 nm, which agrees with the extraction of the upper fluid monolayer from the lipid bilayer membrane. Moreover, the surface roughness of these defect sites is  $353.1 \pm 25.3$  pm which is much higher than the one of both lipid phases (L $\alpha$  =  $84.4 \pm 5.8$  pm, S<sub>o</sub> =  $130.1 \pm 6.1$  pm) (Fig. 42 G). We suppose that the unfavorable exposure of lipid acyl chains to water leads to an unstable situation with the lack of an optimal membrane packing and the consequent increase of the roughness.

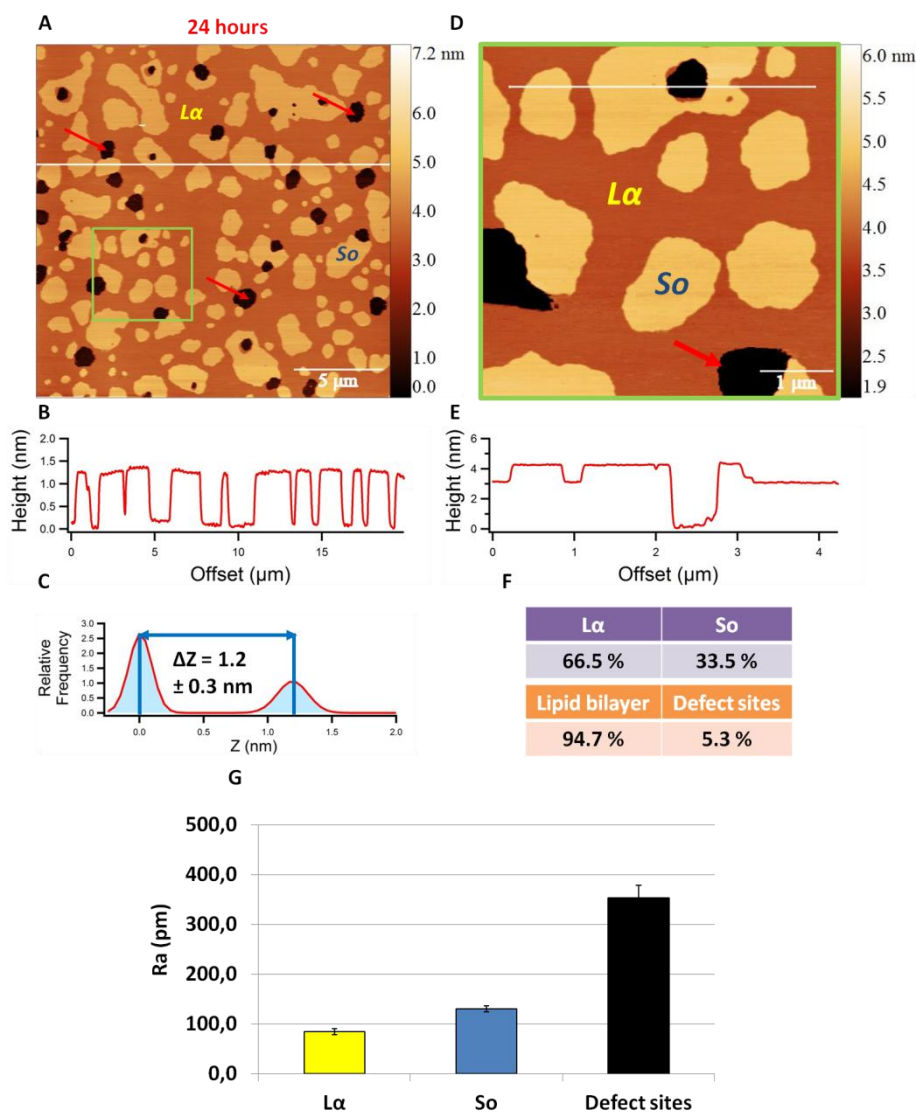


**Figure 42.** AFM topography of a DOPC/SM/Chol model membrane after 24 hours in Milli-Q H<sub>2</sub>O. AFM image of the membrane surface, 20x20  $\mu\text{m}^2$  (A) and a zoom image, 5x5  $\mu\text{m}^2$  (D), to highlight structural details. (C) The difference of height between the L $\alpha$  and S $\alpha$  phase remains constant. (F) Relative ratio of L $\alpha$  and S $\alpha$  is reported. The bilayer has only 5% of damage sites. (B, E) Height profiles. (G) Roughness of lipid phases and damaged areas are indicated. AFM images were collected in tapping-mode in Milli-Q H<sub>2</sub>O at room temperature.

Finally, from the comparison between the two images shown in Fig. 43 we can see that lipid rafts after 24 h in Milli-Q water form lipid islands of bigger dimensions. Comparative analysis of the surface occupied by raft-like domains at different incubation time showed a slight increase after 24 h in Milli-Q water (Fig. 43). After 1 h incubation the membrane is characterized by ordered domains with area distribution in the range of 0.01-1.00  $\mu\text{m}^2$ . After 24 h in liquid environment, the membrane shows a decrease of around 80% in the number of raft-like islands, with the domain area distributed over a broad range of values (0.05-6.00  $\mu\text{m}^2$ ), due to domain coalescence phenomena.

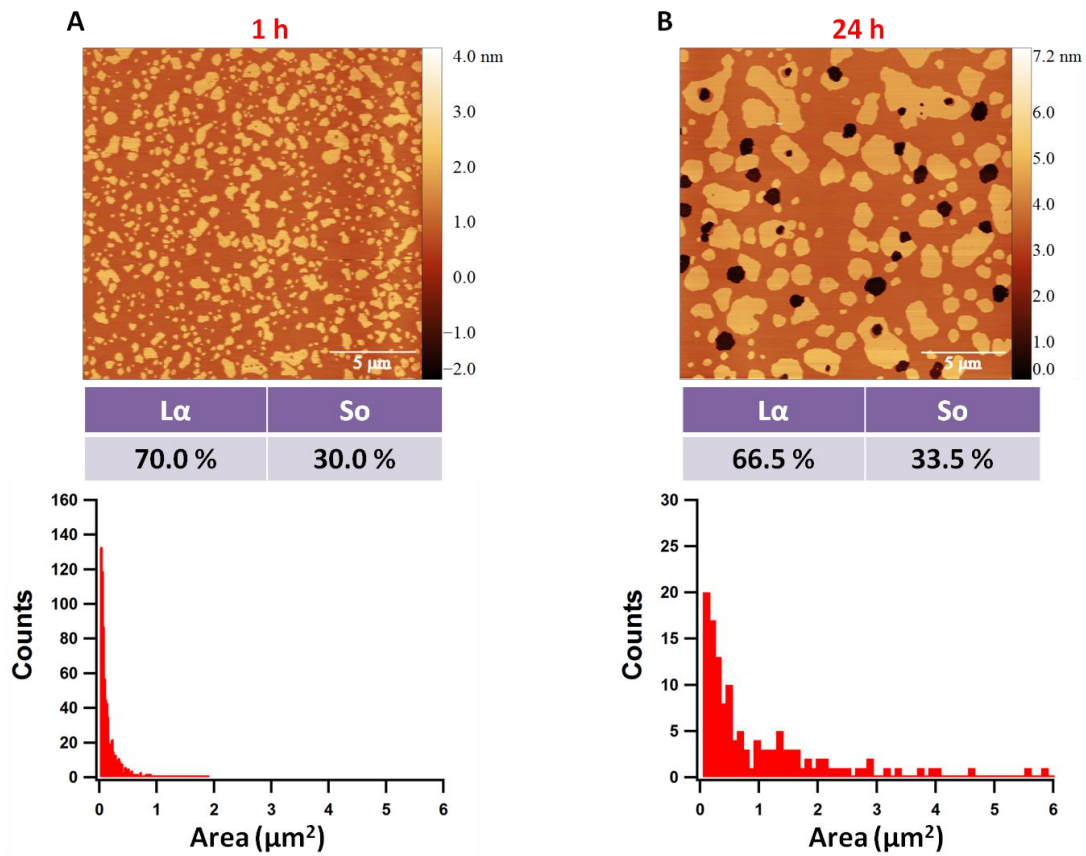


**Figure 43. Coalescence of raft-like domains of DOPC/SM (66:33) + 5% Chol. (A)** Membrane at time 0 (1 hour) and **(B)** membrane at 24 hours in Milli-Q H<sub>2</sub>O with relative ratio of lipid phases (L and So) and the distribution of So-domain areas. Membrane at 24 hours shows a decrease in the number of raft domains which appear of bigger dimension compared to membrane at time 0.

When tested after a longer time in the same solution (48 hours, Fig. 44) one can see that the membrane further damages becoming extensively discontinuous, leaving lipid membrane patches on the surface. The distribution of heights is still bimodal, but with a broader distribution around each peak and with average height separation of  $\Delta Z = 4.1 \pm 0.8$  nm, confirming the presence of a damaged, not homogeneous membrane made of both lipid bilayers (5.0-6.0 nm thick) and monolayer islands (2.5-3.0 nm thick). It is now difficult to identify the ordered and disordered lipid phases. This result demonstrates that the system is suitable for investigating biological processes until the 24 hours in liquid buffer, maintaining a good stability and the original structural properties.

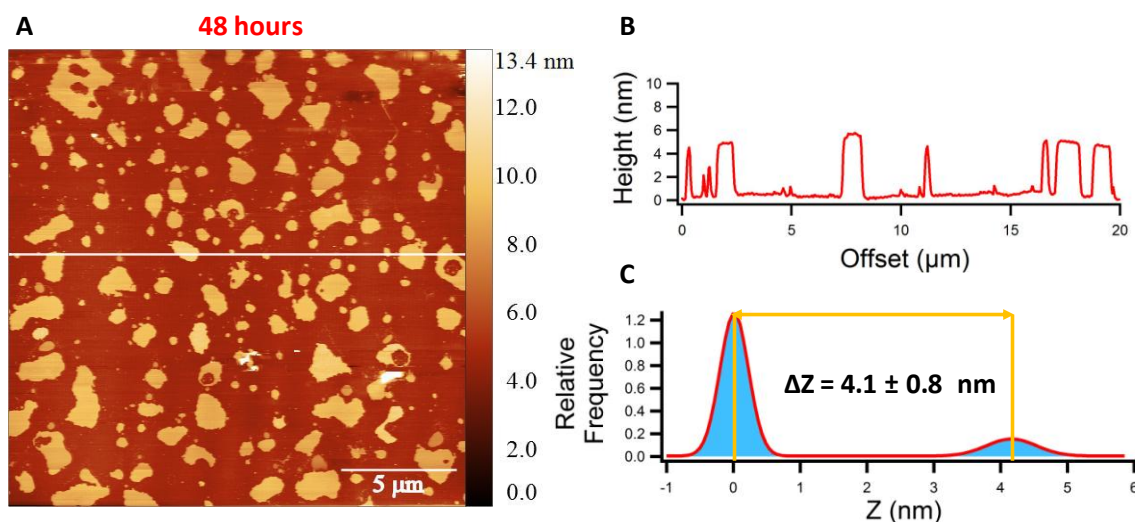


**Figure 44. AFM topography of a DOPC/SM/Chol model membrane after 48 hours in water solution. (A)** AFM image and **(C)** distribution of height shows the presence of membrane patches. **(B)** Height profile. AFM image was collected in tapping-mode in Milli-Q H<sub>2</sub>O.

### 8.3 GM1 distribution on lipid rafts

After the optimization of the protocol based on direct vesicle fusion for the production of multi-component SLBs mimicking lipid raft domains, I selected the most stable mixture, the DOPC/SM 66:33 + 5% chol, and moved towards the production of more complex models of raft-like membranes. First, I introduced in the layer a new player, namely the GM1 ganglioside, a biologically relevant molecule directly correlated with lipid rafts<sup>293</sup>. GM1 is a glycosphingolipid that is more abundantly expressed in the nervous system. Its polar head is formed by a polysaccharide and by one sialic acid residue, with a 3-fold higher polar surface area with respect to SM. In cells, GM1 is primarily, but not exclusively, localized in the outer leaflets of plasma membranes where it is involved in cell-cell recognition and signal transduction within caveolae and lipid rafts<sup>294</sup>. Moreover, these molecules have a role in several neurodegenerative disease such as AD, where GM1 has been proposed to initiate the aggregation of amyloid- $\beta$  peptides<sup>295</sup>. In order to study GM1 distribution into my model system, I added two different percentages (1% and 2.5%) of GM1 to the initial lipid mixture. From these 4 components (DOPC, SM, Chol and GM1) LUVs I produced then the SLB and used AFM to investigate membrane stability and structural properties. In the sample with 1% GM1 (Fig. 45) one can see that the membrane morphology is very similar to the one with three lipid components shown for instance in Fig. 41 A. Two are the main differences: the appearance of small nanodomains, mostly decorating the borders of the So phase (blue arrows in Fig. 45 B); the presence of island “hole” defects, as in Fig. 42 A. The nanodomains protrude from the So phase of about 2.0 nm (line profile in Fig. 45). Such

domains might be originating from a phase separation of GM1-SM-chol domains from the SM-chol areas. The protruding height is consistent with the higher polar surface of GM1 head with respect to SM.

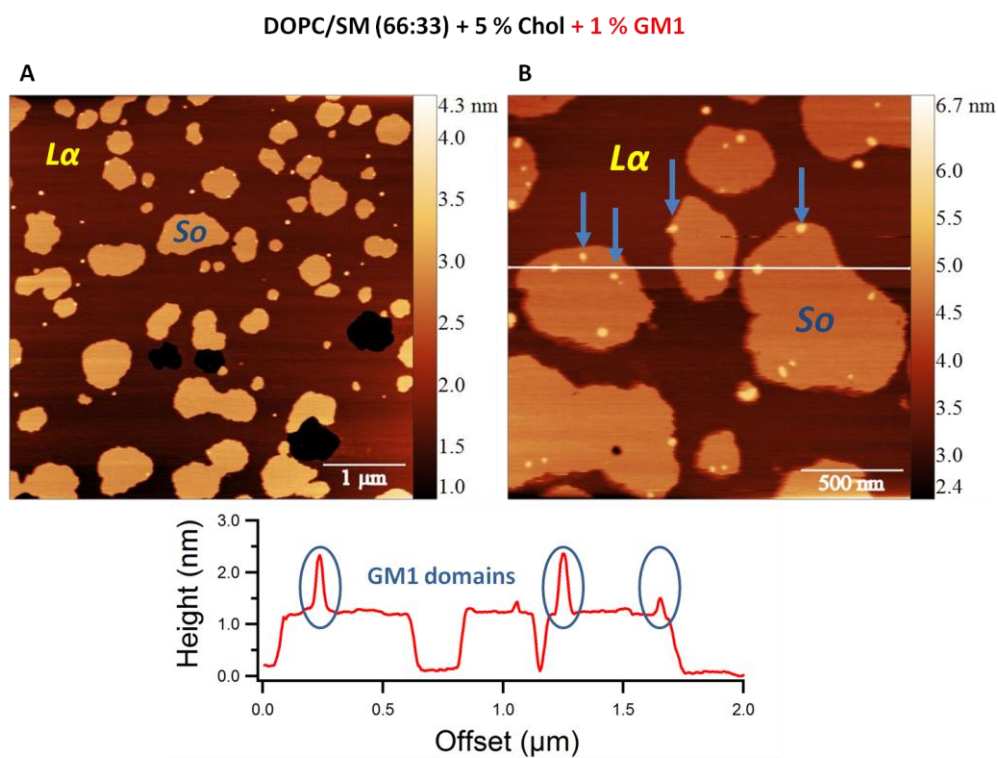


**Figure 45. AFM topography of a SLB composed by DOPC/SM/Chol + 1% GM1.** Blue arrows indicates GM1 nanodomains on ordered raft domains in AFM image.

In the sample with 2.5% GM1 shown in Fig. 46, the number of nanodomains increases consistently: small circular islands of 20-160 nm in diameter (as shown in the distribution of equivalent disc radius values in the lowest panel on the right of Fig. 46) protruding of about 0.5-2.0 nm from the  $So$  phase can be observed. On the bigger  $So$  SM-chol rafts these nanodomains are again mainly distributed at the borders, to indicate a preferential GM1 insertion from  $So$  raft periphery, as can be seen in the zoomed-in image of Fig. 47. From the same image it is possible to highlight that even the smaller GM1 domains which at a first glance seemed to be located on  $L\alpha$  phase, are actually surrounded by a small crown of lipids in  $So$  ordered phase, further indicating that the localization of these molecules take places only in the rafts. AFM images acquired after 1h, 2h and 3 h respectively show a progressive increase of the GM1 nanodomains density (Fig. 45), especially after 2 h imaging. This phenomena highlight the possible progressive formation of GM1-SM-chol domains which detach from the SM-chol  $So$  islands. “Dark hole” areas, present also in this case, do not seem to evolve in size with imaging time.

**DOPC/SM (66:33) + 5 % Chol + 2.5 % GM1**

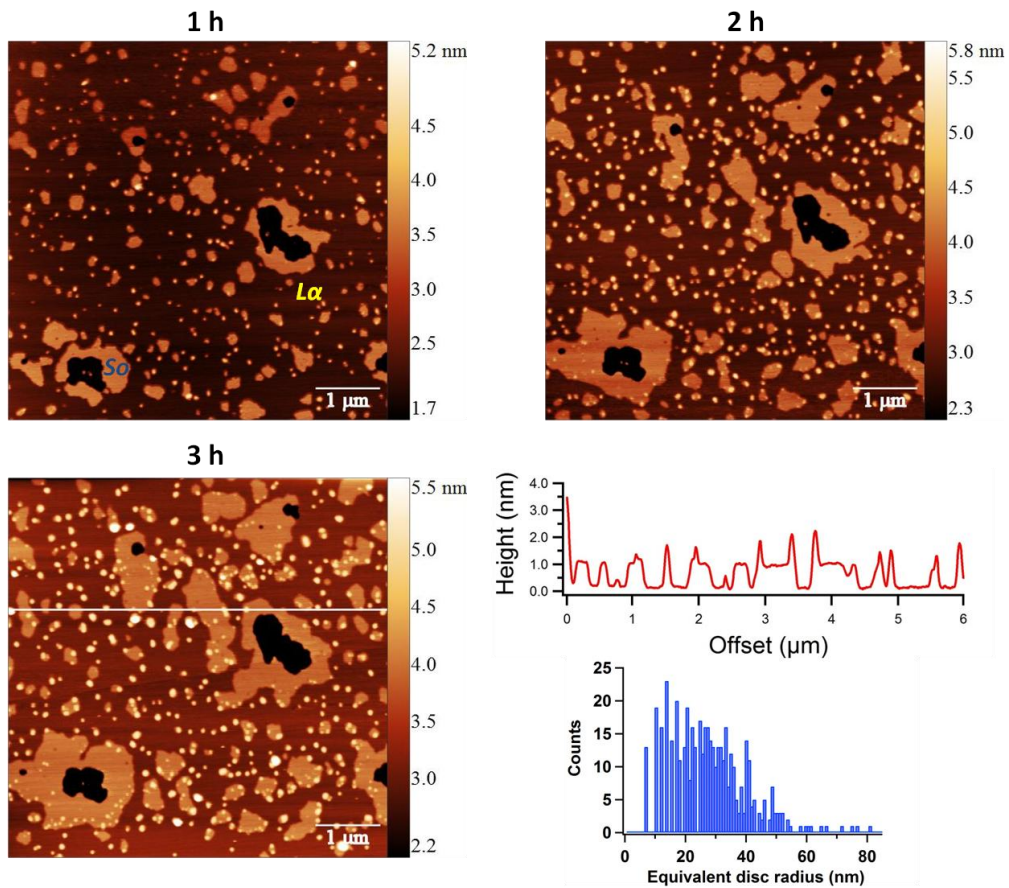


**Figure 46. AFM topography of a SLB composed by DOPC/SM/Chol + 2.5% GM1.** Imaging during time shows the enrichment of rich-GM1 nanodomains on raft-like domains ( $S_o$  phase). These domains are 20-160 nm in size and 0.5-3.0 nm in height. AFM images were collected in tapping-mode in Milli-Q  $H_2O$ .

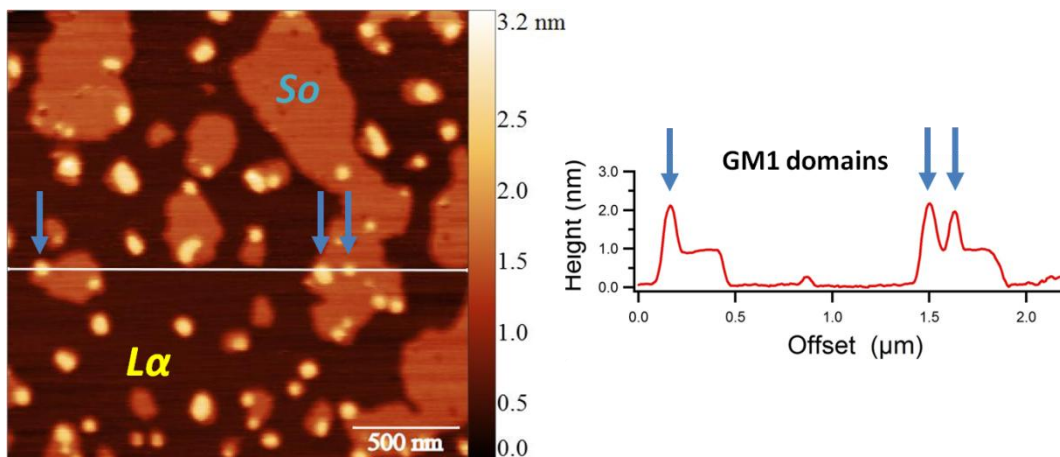


**Figure 47. Zoom details of SLB composed by DOPC/SM/Chol + 2.5% GM1.** GM1 islands mainly localize at the borders of  $S_o$  domains (blue arrows). AFM image was collected in tapping-mode in Milli-Q  $H_2O$ .

## 8.4 Lipidated-Prion protein (PrP<sup>C</sup>) insertion into model membranes

Prions are pathogens that cause a group of neurodegenerative transmissible spongiform encephalopathies (TSEs) also known as prion diseases. Despite their highly heterogeneous features, these disorders are characterized by the conversion of the normal cellular prion protein (PrP<sup>C</sup>) into the toxic scrapie isoform (PrP<sup>Sc</sup>) in the central nervous system (CNS). The finding of PrP<sup>Sc</sup> as molecular hallmark of all TSEs has made it possible to definitively diagnose prion diseases at both the pathological and molecular levels. Moreover, the discovery and further characterization of PrP<sup>Sc</sup> have provided enormous insights into the nature of prions. The physiological functions of prions remain still defined. However, several studies have been revealed that PrP<sup>C</sup> may play a role in oxidative stress reduction, signal transduction, apoptosis regulation, adhesion of the extracellular matrix and the formation and maintenance of synapses<sup>296</sup>. As discussed in the introduction (paragraph 3.2) PrP<sup>C</sup> is a GPI-anchored protein that is predominantly localized in the outer leaflet of the neuronal cell membrane<sup>297</sup>. Although the biological function of PrP<sup>C</sup> has not been fully understood yet, its membrane attachment via a GPI anchor seems to be critical for the conversion into the pathological PrP<sup>Sc</sup> isoform, which generates highly insoluble, toxic aggregates. Several evidences support the idea that the lipid environment has a key role in prion conversion and propagation, especially the association of PrP<sup>C</sup> with lipid raft domains<sup>298-300</sup>. In this framework, I was involved by Prof. G. Legname (SISSA) in collaboration with Prof. C. F. W. Becker (University of Wien) in the study of the interaction of a lipidated-Prion protein with raft-like artificial model membranes. I tested a full-length PrP (residues 23-231, FL-PrP) modified with a C-terminal membrane anchor (MA) via a semisynthesis strategy<sup>301</sup>. I produced a ternary membrane made by DOPC, SM (66:33 in molar ratio) with 5% cholesterol and investigated the ability of FL-PrP-MA to interact with this membrane in order to identify the effect of lipid membrane composition on protein conversion and conformation. After 1 h of incubation of the SLB with FL-PrP-MA (25 nM), AFM analysis in liquid buffer shows the formation of large protein clusters on highly ordered membrane domains (So) whereas, similarly to the GM1 case, the fluid phase of membrane is not involved (Fig. 48). Surprisingly, many raft domains seem not to be perturbed by the protein, in contrast with the typical mode of action of several GPI-anchored proteins in other model membrane experiments. Several studies have highlighted that these proteins are characterized by a first insertion at the borders of highly ordered domains followed by a diffusion in the central region and a final saturation of the surface of these functional lipid islands<sup>302,303</sup>.

The height profile along the red line in the 2x2  $\mu\text{m}^2$  AFM image (Fig. 48 B) reveals that the protein clusters can be associated to the formation and accumulation of oligomers on lipid rafts. The main results is that FL-PrP-MA is targeted to the ordered domains of the membrane but it is not

possible to infer whether the interaction is driven by the MA, which then promotes the aggregation of the prion, or by an intrinsic protein affinity for the Lo phase as well as the by the molecular interaction between PrP molecules .

**DOPC/SM (66:33) + 5 % Chol + FL-PrP-MA (1 h)**

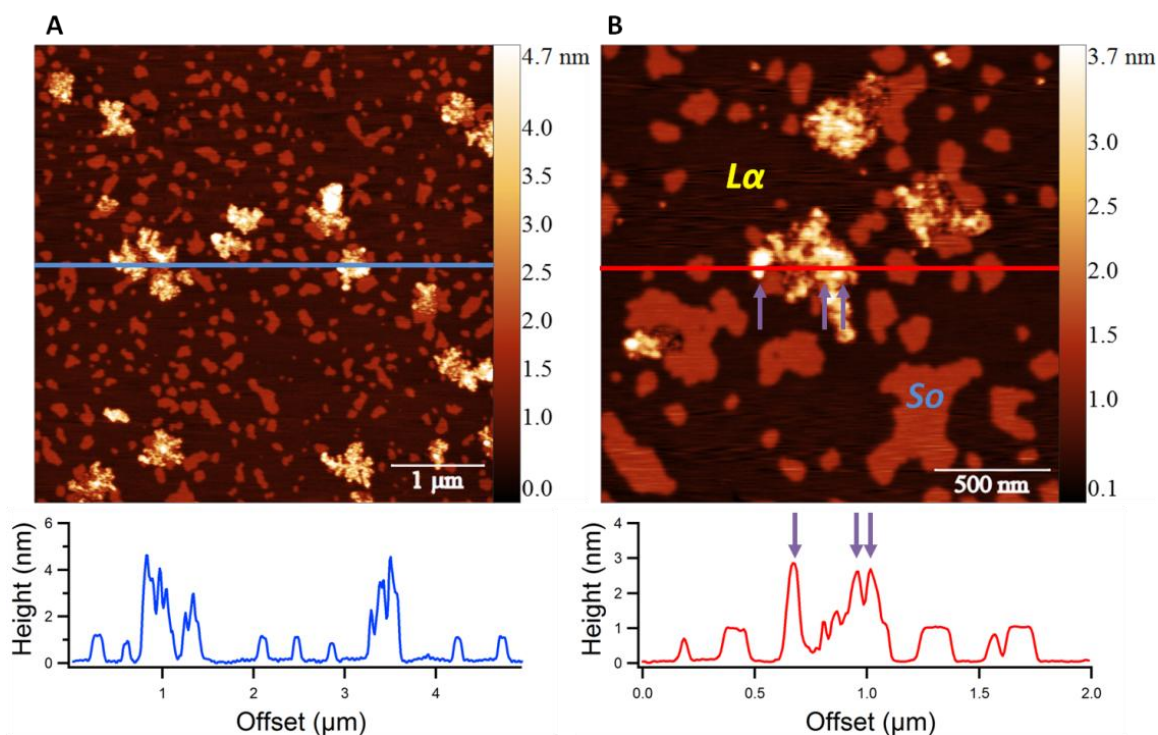


**Figure 48. The interaction of FL-PrP-MA with raft-like model membrane. (A)** AFM topography of PrP aggregation and the height profile. **(B)** Zoom AFM image reveals that the protein forms oligomers (lilac arrows) that preferentially accumulate on raft domains ( $S_o$  phase). AFM images were collected in tapping-mode in Milli-Q  $H_2O$  at room temperature.

Successively, I analyzed the membrane by AFM after 12 h of incubation with FL-PrP-MA. As we can see from the Fig. 49, the membrane undergoes an extensive structural damage characterized by many areas which can be associated to the extraction of the upper monolayer (2-3 nm the depth of these damaged site). However, the two lipid phases are still distinguishable. As expected, bigger size raft domains are present as well as protein oligomer clusters. However, the aggregation seems to have reached an equilibrium because cluster heights are similar to those found from the membrane after 1 h of protein incubation.

### DOPC/SM (66:33) + 5 % Chol + FL-PrP-MA (12 h)

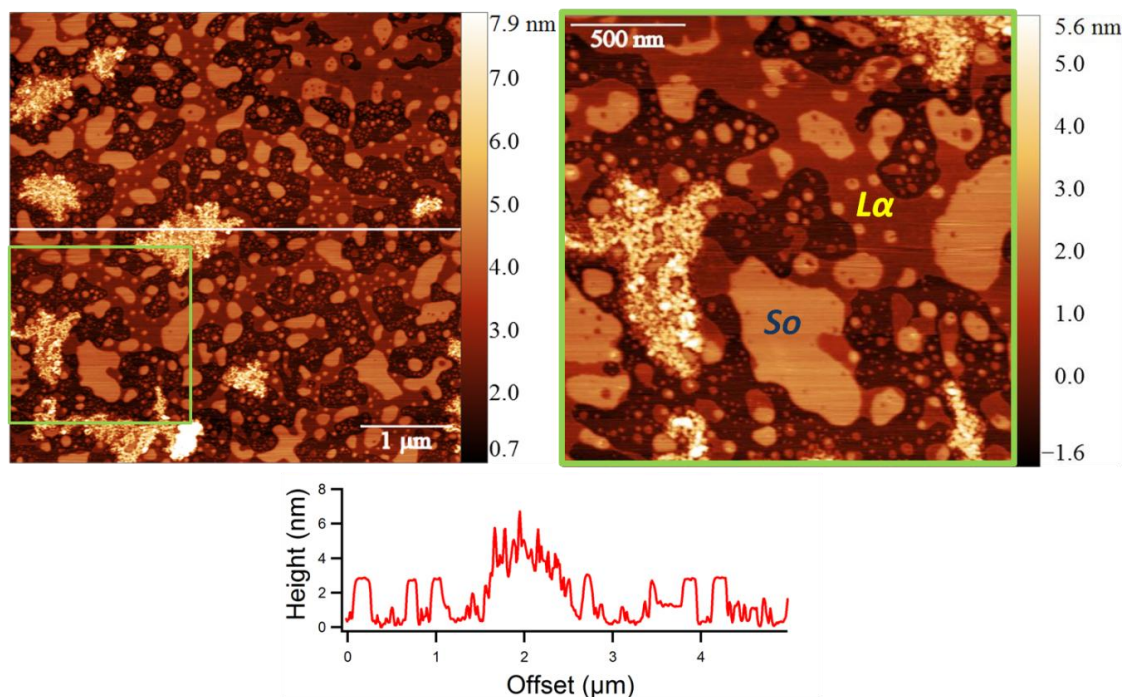


**Figure 49.** The interaction of FL-PrP-MA with raft-like model membrane after 12 hours. The membrane is highly damaged, and oligomer clusters appear of bigger size following the increase in dimension of lipid rafts (So phase).

## 8.5 Discussion

The application of direct vesicle fusion method for the preparation of SLBs allowed to perform a comparative analysis with the drop-casting technique in order to explore the potentialities of both methods for the fabrication of complex membrane model systems. Although drop-casting is an easy and fast technique, the control of lipid composition and morphology is hard to be obtained. Vesicle fusion instead shows great advantages in terms of reproducibility, quality of the membrane and the possibility to create model systems with several lipid components. At variance with drop-casting, binary and ternary complexes of high quality were produced with a success rate of 90%, showing a very good control of lipid composition and the presence of well-separated lipid phases. Moreover contaminating residues, which characterize the SLBs made via drop-casting, are completely absent in membranes produced via vesicle fusion, allowing to introduce further protein components in the membrane and to study the distribution of nanometric molecular elements. Another relevant quality of SLB produced by direct vesicle fusion is that they are always kept in liquid buffer, without any passage through air, as in the case of drop-casting. The formation of the bilayer at near-physiological conditions ensures to study lipid phase behavior and lipid-biomolecule interactions without any artifacts caused by the air-water transfer. The investigation of membrane stability in liquid buffer showed that raft domains change their

morphology over the time, forming domains of progressively bigger dimension. This effect was not present in SLB created from drop-casting, highlighting that lipid diffusion, which is responsible for domain reorganization, is guaranteed only in membranes produced via vesicle fusion. Taking into account advantages and disadvantages of both methods, we agree with most of the literature, saying that vesicle fusion has to be considered the method of choice in membrane nanotechnology<sup>286</sup>.

Once created and selected the best raft-like model systems, I complicated further the scenario by adding a new molecular component to the DOPC, SM cholesterol mixture to create a new bilayer. I first studied the interaction and distribution of GM1 gangliosides on membranes. Several studies have shown that GM1 has a relevant role in many cellular and pathological processes, such as the segregation and processing of the prion proteins. Therefore, the possibility to exploit a complex model membrane that includes these functional molecules is a promising tool to investigate biological processes involving lipid raft domains. I produced membrane characterized by 1% and 2.5% molar concentration of GM1 molecules. AFM images showed that GM1 forms small nanodomains of 1-2 nm in height which preferentially localized on ordered domains of membrane. The distribution was similar for both GM1 concentrations, however at 2.5% GM1 the membrane displays a higher density of nanodomains compared to the sample with 1% GM1. This support the idea that GM1 at higher concentration could in somehow modulate the organization of membrane raft domains.

Then, for the first time in the literature, I tested the ability of lipidated-anchor full-length Prion protein (FL-PrP<sup>C</sup>-MA), a membrane-binding protein which in pathological conditions form aggregates responsible for Prion disease, to interact with raft-like model membranes. I tested in particular the effect of the C-terminal membrane anchor (MA) on the activity of the protein and on membrane-binding capability. A great interest in C-terminal membrane attachment of PrP<sup>C</sup> via GPI-anchor has been grown in the last years because it is the mechanism which targets the protein to the extracellular surface of cell membrane and has a presumed role in the conversion of PrP<sup>C</sup> into the toxic scrapie isoform which leads to the formation of aggregated species. The protein was modified by a semisynthetic approach which provides several advantages over the other classic strategies<sup>301,304</sup>. Exogenous proteins usually expressed in high amount in bacterial systems lack of post-translational modifications. This limitations can be overcome by producing the protein in insect systems, but the yield of protein production is not satisfying. Another approach consists to the isolation of GPI-anchor PrP<sup>C</sup> from neurons but contamination with other compounds such as lipids and even misfolded PrP<sup>C</sup> cannot be excluded. The advantage of semisynthetic MA attachment strategy is that the full-length protein is in its native conformation, ready for single molecule investigation. Great efforts have been made to monitor the protein binding and aggregation on membrane of small PrP<sup>C</sup> peptides by AFM<sup>305</sup> and scanning tunnel

microscopy (STM)<sup>306</sup> but these protein structures clearly are an underestimated representation of the real protein, and do not represent either the structure and the activity of the full-length protein. The application of AFM to study the FL-PrP<sup>C</sup>-MA distribution on raft-like membrane, as well as, the role of lipids in the aggregation process, is a smart strategy because it allows to perform single molecule-like analysis at the nanoscale with small amounts of protein. AFM imaging showed that FL-PrP<sup>C</sup>-MA interacts with lipid raft domains without affecting the fluid phase of the bilayer. This could be due to the MA activity, which targets the protein to the ordered islands of membrane. However, formation of aggregated protein clusters which might resemble oligomer accumulation are observed. Since that the inter-molecular interactions among PrP molecules promote the formation oligomers, we cannot exclude that this effect is caused by the increase of local concentration of the protein on rafts via MA targeting. The concentration of PrP has been shown to play a role in the aggregation process<sup>307</sup>. One study has demonstrated that full-length recombinant PrP display different behavior according to the concentration of the protein incubated on SLBs made of POPC (1-palmitoyl-2-oleoyl-sn-glycero-3-phosphocholine) and POPS (1-palmitoyl-2-oleoyl-sn-glycero-3-phospho-L-serine)<sup>308</sup>. At high concentration (400 nM) PrP monomers formed sponge-like aggregates of 3-5 nm in height, whereas at very low concentration (4 nM) the formation of flat PrP layer of 2 nm in height was observed. In my case the protein was incubated at intermediated concentration (25 nM) a condition which does not allow to extrapolate the singular contribution of MA and protein concentration in the activity of PrP interacting with the SLB. For that reason, additional experiments at very low FL-PrP<sup>C</sup>-MA concentration will be performed, to better elucidate the behavior of this lipidated-protein on raft-like model membranes and gain new insights into the role MA in prion conversion and aggregation.

## 9. Iron-mediated interaction of Alpha Synuclein ( $\alpha$ S) with lipid raft model membranes

After having studied lipid raft formation in SLBs and their interaction with gangliosides and lipid-tailed proteins, in the third part of my thesis project I focused on the study of the interactions of proteins relevant as mediators of neural signaling, as alpha synuclein ( $\alpha$ S), with lipid rafts. My attention was in particular directed towards the mechanisms of  $\alpha$ S aggregation and on the influence that metals as iron (II) can have on it. The role of lipid rafts in the central nervous systems (CNS) is in fact known to be critical. They are implicated in neuronal signaling, neuronal cell adhesion and axon guidance<sup>90</sup>. Moreover, the involvement of lipid rafts in the biological functions of  $\alpha$ S has been reported in several works: lipid rafts are enriched in both pre-synaptic and post-synaptic sites of neurons and play a key role in organizing the synaptic proteins that modulate the homeostasis of vesicle exocytosis for neurotransmitters release<sup>90</sup>. In this respect,  $\alpha$ S is enriched at the presynaptic terminals of neurons and is thought to be localized on lipid rafts, where it supports the correct assembly and disassembly of synaptic vesicles, by interacting with the SNARE proteins<sup>213,309</sup>. Recently, some evidences have shown that iron and other metal ions can modulate  $\alpha$ S expression and promote *in vitro* aggregation of  $\alpha$ S by inducing the formation of stable metal- $\alpha$ S complexes, impairing the  $\alpha$ S function<sup>226,230</sup>. Aggregates of  $\alpha$ S are in fact globally recognized as one of the key molecular events that contribute to the development and progression of neuro-degeneration<sup>310</sup>. Although the structural details as well as the conditions which induce  $\alpha$ S aggregation have not completely understood, it is accepted that metals favor this process<sup>311</sup>. Iron in particular is a biological essential element being implicated in the electron transfer during cellular respiration and as cofactor in the catalysis of enzymatic reactions. At the same time iron is potentially toxic when is present at high concentrations in the cell. It has been demonstrated that the total amount of iron increases physiologically in the brain with age and that this fact could be correlated with the old-age onset of PD<sup>227</sup>.

In this context, I was therefore interested in understanding the effect of iron in promoting structural changes in  $\alpha$ S bound to membranes. I used AFM to characterize protein aggregates of wild-type  $\alpha$ S and of a mutant form of  $\alpha$ S, the A53T, responsible for an early stage familiar development of PD and more prone to aggregation. Successively, I produced lipid rafts in SLBs by direct vesicle fusion and investigated the effect of the protein-membrane interaction before and after metal treatment.

## 9.1 In vitro iron-mediated aggregation of $\alpha$ S

In order to evaluate the effect of iron (II) in promoting the aggregation of  $\alpha$ S, I performed an *in vitro* incubation of 100  $\mu$ g of 35  $\mu$ M wild-type  $\alpha$ S in presence of 2 mM FeCl<sub>2</sub> salt solution. These values of concentration for the protein and the metal have been chosen in accordance with a previous study of *in vitro* aggregation of the protein mediated by metals, performed by Uversky and colleagues<sup>226</sup>.

First, I studied as a reference the behavior of the bare wild-type  $\alpha$ S, deposited on mica after 1 h shaking in Milli-Q water at 37° C (see Methods) measured by tapping-mode AFM imaging in air. As can be seen from Fig. 50 A, there is a homogeneous background from which what resemble sparse protein aggregates protrude. The roughness of the background is about  $161.7 \pm 13.4$  pm, slightly higher than the roughness of bare mica measured in the same conditions ( $122.1 \pm 7.3$  pm). This is consistent with a mat of non-aggregated wt  $\alpha$ S. The globular aggregates have heights in the range 2-6 nm: the sparse presence of aggregates is clear in the topographic image and in the line profile reported in Fig. 50 A-C but it is not evident in the height histogram in Fig. 50 B, due to the small number of globular proteins. The aggregation in this case is probably caused by the shaking step.

Then wt  $\alpha$ S has been incubated for 1 h in the same conditions (Milli-Q-H<sub>2</sub>O at 37° C) but in the presence of iron, and deposited on mica (Fig. 50 D). AFM images show the formation of globular aggregates compatible with protein oligomeric species. The height distribution of the spots related to the protein shows the presence of two main populations of oligomers, with heights of about 3-4 nm and 7 nm respectively (Fig. 50 E) (the fitting curve evidences the two Gaussian distributions of aggregates, peaked at 3 and 7 nm). This result confirms the role of iron (II) ions in inducing  $\alpha$ S aggregation.

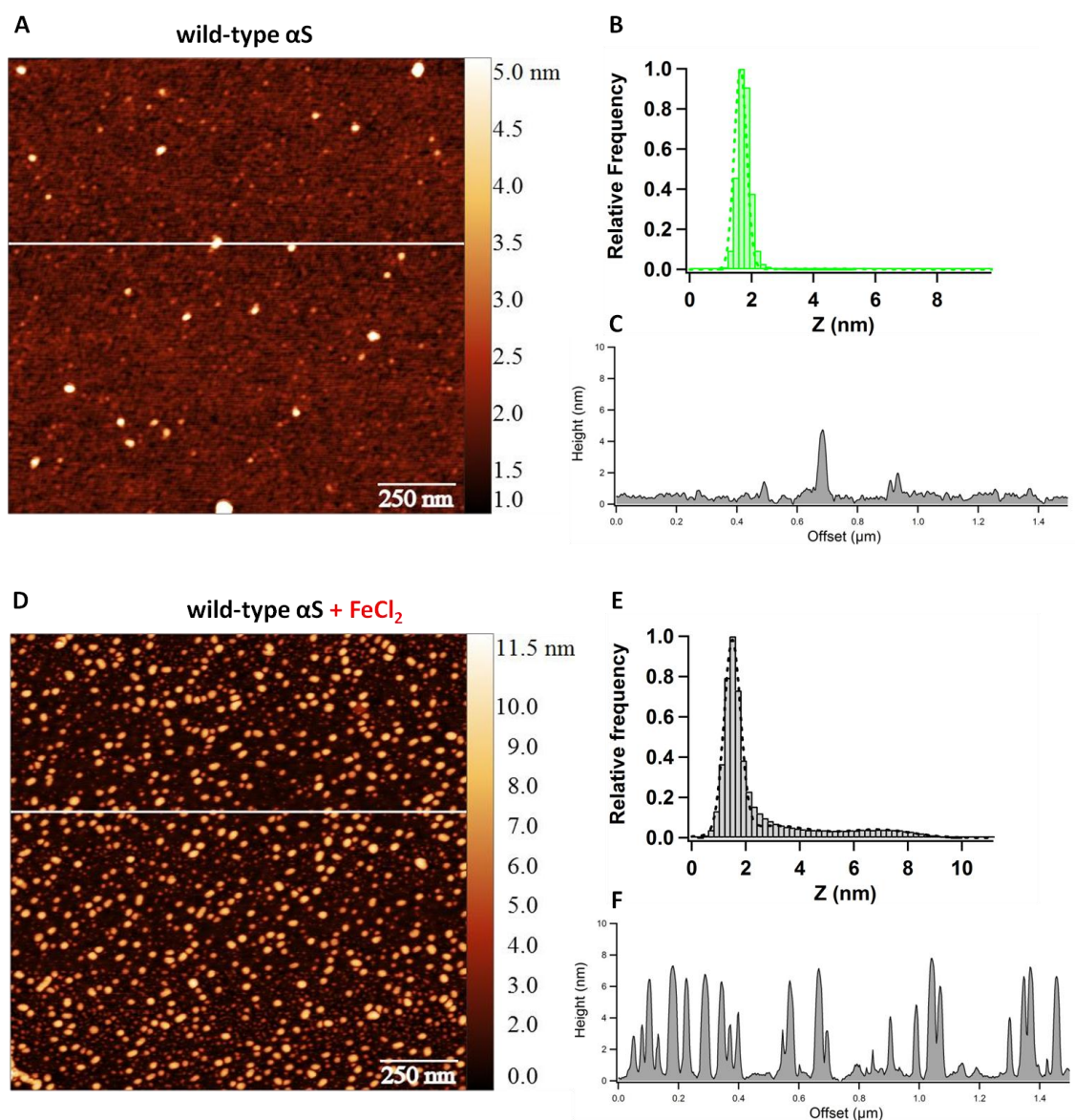


**Figure 50. AFM-characterization of the iron-mediated aggregation of wild-type  $\alpha$ S.** (A), (B), (C) show respectively AFM topography, height distribution and height profile of wild-type  $\alpha$ S oligomers after incubation in Milli-Q  $H_2O$ . (D), (E), (F) represent the same analysis made on wild-type  $\alpha$ S oligomers after the treatment with 2 mM  $FeCl_2$ . AFM images were collected in tapping-mode in air.

At this point, I repeated the same type of experiments just described to in the case of the A53T  $\alpha$ S mutant. The AFM image of Fig. 51 A shows that 1h incubation of A53T  $\alpha$ S in Milli-Q  $H_2O$  produces the formation of bright features of 2-6 nm height, compatible with globular protein aggregates, a situation very similar with the previous experiment of the wt  $\alpha$ S. Even in this case, the presence of few aggregates over the area of mica is underlined by the AFM topographic image and the line profile (Fig. 51 A, C). Here, the roughness of the background is about  $189.4 \pm 11.7$  pm, 1,5-fold the one of mica, possibly indicating the presence of non-aggregated proteins, not visible in the AFM topography image. Conversely, iron induces a strong protein aggregation (Fig. 51 D), more pronounced with respect to the wt  $\alpha$ S case. Globular aggregates can be classified as protein

oligomers exhibiting a normal distribution with a mean value peaked around 9 nm as highlighted in the height distribution graph (Fig. 51 F).

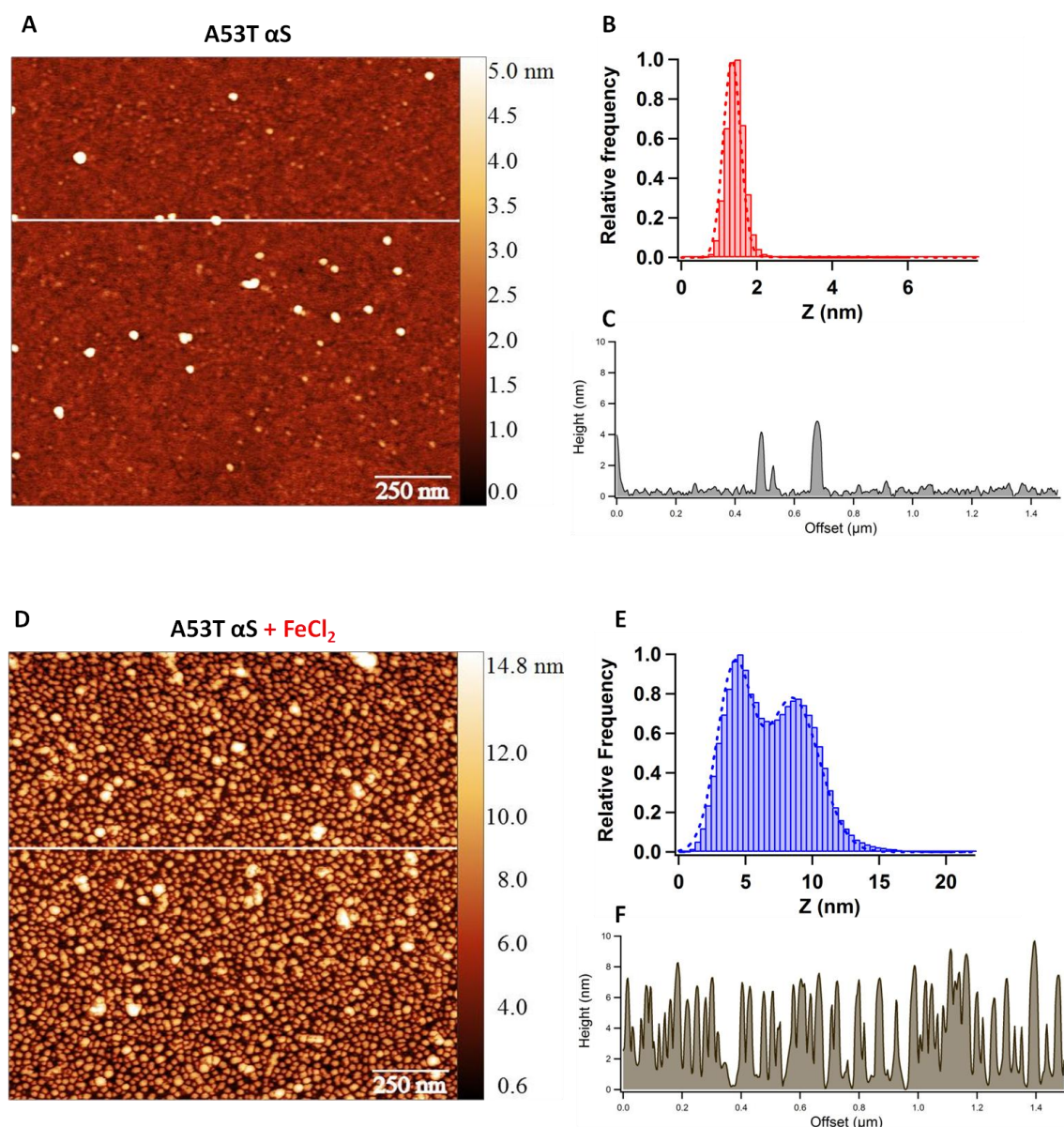


**Figure 51. AFM-characterization of the iron-mediated aggregation of mutant A53T  $\alpha$ S.** (A), (B), (C) show respectively AFM topography, height distribution and height profile of mutant A53T oligomers after incubation Milli-Q  $H_2O$ . (D), (E), (F) represent the same analysis made on the mutant A53T after treatment with 2 mM  $FeCl_2$ . AFM images were collected in tapping-mode in air.

The effect of iron on protein aggregation is very fast: oligomers form already after 1 h incubation, both in the case of wild-type and A53T mutant  $\alpha$ S. However, the aggregation is more pronounced for the mutant and is characterized by a larger amount of oligomers with bigger dimensions compared to the wild-type  $\alpha$ S. After this preliminary test, I moved on to study the interaction of iron with membrane-bound  $\alpha$ S.

## 9.2 Interaction of monomeric $\alpha$ S with lipid raft model membranes

In order to evaluate the effect of  $\alpha$ S binding to a model lipid bilayer mimicking lipid raft domains, I produced a planar lipid bilayer composed by DOPC, SM (66:33) and 5% cholesterol following the same recipe described in paragraph 8.1. At variance with the experiments described in chapter 8, in which the interaction of the GM1 ganglioside and the lipidated PrPc with lipid rafts, respectively, were studied, here we removed any presence of metal ions in solution by washing repeatedly the SBL (prepared from vesicle fusion with 5mM  $\text{CaCl}_2$ , see the protocol described in Materials and Methods) prior to insert the  $\alpha$ S protein. By incubating  $\alpha$ S in Milli-Q water at nominal pH of 7.0, in fact, I wanted to discard any possible ion-induced protein conformation more prone to aggregation. In this way, by starting with almost 100% of the soluble, monomeric, unstructured conformation of  $\alpha$ S, I could address more precisely the role of Iron (II) ions in promoting  $\alpha$ S aggregation.

The binding of the protein was monitored vs. time, as previously described, by tapping mode AFM imaging in liquid environment. This approach allowed us to visualize and study submicrometric raft domains and to investigate the localization of the protein in interaction with the membrane. The Milli-Q water-washed SBL, imaged in pure Milli-Q, is shown in Fig 52 A. In analogy with the image shown in Fig. 41 A (chapter 8) corresponding to a membrane with the same composition, here I observed two phases separated in height of  $1.2 \pm 0.2$  nm. On this membrane, 100  $\mu\text{g}$  of 35  $\mu\text{M}$  wild-type  $\alpha$ S (final concentration = 4.5  $\mu\text{M}$ ) was incubated for 1 hour and then the surface was imaged again by AFM.

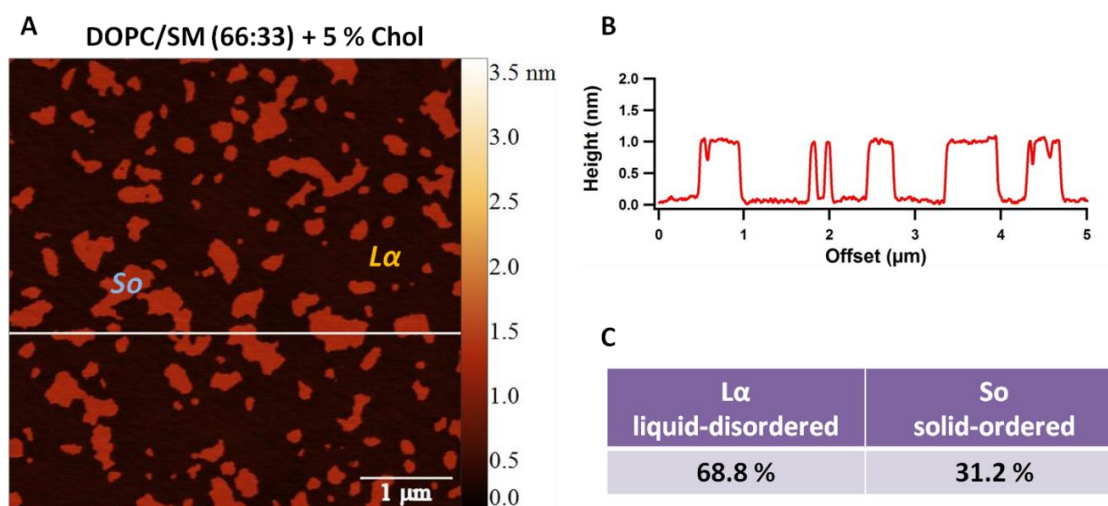


**Figure 52. AFM topography of lipid raft model membrane.** The image shows the topography of artificial lipid bilayer made by DOPC/SM (66:33 mol:mol) + 5% cholesterol (mol). The membrane is characterized by the coexistence of the two lipid phases ( $L\alpha$  and  $So$ ). **(A)** Surface topography. **(B)** Height profile. **(C)** Percentage of  $L\alpha$  and  $So$  phase. AFM images were acquired in tapping-mode in Milli-Q  $\text{H}_2\text{O}$  at room temperature.

The interaction between the monomeric wild-type  $\alpha$ S and the SLB (Fig. 53) seems to involve both lipid phases, ordered and disordered, with the formation of different types of defects in the membrane structure, which appears at different topographic heights in Fig 53 B.

The phase which protrudes with about 2 nm from the bottom height of the image can be attributed to the  $S_o$  phase. In fact, the surface coverage by this phase (29.8%) is in good agreement with the one of the starting SBL (31.2%). The roughness of the domains belonging to the  $S_o$  phase, however, shows a 2-fold increase in the presence of the monomeric protein. The AFM topographic image indicates the presence of pore-like defects as well as of bright spots (blue arrows in Fig 53 A) which might be assigned lipid-protein complexes and to protein aggregates, respectively. On the other hand, the  $L\alpha$  phase exhibits larger defect domains. The height difference between these new defects and the  $L\alpha$  phase is about 0.8 nm that could be caused by lipid-extraction and/or direct interaction of  $\alpha$ S with the bottom layer of the SLB in alpha-helix conformation parallel to the membrane plane.

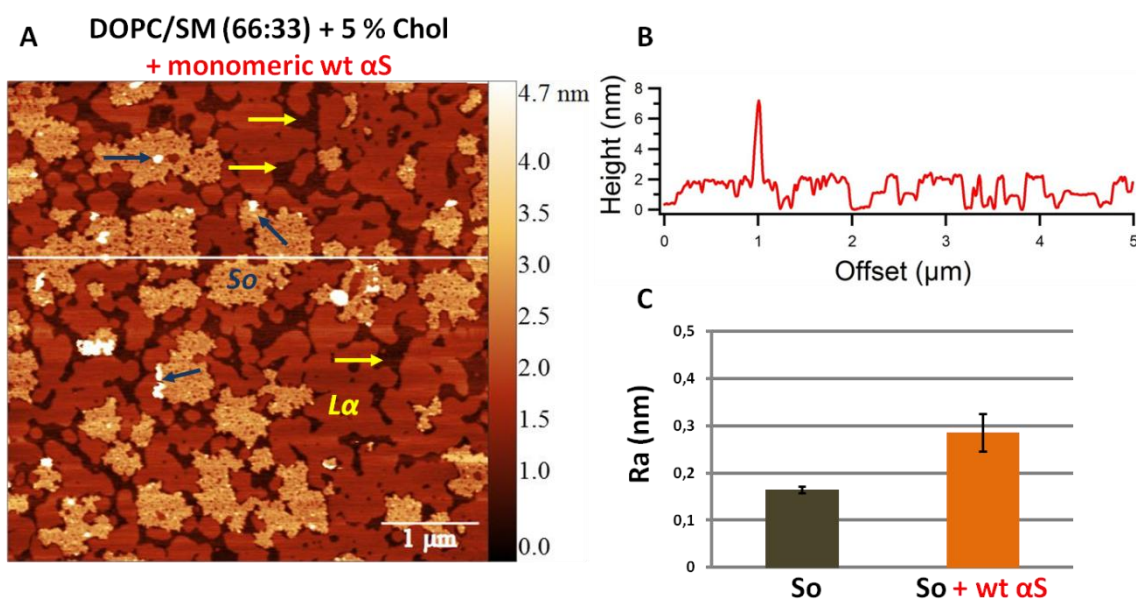


**Figure 53. AFM topography of lipid raft model membrane incubated with monomeric wild-type  $\alpha$ S.** (A) The protein (4.5  $\mu$ M) interacts with both lipid phases in different manner. Raft-like domains ( $S_o$  phase) are characterized by indented borders and small protein aggregates (blue arrows). Larger defects are present on DOPC ( $L\alpha$  phase) (yellow arrows). (B) Height profile. (C) Change in the roughness (Ra) of ordered domains shows the presence of  $\alpha$ S interaction. Image were collected in tapping-mode in Milli-Q  $H_2O$  at room temperature.

We then tested the interaction between the mutant A53T  $\alpha$ S monomers with the model membranes characterized by the same lipid composition of the previous experiment. Here we observed a different behavior with respect to the case of wild-type  $\alpha$ S.

Apart from white, aggregated phases, we observe one single type of defect. The total area covered by the highest, large domains (29.2%) is similar to the original area occupied by the  $S_o$

phase before introducing the protein (see Fig. 52). The roughness of So phase remains significantly the same to indicate that the interaction between A53T  $\alpha$ S and the SBL does not occur at the level of So domains. About the 38.5% of the total membrane area is now covered by a new phase, with a height lower of about 1 nm with respect to the L $\alpha$  phase. On the contrary, a 5-fold variation of the roughness of the L $\alpha$  phase points towards the hypothesis of a preferential interaction of the A53T mutant protein with the DOPC phase. We can also note the presence of small white spots (yellow arrow in Fig. 54 A) that could be assigned to protein aggregates. Such domains are much smaller in size and height than the ones seen in Fig. 53 (and also with respect to brighter spots in the same figure).

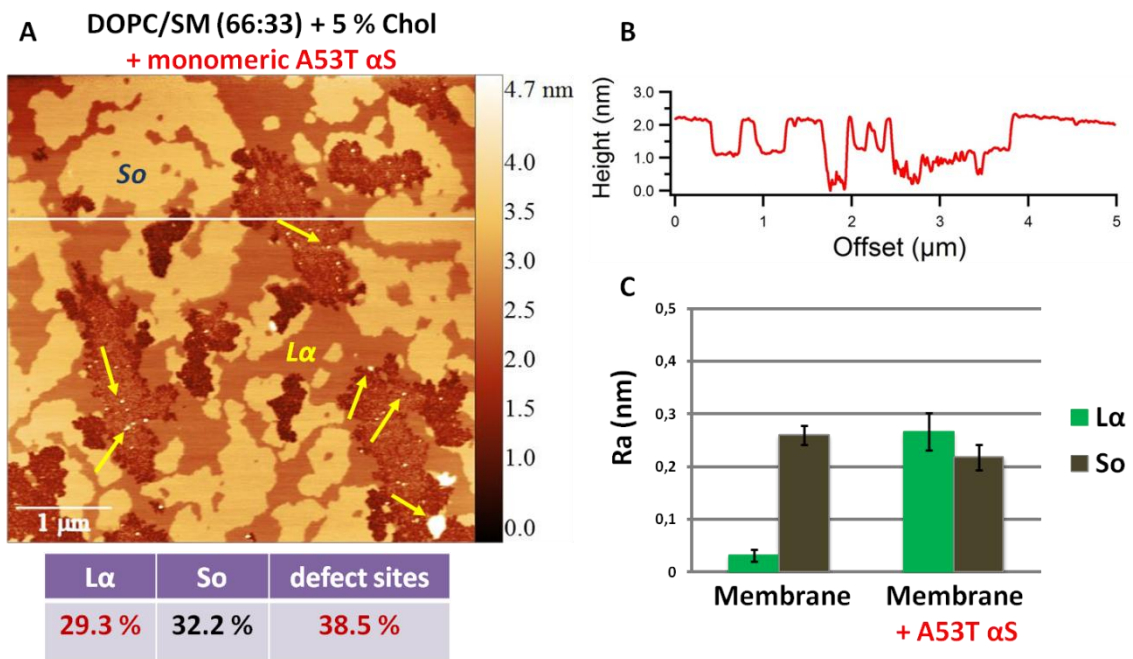


**Figure 54. AFM topography of lipid raft model membrane incubated with monomeric A53T  $\alpha$ S.** (A) The protein (4.5  $\mu$ M) interacts preferentially with the DOPC (L $\alpha$  phase). Defect sites with white spots of aggregation are largely distributed and extended (yellow arrows). (B) Height profile. (C) Change in the roughness (Ra) of the L $\alpha$  phase confirms the interaction of the protein with DOPC. No variation of Ra occurs for lipid rafts (So phase). AFM Images were acquired in tapping-mode in Milli-Q H<sub>2</sub>O at room temperature.

### 9.3 Interaction of iron-induced oligomers of $\alpha$ S with lipid raft model membranes

In order to assign a biological relevance to the  $\alpha$ S oligomers complexated by iron ions, we tested these aggregated species on model membranes with the same composition as described previously. Again, I investigated the  $\alpha$ S-iron (II) oligomer-membrane interaction by AFM in Milli-Q water. Here, we observed a totally new scenario. The 7 nm average size globular aggregates observed on bare mica in Fig. 50, are now coalescing on lipid raft domains, forming clusters of globular protein aggregates of 200-500 nm in diameter (Fig. 55 A). The AFM zoom-in image (Fig. 55 B) shows that the borders of such oligomer clusters have a height value that matches very well with the height of raft domains, strengthening the hypothesis that the interaction of the protein cluster with the membrane occurs on  $S_o$  phase only. To further support it, we can notice that the roughness on the two phases does not change (data not shown). Surprisingly, the accumulation of the oligomers does not involve all lipid raft domains, underlying a probably cooperative mechanism which mediate this kind of membrane-protein interaction.

The incubation of oligomers of the mutant A53T  $\alpha$ S with the SLB shows similar results (Fig. 56 A-B). The presence of clusters of aggregated oligomers can be observed also in this case.

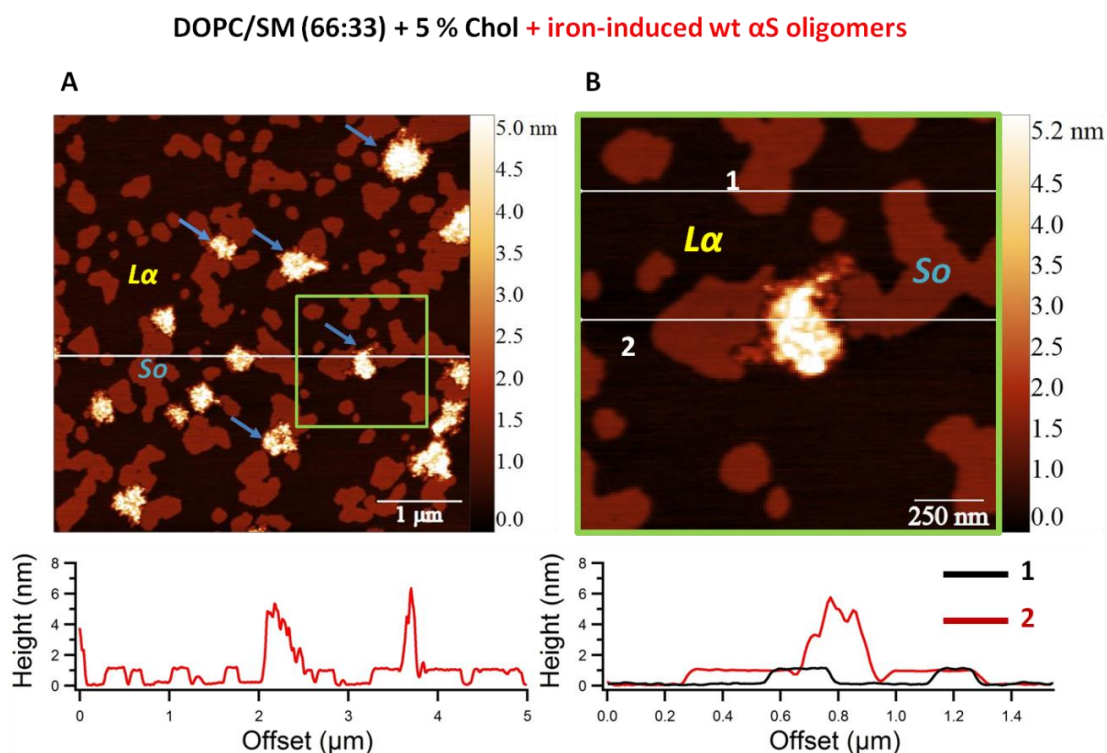


**Figure 55. AFM topography of lipid raft model membrane incubated with iron-induced oligomers of wild type. (A-B)** AFM topographic images were acquired in tapping-mode in Milli-Q  $H_2O$  at room temperature.

DOPC/SM (66:33) + 5 % Chol + iron-induced A53T  $\alpha$ S oligomers

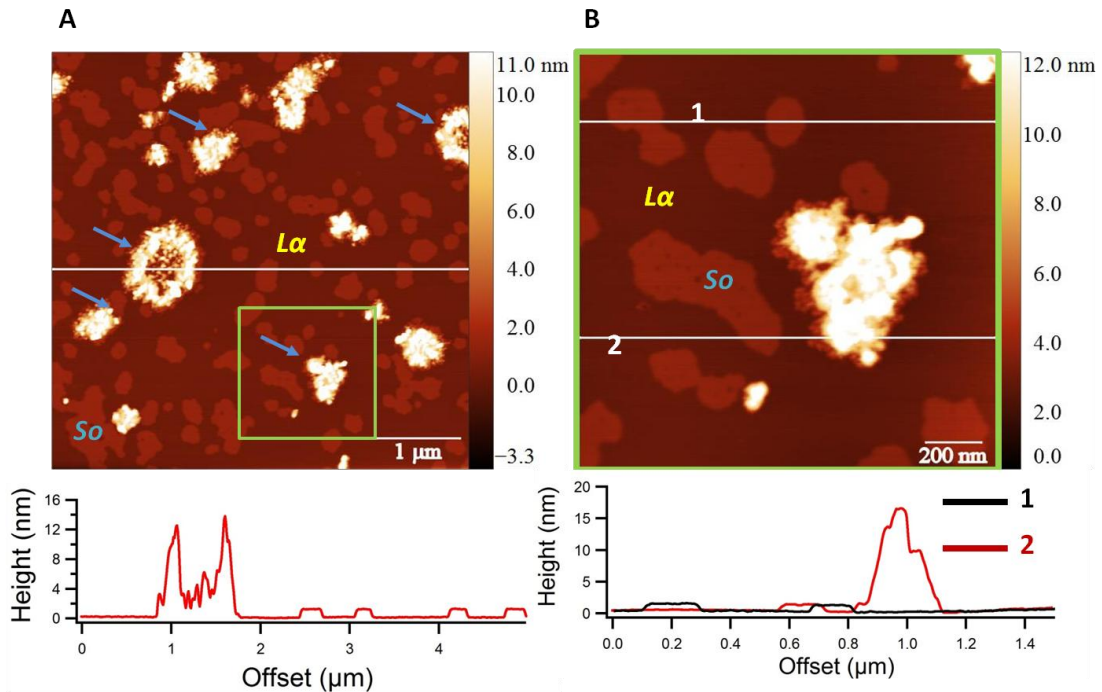


**Figure 56.** AFM topography of lipid raft model membrane iron-induced oligomers of mutant A53T  $\alpha$ S. (A-B) AFM topographic images were acquired in tapping-mode in Milli-Q  $H_2O$  at room temperature.

However, the mutant A53T  $\alpha$ S-iron (II) aggregates show a more aggressive behavior: they form bigger size clusters, which now can reach lateral dimensions up to 1000 nm (Fig. 57 B) and higher heights (2-fold increase than wt). The total surface coverage of A53T oligomer clusters is around 3-fold higher than for the wild type  $\alpha$ S oligomers (Fig. 57 A-B). In addition, I noted the presence of two populations of oligomeric clusters on A53T  $\alpha$ S sample. The first one is represented by small, circular and totally filled clusters which are similar to those found on the wild type  $\alpha$ S sample. The second one consists of bigger annular clusters, which are characterized by a thick ring of oligomers with a central empty space. These ring-shape structures might give us information on the mechanism by which clusters are formed on membranes. They could assembly starting from a preferential interaction of oligomers at the borders of raft domains which could act a docking site for a subsequent recruitment of the oligomers present in solution.

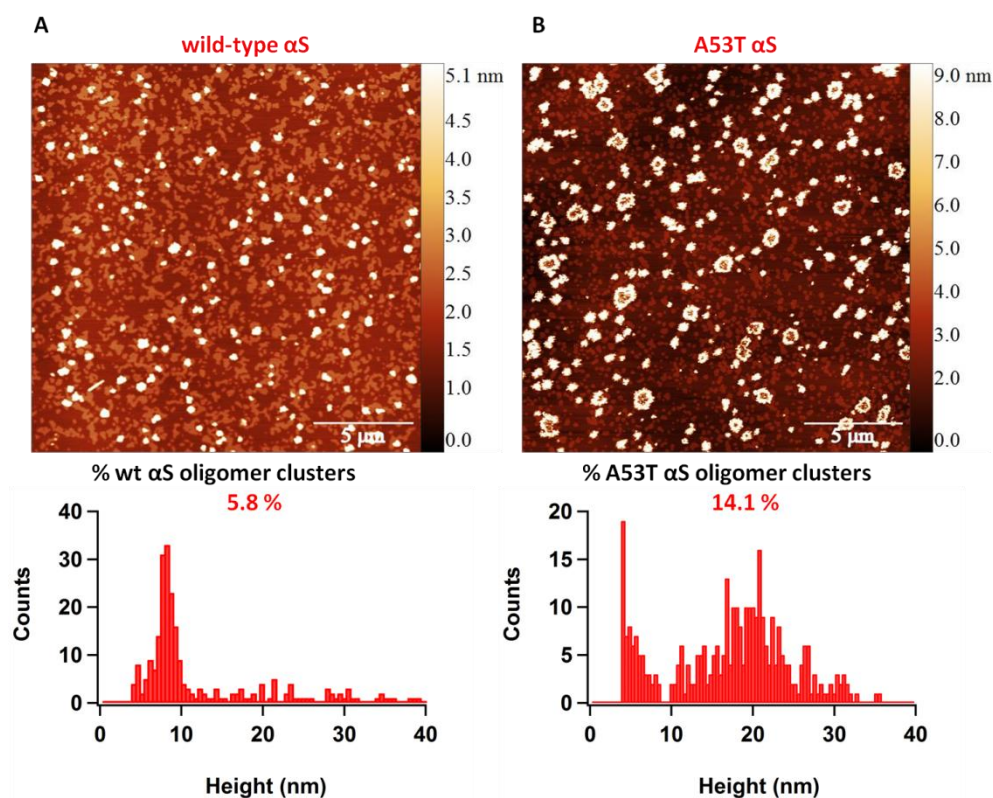


**Figure 57. AFM topography and distribution of height of iron-induced oligomers of wild type (A) and mutant A53T αS (B).** AFM Images were collected in tapping-mode in Milli-Q H<sub>2</sub>O at room temperature.

#### 9.4 Attenuated total reflectance infrared spectroscopy measurements

In order to complement AFM data on iron (II) effect on αS-aggregation and interaction with raft-like membranes, I performed infrared (IR) spectroscopy measurements. In particular, I used FTIR-ATR (Fourier-transformed IR in attenuated total reflectance conditions), a technique which provides valuable information about protein secondary structure and dynamics of lipid-protein interactions. Moreover, ATR provides excellent quality data in conjunction with the best possible reproducibility of any IR sampling technique. All measurements were performed in air, using a germanium crystal with 25 internal reflections as substrate.

In Fig. 58 IR absorbance spectra of the oligomers of wt and mutant A53T αS, respectively, formed in solution in the presence of iron (II) ions (FeCl<sub>2</sub> solution, same conditions as in paragraph 9.1, 1h incubation time) and deposited on the Ge crystal, are shown. IR spectra show interesting results in the spectral region between 3050 and 2800 cm<sup>-1</sup>, characterized by the C-H stretching (symmetric and asymmetric) vibration of CH<sub>2</sub> and CH<sub>3</sub>, which can be found in the side chains of aliphatic amino acids. Wt αS displays stronger peaks at 2919 cm<sup>-1</sup> (asymmetric stretching of CH<sub>2</sub>) and at 2851 cm<sup>-1</sup> (symmetric stretching of CH<sub>2</sub>) which highlight a greater vibrational freedom of wt protein compared to the mutant species. At the same time, the mutant A53T shows a broadening

and a shift of  $\text{CH}_2$ - $\text{CH}_3$  asymmetric stretching peaks which can be correlated to a bigger structural disorder of the protein.

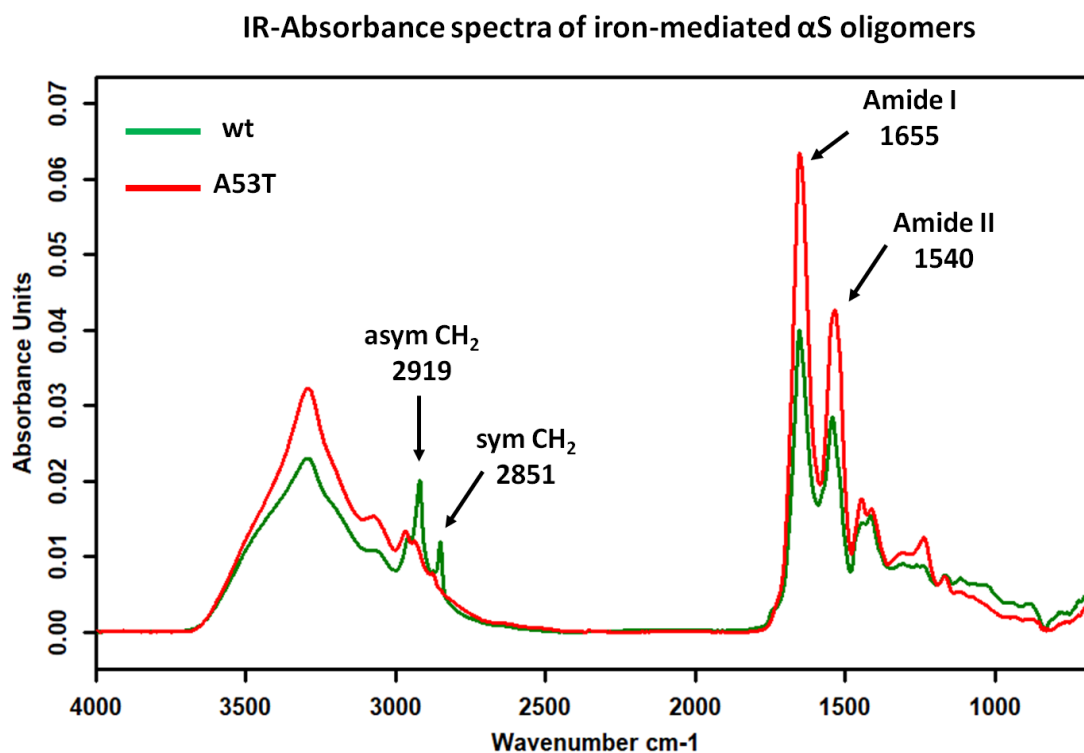


**Figure 58.** The absorbance spectra of iron-mediated  $\alpha\text{S}$  oligomers. Wt  $\alpha\text{S}$  (green) and mutant A53T (red) were treated for 1 h with a solution of 2 mM  $\text{FeCl}_2$ .  $\text{CH}_2$  asymmetric and symmetric stretching of wt can be observed at 2919  $\text{cm}^{-1}$  and 2851  $\text{cm}^{-1}$ , respectively. The measurements were performed in air in the mid-infrared region (approximately 4000-750  $\text{cm}^{-1}$ ).

Focusing on the amide I (1655  $\text{cm}^{-1}$ , the most intense absorption band in proteins, primarily governed by the  $\text{C}=\text{O}$  stretching vibration, is directly related to the backbone conformation) and amide II (1540  $\text{cm}^{-1}$ , derives mainly from in-plane  $\text{N-H}$  bending and  $\text{C-N}$  and  $\text{C-C}$  stretching vibrations and is conformationally sensitive) region of the IR spectra, similar broadening of peaks for the mutant A53T can be seen, confirming the presence of greater disorder in the structure of the protein (Fig. 59 A). The calculation of the second derivative of the absorbance spectra in this region highlights the predominance of  $\alpha$  helix structure in both proteins (1655  $\text{cm}^{-1}$ ), with other two peaks at 1640  $\text{cm}^{-1}$  and 1625  $\text{cm}^{-1}$  more pronounced in the mutant A53T with respect to the wt protein (Fig. 59 B). These components can be referred to a high content of random-coiled and parallel  $\beta$ -sheet structures, respectively. From these preliminary data, we can infer that the iron (II) induced mutant A53T aggregates already shown by AFM in the image of Fig. 51 are characterized by a bigger structural disorder and that aggregation is driven by the formation of  $\beta$ -sheet secondary structures, as in the case of  $\alpha\text{S}$  toxic oligomers and fibrils.

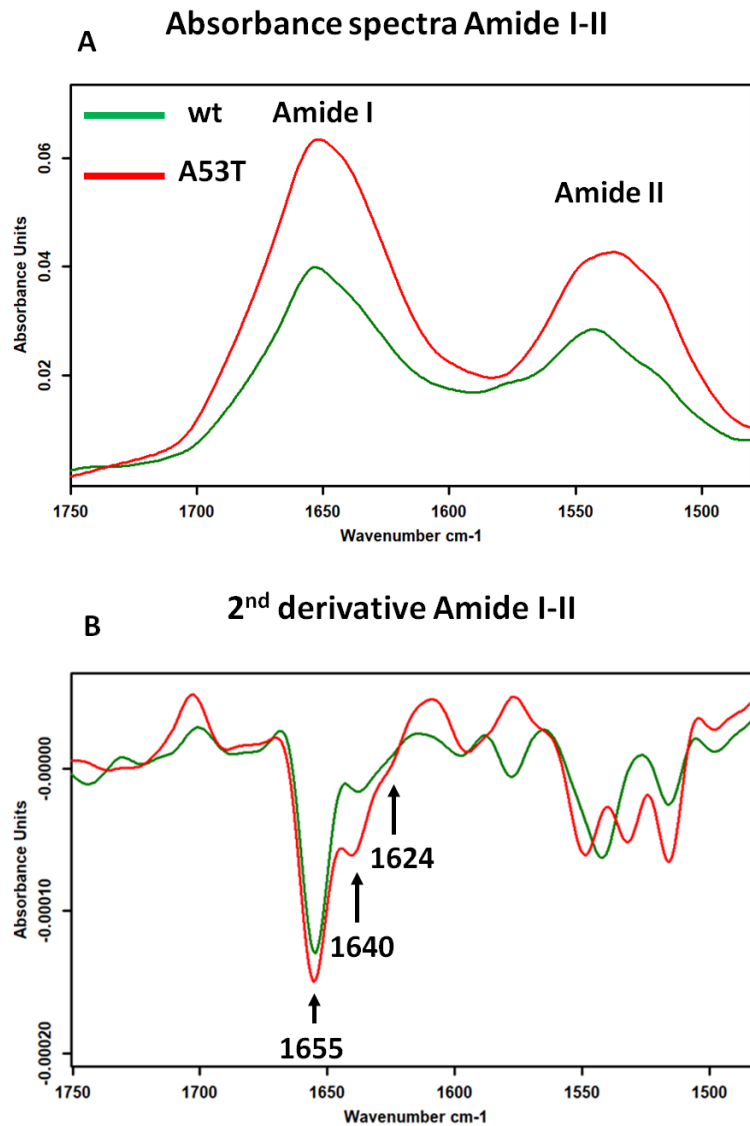


**Figure 59. The absorbance (A) and the second-derivative (B) spectra of amide I and amide II region.** The peaks at  $1640\text{ cm}^{-1}$  and  $1624\text{ cm}^{-1}$  highlight respectively the presence of higher contribution of random-coiled and  $\beta$ -sheets in the mutant A53T  $\alpha$ S.

Then, I focused on the interaction of both proteins with LUVs composed by DOPC/SM (66:33 in molar ratio) with 5% cholesterol (molar) in order to get insights about the behavior of the proteins interacting with membrane in absence of iron. In this experiment, LUVs and proteins were incubated at room temperature for 1 h, then the sample was spotted on the germanium crystal forming a thin film of lipid bilayer interacting with the proteins. The difference between this set of IR experiments and the AFM ones is then on the support substrate used. However, both of them, mica and germanium, are oxide surfaces. In first approximation then one can assume that the SBL should not be much different in the two cases, since the two surfaces are similar in terms of surface tension and wettability. After the evaporation of the solution, we recorded IR - absorbance spectra. From Fig. 60 it is possible to observe a strong absorption enhancement in the

region of 3050-2800  $\text{cm}^{-1}$  corresponding to the C-H bonds stretching vibration in  $\text{CH}_2$  and  $\text{CH}_3$ , of which lipid acyl chains are particularly rich, confirming the presence of the lipid membrane.

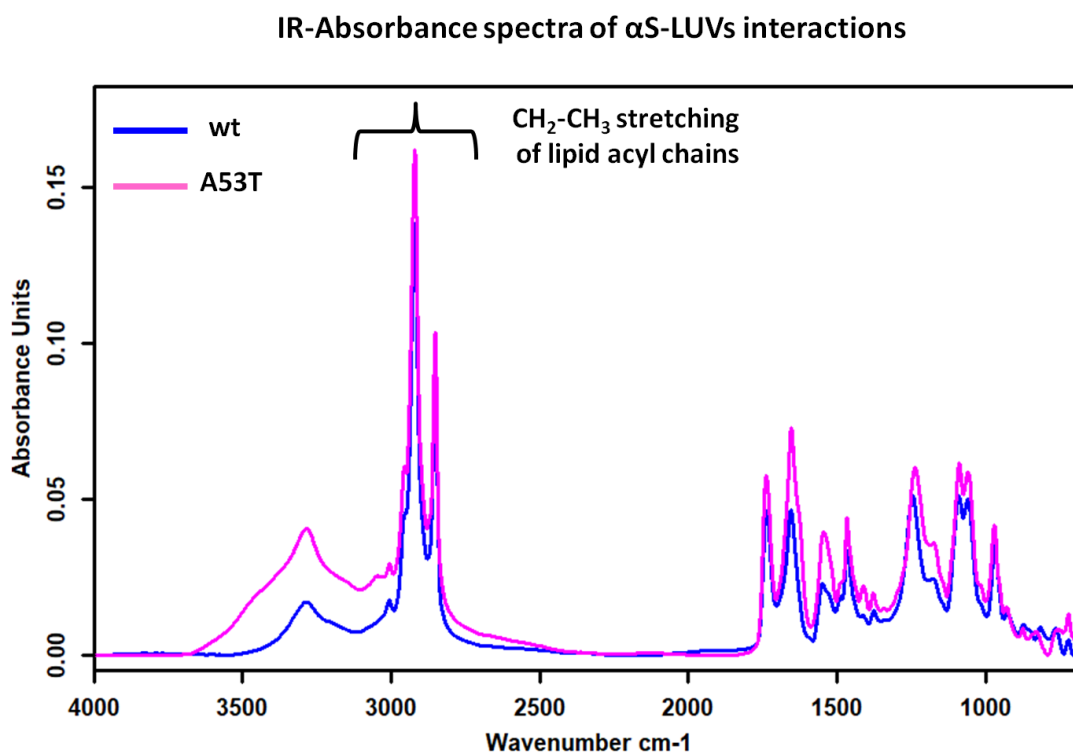


**Figure 60. The absorbance spectra of  $\alpha\text{S}$ -LUVs interactions.** The region of 3050-2800  $\text{cm}^{-1}$  shows the peaks related to the vibrational stretching of  $\text{CH}_2$  and  $\text{CH}_3$  group of lipid acyl chains. Wt  $\alpha\text{S}$  is reported in violet, the mutant A53T in blue.

The observation of amide I-II region (Fig. 61 A) shows the presence of a strong peak at 1626  $\text{cm}^{-1}$  in the case of mutant A53T  $\alpha\text{S}$ , which correlates with the presence of aggregation and which is almost absent in the case of wt  $\alpha\text{S}$ . The second derivative analysis of the same spectral region (Fig. 61 B) highlights, as in the case of aggregates on germanium, a prevalence of  $\alpha$ -helix content in the structure of both proteins. No random coil secondary structures are observed. However, the mutant species clearly shows pronounced components which can be associated to parallel and anti-parallel  $\beta$ -sheets (1624 and 1695  $\text{cm}^{-1}$ , respectively), and  $\beta$ -turn (1677  $\text{cm}^{-1}$ ).

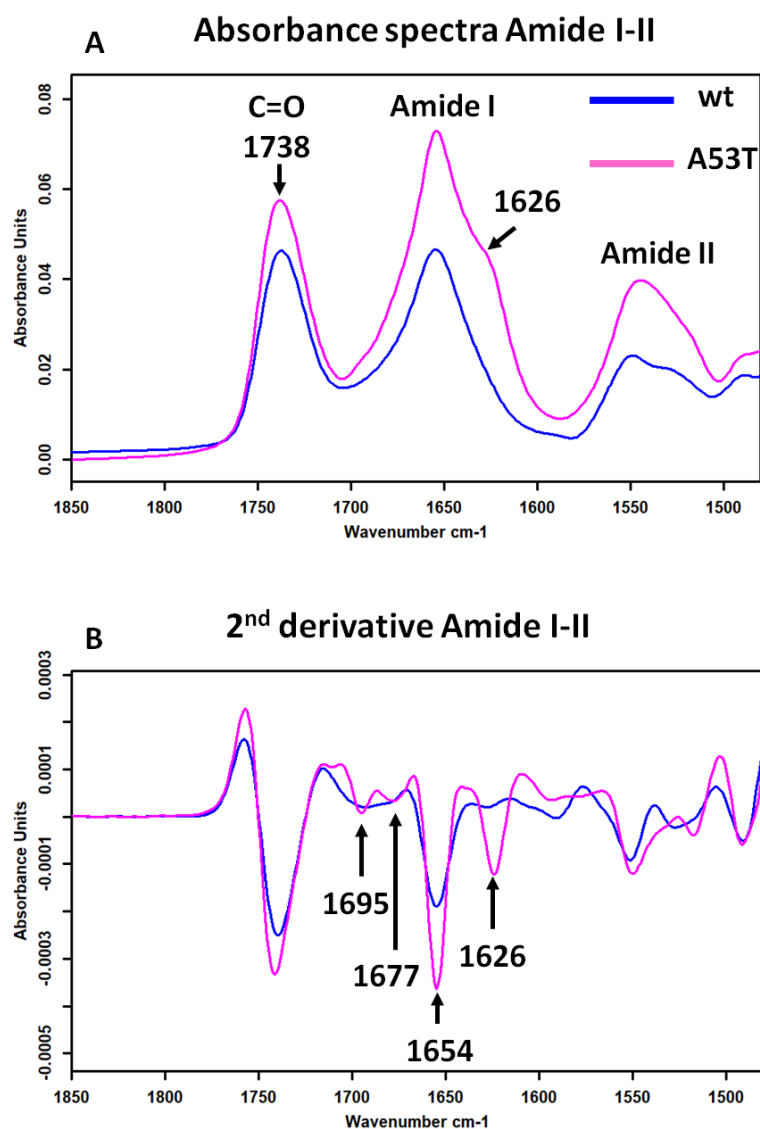


**Figure 61. The absorbance (A) and the second-derivative (B) spectra of amide I and amide II region.** The peak at 1738 cm<sup>-1</sup> represents the carbonyl stretching of lipids (C=O bond). As for the analysis of oligomers induced by iron, the mutant A53T is characterized by stronger peaks at 1695, 1677, and 1626 cm<sup>-1</sup> in the second-derivative spectra. These values are associated to anti-parallel  $\beta$ -sheets,  $\beta$ -turn and parallel  $\beta$ -sheets, respectively, highlighting an aggregation process mediated by lipid membrane.

Finally, a third set of measurement was performed on lipid vesicles incubated with iron-induced protein oligomers. Here, we concentrated on the region of 1300-1125 cm<sup>-1</sup> which display macroscopic difference between the two proteins. The IR-absorbance spectra show a difference in the peak corresponding to the vibrational stretching of organic phosphate groups of lipid headgroups (1230 cm<sup>-1</sup>) (Fig. 62 A). Wt  $\alpha$ S is characterized by a broadening of this peak compared to the mutant A53T. In order to check the role of iron in the change of the morphology of this peak, I compared the IR absorbance in this small spectral region of two controls: SLB alone and of SLB incubated with iron (in the absence of protein) (Fig. 62 B). The comparative analysis highlights

an interesting result. The bare membrane displays a peak which is similar to that recorded from iron (II)-mutant A53T  $\alpha$ S aggregates interacting with the membrane, whereas the broad peak of iron (II)-wt  $\alpha$ S aggregates on the membrane is more comparable to the one of the membrane incubated with iron. The shift and the broadening of this peak could be due to the effect of iron on lipid headgroups of membrane. The hypothesis is that the wt  $\alpha$ S have worst ability to bind iron which thereby remain free in the membrane in sufficient amount to interact with lipid headgroups. On the contrary, the mutant species seems to bind iron in greater amount or with a faster kinetics, forming a complex and leaving no iron ions free to interact with the phosphate groups, with an absorption fingerprint in this spectral region that is similar to the one of the membrane alone.

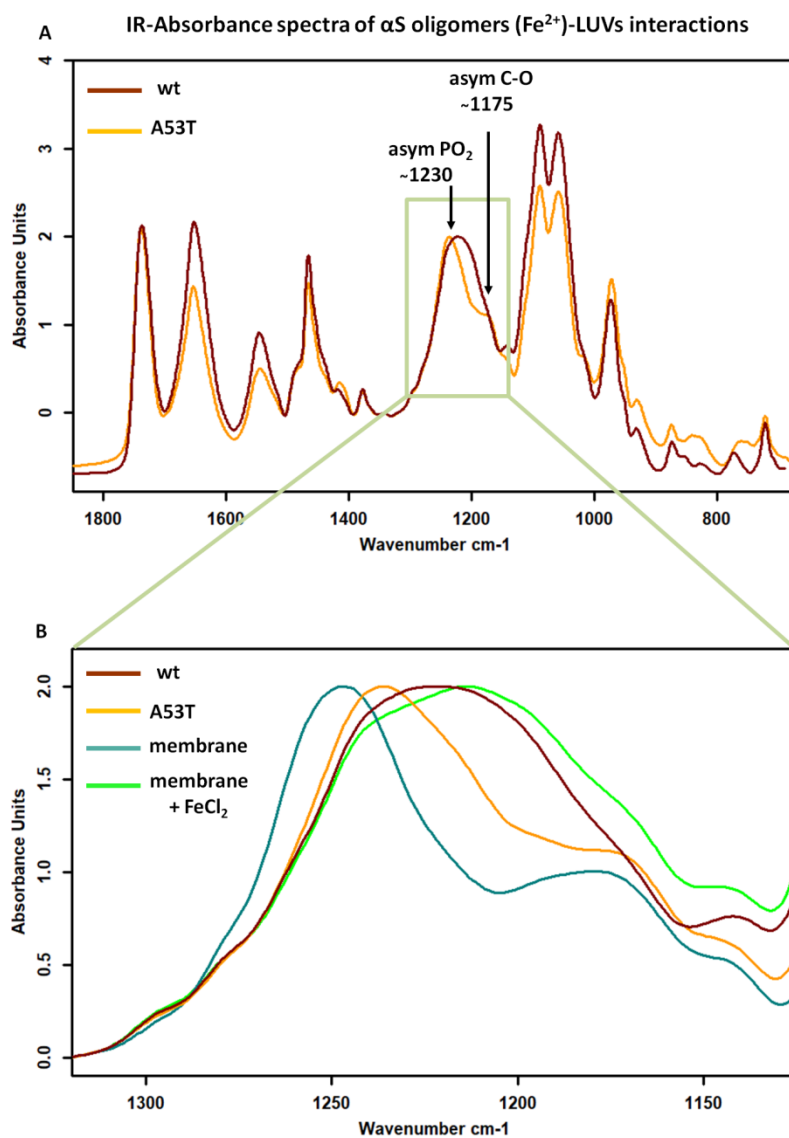


**Figure 62. The absorbance spectra of the interaction between iron-mediated oligomers with raft-like membrane (A).** A broaden peak is observed for the wt  $\alpha$ S in region of phosphate group stretching (1300-1150  $\text{cm}^{-1}$ ). (B) The comparative analysis of wt  $\alpha$ S (dark red), mutant A53T (orange), lipid membrane (dark green) and lipid membrane incubated with iron (bright green) shows a different behavior of the proteins in the binding of the metal.

## 9.5 Discussion

Several evidences have suggested that aberrant misfolded protein oligomers formed in the early stage of protein aggregation processes, instead of the mature amyloid fibrils, are the pathogenic species associated with many neurodegenerative disorders, as PD. One of key pathological events which is considered at the basis of the development and the progression of PD, is the binding of oligomers to biological membranes, which modify the organization of the phospholipid bilayer as well as the stability and function of its associated proteins leading to neurotoxicity<sup>219</sup>. The ability of aberrant oligomers to destabilize and disrupts cellular membranes appears to partially depend on the psychochemical properties of oligomers and on the lipid composition of the membrane<sup>220,221</sup>. Increasing interest in elucidating the mechanisms of oligomer formation, structure, molecular dynamincs and cytotoxicity has exponentially grown in the last two decades. Several factors have been shown to promote *in vitro* and *in vivo* protein oligomerization, such as pH, metal ions and interaction with lipid membranes. Among them, the correlation between biological metal ions and the process of protein aggregation represents a fascinating challenge. Several studies have shown that metals can promote misfolded protein aggregation of different amyloid proteins involved in neurodegeneration<sup>312</sup>. A study has demonstrated that the rate of  $\alpha$ S fibrilization *in vitro* is enhanced by the presence of different metals, such as iron, copper, zinc and manganese<sup>226</sup>. Iron is particularly interesting since it has been correlated with increased level of misfolded protein aggregation and oxidative stress<sup>229,234,313</sup>.

In this framework, I studied the effect of  $\text{Fe}^{2+}$  ions on the aggregation of the  $\alpha$ S, the main protein of PD, and specifically on how iron can change the binding affinity of the protein to the membrane. I performed a comparative analysis of the wt  $\alpha$ S form with a mutated species carrying an A53T point-missense mutation leading to early-stage inherited PD. I focused on the production of model membranes with a lipid composition that mimic lipid raft domains. Lipid rafts seem to have a crucial role in the biological function of the protein as well as in the pathology of the disease. Considerable amount of data suggest an involvement of these functional nanodomains in the interaction of misfolded amyloid proteins with cell membranes<sup>122</sup>. In neuronal cells,  $\alpha$ S appears to be involved in the homeostasis of neurotransmitter release at pre-synaptic vesicles by binding lipid rafts and the protein complexes which modulates the assembly and disassembly of membrane vesicles. Moreover, other pathological amyloid proteins such as PrP and  $\text{A}\beta$  peptides have exhibited a strong connections with these lipid domains<sup>111,117</sup>.

First results on *in-vitro* iron mediated aggregation of  $\alpha$ S showed that ferrous ions induce a fast and strong aggregation of both proteins, with greater effect on the mutant A53T  $\alpha$ S. AFM analyses revealed the formation of globular protein aggregates whose dimension and geometry could resemble misfolded protein oligomers. A consistent amount of data have indicated that

oligomers show a broad heterogeneity in terms of morphological and structural features, according to the different conditions in which they are formed<sup>187</sup>. Generally, misfolded protein oligomers display globular morphology with a height in the of range of 3-15 nm which matches with my AFM data. The better propensity of the mutant  $\alpha$ S species to aggregate in presence of the metal is conformed with many studies which highlights this aspect. A study have showed that human neuroblastoma cells overexpressing wt and the mutant A53T  $\alpha$ S exhibit protein aggregates upon treatment with  $\text{FeCl}_2$  (1 or 10 nM), with a greater rate of  $\alpha$ S-aggregation for the A53T<sup>236</sup>. In addition, iron-mediated stimulation appeared to induce 4-fold increase in susceptibility to toxicity compared to cells untreated with iron. IR preliminary analysis revealed that A53T oligomers induced by iron are characterized by a higher content of random-coiled and  $\beta$ -sheet structures than wt  $\alpha$ S, and by an overall structural disorder. I supposed that the amminoacidic replacement of the alanine (A) with a threonine (T) could in somehow affect the structures of the protein by the presence of a steric hindrance or different interactions between the amino acids of the region around the mutation. A similar phenomenon has been show to occurs in collagen molecules. Mutations which cause the substitution of glycine residue within the repeating  $(\text{Gly-Xaa-Yaa})_n$  triplet pattern of the collagen type I triple helix are the major cause of osteogenesis imperfect<sup>314</sup>. These collagen molecules display the formation of less ordered structures with a possible disruption of the fibril structure, a situation that could have some aspects in common with the mutant A53T  $\alpha$ S. Recently, replica exchange molecular dynamic simulations (REMD) have been performed on both full-length monomeric protein wt and A53T  $\alpha$ S in aqueous solution to get insights into the secondary and tertiary structural properties as well as free energy landscapes<sup>315</sup>. The higher propensity of A53T to form protein aggregates appears to be related to the more abundant  $\beta$ -sheet content close to the mutation site in the N-terminal region and the lack of strong intra-molecular long-range interactions in comparison to the wt  $\alpha$ S, leading to the NAC region more solvent exposed. These results seem to confirm our preliminary IR measurements. Moreover, IR spectra also highlighted that mutant A53T  $\alpha$ S is more prone to form complexes with iron. The wt  $\alpha$ S is characterized by a higher vibrational freedom of  $\text{CH}_2$  bonds as in presence of a weaker interaction with the metal compared to the mutant protein. However, for a better understanding about the dynamics and the molecular forces involved in the iron-binding, as well as the consequence on both protein structures, the use of additional techniques such as CD spectroscopy, dynamic simulation and NMR spectroscopy could be very helpful for clarifying this process.

Successively I investigated the ability of iron-induced oligomers to interact with planar artificial lipid bilayer composed by the DOPC, SM and cholesterol and I compared the effect and the lipid-binding of oligomers vs monomers of both proteins. AFM images revealed that monomeric proteins bind lipid membrane in different way. The wt  $\alpha$ S seems to interact with both lipid phases

(L $\alpha$  and S $_o$ ) leading to a change in the morphology of raft-like domains which appear to have irregular and indented borders, as well as a more pronounced roughness. Moreover, the L $\alpha$  phase shows extensive damage site. It is also possible to observe the presence of few aggregates, resembling protein aggregates or protein-lipid complexes, mainly localized on rafts, highlighting that membrane alone can promote a light protein aggregation. Conversely, the mutant A53T seems to interact preferentially with the fluid lipid matrix causing damage sites without affecting the ordered domains. However, the presence of this membrane impairment appears to accelerate the coalescence of the raft-like domains. Preliminary IR data of the monomers incubated with vesicles showed that the mutant A53T is characterized by a high content of  $\beta$ -sheet structure compared to the wt that exhibits  $\alpha$ -helix content. These results disagree with AFM data, a possible explanation being that the protein-vesicles incubation needs more time to promote the effect observed in the planar membrane system, which is supported by a solid substrate and lacks the curvature of lipid vesicles, a parameter that has been shown to highly influence protein binding. There are contradictory results about the mechanisms by which  $\alpha$ S binds lipid membranes and the resulting effects on membrane structure. Several studies performed with vesicles showed that the protein monomer has high affinity for negatively-charged lipid vesicles but display no effect on neutral lipids as PC<sup>206</sup>. My results are in contrast with some of these data because I clearly observed that both proteins interact with the fluid DOPC phase of the membrane.

AFM analysis of iron-induced oligomers interaction with raft-like membranes revealed an accumulation of these misfolded structures on the ordered domains, forming protein clusters, for both wt and mutant A53T  $\alpha$ S. The protein clusters of the mutant species are bigger in terms of dimensions and coverage of the membrane area, reflecting the faster rate of aggregation in the presence of iron compared to the wt  $\alpha$ S. Moreover, IR spectra highlights that wt  $\alpha$ S, aggregating with lower rate in presence of iron, leaves sufficient amount of metal ions in solution that are able to interact with lipid headgroups, resulting in a broadening of phosphate group vibrational peak in a way very similar to the IR spectra of membrane incubated only with iron. Controversial data are present also for the interaction of  $\alpha$ S-oligomers in different kind of model membrane systems. Oligomers have been shown to permeabilized negatively-charge lipid vesicles, but this effect have not been observed for neutral PC lipid vesicles or mixtures of anionic and zwitterionic phospholipids such as POPS/POPC (1:1) and DOPE/DOPS (1:1)<sup>316</sup>. A study have showed that  $\alpha$ S-oligomers are able to stabilized pre-existing defects in planar lipid bilayer made by POPC/POPS by interacting with the lipid acyl chains at the edges of the defect sites<sup>317</sup>. Moreover, cholesterol has been shown to promote the interaction with neutral-charge lipid bilayers<sup>318</sup>. Generally, several mechanisms of membrane damage by oligomers have been proposed, including permeabilization,

lipid extraction and pore-formation both in lipid vesicles and planar model membranes of different compositions<sup>316,319</sup>.

However, my iron-mediated oligomers does not produced any impairment of the membrane. The accumulation on ordered domains has been observed for the A $\beta$ -peptide of Alzheimer's disease on DOPC/DPPC supported lipid bilayer<sup>320</sup>. The peptide aggregates when interacting with the membrane formed small clusters that localized on raft-like domains 90 minutes after peptide addition, showing a similar effect of my  $\alpha$ S-oligomers. I supposed that the accumulation of iron-mediated  $\alpha$ S aberrant oligomers on raft-like domains could have a pathological relevance. The accumulation of iron in PD brain could lead formation of  $\alpha$ S-oligomers which may accumulates on raft-domains of plasma membrane affecting the plethora of biological processes regulated by proteins enriched in these signaling platforms, firstly the homeostasis of neurotransmitter exocytosis. Recent evidences have demonstrated that there is a strong interplay between iron, oxidative stress and protein aggregation in neurodegenerative disease<sup>321,322</sup>. Moreover, oligomer formation induced by metals has been observed even for A $\beta$ -peptide<sup>312</sup>.

Finally, I demonstrated for the first time that iron can promote strong and fast in vitro aggregation of both wt and mutant A53T  $\alpha$ S, leading to the formation of misfolded aberrant oligomers. The mutant form confirmed a better propensity to aggregate due to its mutation which causes modification of secondary structure conformation. At the same time, a preferential accumulation of these oligomers on raft-like domains of planar model membranes have been observed, highlighting a possible role of lipid rafts and iron in the pathology of PD.

## CONCLUSIONS

The discovery of cell membrane submicrometric domains, referred to as lipid rafts, has revolutionized the structural and functional vision of cellular membrane organization in the last two decades, moving the focus on the study of the biophysical properties, biological role and pathological implications of such dynamic nanodomains. From a structural point of view, lipid rafts are enriched in specific lipid species as sphingolipids and cholesterol, and several GPI-anchor proteins. They can be imagined as structurally ordered lipid islands with dynamic composition, floating in a fluid matrix made by other lipids, operating as active signaling platforms involved in protein trafficking and cell-to-cell communication. Moreover, the pathological implication of lipid rafts in cancer and neurodegenerative disease has been proposed. However, the concrete existence of these membrane structures in living systems as well as the biological mechanisms which govern their functions remains elusive. The complexity of *in-vivo* investigation of lipid raft led then to a growing interest in the use and design of artificial membrane models, which mimic the structure and composition of biological membranes.

Here we adopted an AFM-based strategy to investigate the structural features of lipid rafts in model membrane systems, with the great advantage to work at the nanoscale in physiological environment. We tested two fabrication methods for the production of planar supported lipid bilayer (SLBs) of specific lipid composition: drop-casting and direct vesicle fusion, one of the most common techniques used in membrane technology. We highlighted the value of drop-casting for the fabrication of basic synthetic lipid membranes to study the interaction with artificial structures that mimic the extracellular environment, as carbon nanotubes. However, for the study of lipid nanodomains we found that the direct vesicle fusion method displays clear advantages, one for all the much higher reproducibility of complex SLBs. We produced three-component membranes with different relative lipid composition and studied the formation and evolution of lipid-raft domains by AFM. We used our most robust and stable model membrane system (DOPC/SM 66:33 + 5% Cholesterol) as a reference to further study rafts interaction with molecules of high biological/clinical relevance. For the first time, we evaluated the interaction of a full-length Prion protein carrying a membrane anchor at the C-terminal (FL-PrP<sup>C</sup>-MA) with the SLB confirming the targeting of raft domains by the protein and highlighting a possible role of lipid-anchors in the pathological aggregation of PrP<sup>C</sup>. Then we used our membrane model to investigate the role of iron (II) in the interaction between alpha synuclein ( $\alpha$ S) and the raft-like membrane, demonstrating a strong impact of the metal ions in promoting the oligomeric aggregation of the protein and its accumulation in the rafts. We compared the human wild-type  $\alpha$ S with a mutant  $\alpha$ S species (A53T) that causes an inherited early-stage Parkinson's disease (PD),

showing a stronger effect of iron (II) ions on the second case. Moreover, by infrared spectroscopy we highlighted some structural differences between the aggregates of the two proteins and their interaction with lipid rafts, which could be ultimately useful to gain new insights for the treatment of this neurodegenerative disorder. Our results pointed out that cellular iron pool could be an interesting therapeutic target against the disease

## FUTURE PERSPECTIVES

In this Ph.D. thesis we mastered model membrane technology applied to the study of lipid raft domains and their evolution in interaction with membrane proteins. In particular, we focused on lipidated-Prion protein and on the role of divalent iron ions in promoting pathological, structural and functional changes of the main protein related to Parkinson's disease, alpha synuclein ( $\alpha$ S). Two manuscripts on these topics are being finalized at present, and will be soon submitted for publication. Remaining on the short term aims, a session of fast-scanning, high-resolution AFM (Cypher, Oxford Instrument) has been scheduled in two weeks from now, in order to get more complete information on the kinetics of iron-mediated interaction of  $\alpha$ S with lipid rafts, and more hints on the structural nature of the oligomers formed. Also, we plan to study the role of other biologically relevant metal ion solutions, with different ionic strength and/or ion size, as copper or trivalent iron ions, on  $\alpha$ S-model membrane interaction. On the longer term, we plan to face the complexity of real life in steps, moving on from model membrane systems to test our iron-induced oligomers *in vitro* on cellular membranes, where multiple membrane targets, including the ones postulated for  $\alpha$ S in mitochondria, can play a relevant role. By means of a multi-technique, multi-scale approach we will investigate for instance the effects induced by oligomers to cells in terms of cytotoxicity, membrane localization and aggregation and potentially lipid damage by a combination of AFM and fluorescent microscopy measurements, and will also correlate these information with the mechanical stress, measured by means of AFM force-distance curves. Ultimately, the molecular characterization of oligomers in interaction with cells should be correlated with electrophysiology measurements to address their role in cell-cell communication.

## MATERIALS AND METHODS

### Chemicals

18:1 ( $\Delta^9$ -Cis) PC (1,2-dioleoyl-sn-glycero-3-phosphocholine, DOPC), sphingomyelin (brain, porcine, SM) and cholesterol (ovine wool, > 98%) were purchased by Avanti polar lipids (Alabaster, USA). Chloroform, decane, isopropanol (2-propanol, IPA) and methanol were all provided by Fluka and Sigma Aldrich, (Milan, Italy). FeCl<sub>2</sub> solution was prepared by dissolving salt powder (Sigma Aldrich) in ultrapure 18.2 M $\Omega$ -cm water (Milli-Q, Millipore SpA, Milan, Italy), heated at 50 °C in order to promote iron solubilization, and subsequently filtered with a sterile syringe-filter (0.22  $\mu$ m) prior to use.

### Supported lipid bilayer preparation by drop-casting

Briefly, DOPC, SM and cholesterol powders were dissolved in chloroform, chloroform/decane 1:1 (v/v), chloroform/methanol 1:1 (v/v) or IPA at the final concentration of 1 mg/mL. Lipid solutions were mixed together producing mixtures of different lipid compositions at various molar concentrations (DOPC/SM 50:50, DOPC/SM/Chol 40:40:20, DOPC/Chol 2:1). 200  $\mu$ L of lipid mixture were spread onto O<sub>2</sub>-plasma cleaned glass coverslips of 22 mm<sup>2</sup> in dimension used as substrate (Hampton Research, CA, USA). Solvent evaporation to promote self-assembly of lipid bilayers was carried on in incubator at 30 °C and 80% humidity.

### AFM imaging

All AFM images were acquired using a commercially available microscope (MFP-3D Stand Alone AFM from Asylum Research, Santa Barbara, CA). Measurements were carried out at room temperature working in dynamic tapping mode. For imaging, commercially available silicon cantilevers (NSC19, Mikro-Masch, Poland, nominal spring constant 0.6 nN/nm and OMCL-RC800PSA-1, Olympus Micro Cantilevers, nominal spring constant 0.76 nN/nm,) have been chosen for imaging in air and liquid respectively. In both cases cantilevers were used working at low oscillation amplitudes with half free amplitude set-point. High resolution images (512 x 512 pixels frames) were acquired at 0.6 $\pm$ 1 lines/s scan speed.

For the investigation of lipidated-PrP<sup>C</sup> (full length Prion protein carrying a C-terminal membrane anchor, FL- PrP<sup>C</sup>-MA) interaction with lipid raft model membranes, 25 nM of the protein were incubated on planar lipid bilayer for 30 min and then AFM imaging were performed.

For studying  $\alpha$ S interaction with raft-like membranes, 100  $\mu$ g of iron-induced oligomers and protein monomers of human *wild-type*  $\alpha$ S and A53T mutant  $\alpha$ S (35  $\mu$ M) were incubated to supported lipid bilayer for 1 h at room temperature (final protein concentration 4.5  $\mu$ M) and imaged by AFM.

### **AFM data analysis**

AFM images were analyzed using Gwyddion, open-source modular program for scanning probe microscopy (SPM) data visualization and analysis<sup>323</sup>. Results of the AFM topography analysis were expressed as mean  $\pm$  standard deviation (SD) obtained from measurements performed on at least three independent membranes ( $n \geq 3$ ). Surface roughness was determined as Ra value of the height irregularities. Height distributions were fitted using a double Gaussian function using Igor Pro software (Wavemetrics, US). For the analysis of the size distribution  $\alpha$ S aggregates (see paragraph 9.1) the grain analysis macro of Gwyddion software was used. To select the protein aggregates the software uses a threshold in Z and masks in this way all the particles below or above the selected threshold. The threshold chosen for all the images has been chosen manually image by image. The subsequent analysis of the height distribution is therefore limited by this threshold values.

### **MWCNTs preparation**

MWCNTs characterized by 20÷30 nm in diameter (Nanostructured & Amorphous Materials, Inc.) were used as received and substrates were prepared as described previously<sup>279,280</sup>. Briefly, MWCNTs were functionalized using 1,3-dipolar cycloaddition with heptanal and sarcosine at 130 °C for 120 h in dimethylformamide (DMF) as solvent. The DMF solution of functionalized MWCNTs (0.01 mg/mL) was spread to uniformly layer the entire glass coverslip and let to evaporate at 80 °C. Then the substrates were heated up at 350 °C under nitrogen atmosphere to induce the complete re-pristinization of MWCNTs.

### **Artificial membranes on MWCNTs**

Artificial membranes were prepared by drop-casting method as previously described in this chapter. Briefly, DOPC and cholesterol powders were dissolved in chloroform at 2:1 molar ratio at a final concentration of 100  $\mu$ M. 100  $\mu$ L of lipid solution were deposited on a glass coverslip, used as control, and on MWCNTs substrates supported by the same glass coverslip. Solvent

evaporation was performed at 30 ° C, 80% humidity. Membrane was rinsed in Milli-Q H<sub>2</sub>O, dried gently with a nitrogen flux and mounted on metallic plates using epoxy glue for subsequent AFM imaging.

### **Raman spectroscopy**

The Raman spectroscopy measurements were performed in the reflection geometry. A 532-nm continuous-wave laser (Cobolt Samba, 50 mW, bandwidth 1 MHz) was used as excitation source. The beam was focused on the sample by a 100× air objective (NA 0.8, EC EpiPlan, Zeiss) resulting in a diameter of laser spot of about 0.5 μm. A 532-nm RazorEdge Dichroic™ laser-flat beam-splitter and a 532-nm RazorEdge® ultra-steep long-pass edge filter was used to direct the light into microscope and cut Rayleigh scattered light, respectively. The laser power on the sample was controlled by the neutral density filter (Thorlabs) and kept at 100 μW. The acquisition time in all experiments was 60 s. All Raman measurements and analysis were performed by CNR-IOM (TASC Laboratory, Basovizza, Trieste, Italy).

### **Lipid vesicles preparation and supported lipid bilayer formation**

For the production of supported lipid bilayer by vesicle fusion I have followed the procedure described by Oropesa-Nuñez and colleagues<sup>324</sup>, with some modifications. Briefly, DOPC, SM, cholesterol and GM1 powders were dissolved in chloroform at the final concentration of 1 mg/mL. Lipid solutions were mixed at various molar ratio according to the desire composition, and gently evaporated under nitrogen flux. Samples were placed under vacuum overnight in order to completely removed solvent residues and resuspended in Milli-Q H<sub>2</sub>O at a lipid concentration of 1 mg/mL to form multilamellar vesicles (MLVs). MLVs were left to swell for 1 h at 60 °C and then extruded 51 times through a polycarbonate membrane with 100 nm pores using a commercial extruder (Avanti Polar Lipids) at the same temperature, to form large unilamellar vesicles (LUVs). After cooling at room temperature, LUVs were diluted 10 fold with Milli-Q H<sub>2</sub>O. Then, 90 μL of each suspension and 10 μL of a 50 mM CaCl<sub>2</sub> solution were deposited onto a 1 cm<sup>2</sup> of freshly cleaved mica substrate attached to AFM liquid chamber by ultrafast glue. In order to get uniform bilayer coverage, the samples were stored 15 min at room temperature and then AFM chamber was completely filled with Milli-Q H<sub>2</sub>O. After 1 h, membrane was gently rinsed three times with Milli-Q H<sub>2</sub>O to remove excess vesicles from the liquid sub-phase before AFM measurements.

## **Prion protein purification and membrane-anchor ligation**

Membrane-anchored Full-length Prion protein (residues 23-231, FL-PrP<sup>C</sup>-MA) were produced by the group of Prof. C. F. W. Becker (University of Wien). PrP<sup>C</sup> were expressed and purified according to the protocol described by Olschewski and colleagues<sup>304</sup>. The procedure for the production of FL-PrP<sup>C</sup>-MA is described in the study performed by Chu et colleagues<sup>301</sup>.

## **$\alpha$ S expression and purification**

Expression and purification of  $\alpha$ S was performed by the group of Prof. Giuseppe Legname (SISSA, Trieste, Italy). Briefly, the overexpression of  $\alpha$ S was obtained by growing bacterial *E.Coli* cells in 100  $\mu$ g/mL ampicillin containing Luria-Bertani broth at 37 °C until an OD(600) of about 0.6 followed by induction with 0.6 mM isopropyl  $\beta$ -thiogalactopyranoside for 5 h. The purification was performed according to the method of Huang et collagues<sup>325</sup>, with some additional modifications. Briefly, the cell pellet from 1 L culture was resuspended in 100 mL osmotic shock buffer (30 mM Tris-HCl, 40% sucrose, 2 mM ethylenediaminetetraacetic acid disodium (EDTA), pH 7.2) and incubated for 10 min at room temperature. The pellet collected by centrifugation (9000 rpm, 20 min, 4 °C) was resuspended quickly in 90 mL cold water followed by the addition 37.5  $\mu$ L of saturated MgCl<sub>2</sub> and incubated on ice for 3 min. The supernatant containing periplasm proteins was collected by centrifugation (as before) and brought to 20 mM Tris pH 8 (adding 2 mL 1M Tris pH 8, 8 mL cold water for 100 mL solution). The solution was boiled for 10 min and centrifuged (as before). The supernatant was collected, incubated on ice and proteins were precipitated by addition of 35% of ammonium sulfate (19.4 g of ammonium sulfate for 100 mL of solution) (1st precipitation step). The solution was centrifuged and followed by the addition of 55% of ammonium sulfate (11.8 g for 100 mL of solution) (2nd precipitation step). The pellet containing  $\alpha$ -synuclein was collected by centrifugation and dialyzed overnight against 20 mM Tris pH 8 buffer. Each purification step was analyzed by SDS-PAGE. After centrifugation at 9000 rpm for 20 min, the protein was filtered with a 0.22  $\mu$ m syringe filter (Millipore) and loaded onto a Q-Sepharose Fast Flow column (GE Healthcare) and eluted with 0÷500 mM NaCl gradient in 60 min. Protein purification was performed using AKTA Purifier chromatography system (GE Healthcare). The elution fractions were analyzed by SDS-PAGE. Fractions containing only 15 kDa band corresponding to  $\alpha$ S protein were collected for overnight dialysis against water. Finally, the protein was quantified using absorbance at 280 nm, aliquoted, lyophilized and stored at -80°C.

## **In vitro aggregation of $\alpha$ S and AFM protein characterization**

In order to study iron-mediated aggregation of human *wild-type*  $\alpha$ S and the mutant A53T  $\alpha$ S, 100  $\mu$ g of each  $\alpha$ S protein (35  $\mu$ M) were mixed with 2 mM FeCl<sub>2</sub> or Milli-Q H<sub>2</sub>O for the control. Protein solutions were incubated at 37 °C under shaking for 1 hour. 10  $\mu$ L of protein solution were spread onto 1 cm x 1 cm piece of freshly cleaved mica, left to incubate for 5 min, gently rinsed 3 times with Milli-Q H<sub>2</sub>O, dried with a stream of nitrogen, and successively analyzed by AFM in air at room temperature.

## **FTIR-ATR spectroscopy measurements**

For the first experiment, 10  $\mu$ g of iron-induced oligomers of human *wild-type*  $\alpha$ S and the mutant A53T species (prepared as previously reported) were diluted in 200  $\mu$ L of Milli-Q H<sub>2</sub>O. For the second experiment 60  $\mu$ g of large unilamellar vesicles (LUVs) composed by DOPC/SM (66:33) + 5% cholesterol were mixed with 10  $\mu$ g of iron-induced oligomers of both proteins, and incubated for 1 h at room temperature. Same procedure at the same experimental conditions was repeated for both protein monomers. For the control, 60  $\mu$ g of LUVs were incubated in Milli-Q H<sub>2</sub>O or 0.2 mM FeCl<sub>2</sub> salt solution for 1 h at room temperature.

For each experiment, 200  $\mu$ L of sample solution were spread over the whole area of a trapezoidal germanium ATR plate and left to dry forming a thin film of the sample. The crystal is 50mm×10mm×2mm wide with an incidence angle of 45° yielding 25 internal reflections. 30 repeated spectra were acquired for monitoring the complete drying of the sample. Every spectrum was collected at 2 cm<sup>-1</sup>, repeating 256 scans in the range 4500÷400 cm<sup>-1</sup>.

A water jacket connected to a circulating thermalized bath was placed in contact with the aluminium plate holding the IRE crystal in order to perform the heating up and cooling down cycles. A cycle of thermal analysis was performed by an ascending ramp from 20 to 90 °C degrees and a descending one from 90 °C to 20 °C degree, collecting a spectrum every 5 degrees. Additionally, the temperature was controlled by a thermocouple placed on the IRE. The experiment was carried out in duplicate at room temperature. Considering that germanium crystal changes its refraction index depending on the temperature, it was necessary to perform a thermal cycle of the clean germanium crystal with the same conditions described for the sample in order to correctly subtract the background from the spectra at temperature of working (room temperature). Measurements were performed at SISSI (Synchrotron Infrared Source for Spectroscopy and Imaging, Elettra-Sincrotrone Beamlines, Basovizza, Trieste, Italy)

## **ATR-IR data collection and analysis**

For all experiments, the measurements were acquired by a Bruker Vertex 70 equipped with RT-DLaTGS detector. The data-sets collected was previously treated by means of Bruker software OPUS 7.5. All the sample spectra were baseline-corrected subtracting the spectra collected at the relative temperature of the clean germanium crystal used for every experiment.

## APPENDIX

### A. AFM analysis of extracellular vesicles<sup>f</sup>

Extracellular vesicles (EVs) are small phospholipid vesicles (< 1  $\mu\text{m}$ ) naturally released by cells in the surrounding environment, ensuring the transport of molecules such as proteins and genetic materials. EVs mediate communication between cells and have been proposed as biomarkers for a variety of diseases. The most promising two classes of EVs are exosomes (EXOs) and microvesicles (MVs). EXOs are characterized by dimensions in the range of 30-150 nm and originate from the endosomal system of cells. MVs are bigger in dimensions (100-1000 nm) and are produced from the budding of cell plasma membrane. EXOs are considered the most interesting EVs for their potential application in nanomedicine as therapeutic agents in regenerative medicine, drug-delivery and immune therapy, especially in cancer<sup>326</sup>. Several studies have shown that, in tumor models, cancer cells release EXOs promoting immune suppression and metastasis<sup>327</sup>. Moreover it has been demonstrated that EXOs carry specific markers for most types of cancerous tumors and could hence be used as an early diagnostic tool<sup>328-331</sup>. However, due to the heterogeneity and complexity of their origin and composition, the mechanisms by which these EVs carry out their functions is still unknown. Moreover, their quantification as well as their biophysical and biochemical properties remains a challenge as a result of the absence of methodological standards for their characterization.

In this framework, we addressed the advantages of AFM for the morphological characterization of EXOs, focusing on different EXO-immobilization strategy for AFM bio-imaging, with the aim to measure EXO-size distribution. At the same time, we proposed physical explanations for the artifacts both deriving from sample preparation procedures and intrinsic to the measurements, showing how to obtain reliable vesicle size distributions with AFM. In Fig. 63 the schematic representation of the typical experimental workflow is reported. EXOs can be obtained by biosamples and/or cell cultures. These vesicles are extracted and isolated from the extracellular medium or directly from the biofluid of interest. Most common methods for EXO isolation are size exclusion chromatography, ultracentrifuge, particle precipitation, cross flow and diafiltration<sup>332-336</sup>. After the isolation, EXOs are deposited on the substrate such as mica or glass and analyzed by AFM.

---

<sup>f</sup> P. Parisse, I. Rago, L. Ulloa Severino, F. Perissinotto, E. Ambrosetti, P. Paoletti, M. Ricci, A. P. Beltrami, D. Cesselli, L. Casalis. "Atomic force microscopy analysis of extracellular vesicles". *Eur Biophys J.* 2017. 46(8):813-820.

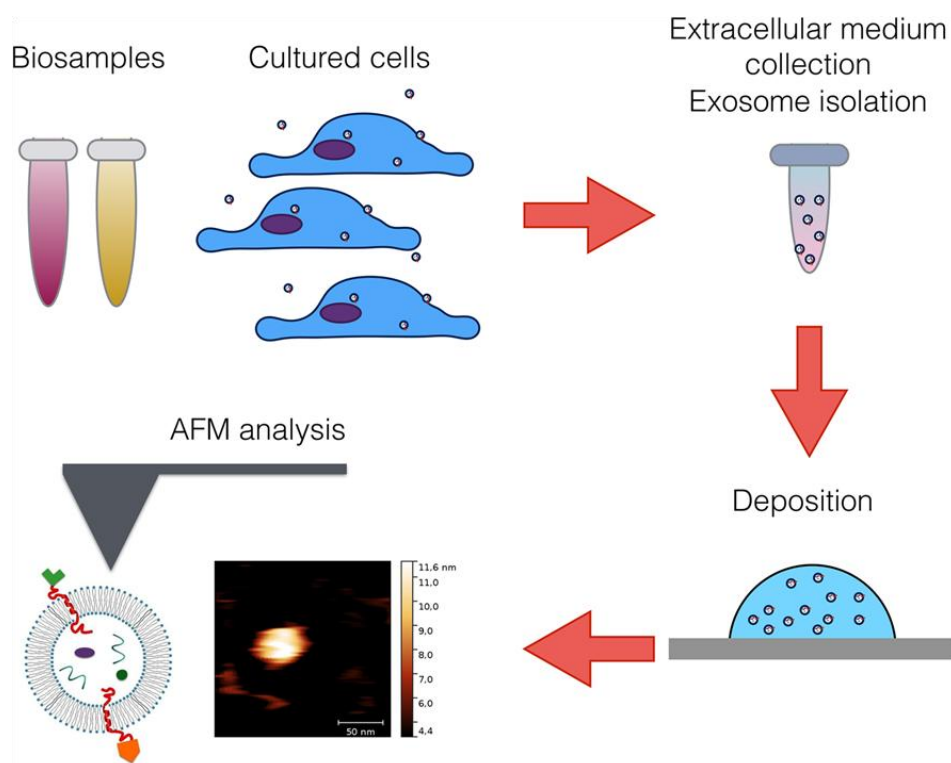


**Figure 63. Schematic experimental workflow for EXOs purification and AFM characterization.** From Parisse et al, 2017

337

We focused on the EXO-immobilization step on the surface prior AFM imaging. Surfaces for bio-imaging has preferentially to be very flat (roughness < 0.5 nm) and with some residual charges to enhance the vesicle attachment. Among the available substrates, muscovite (mica) represents a very good material because after the cleavage it is atomically flat and negatively charged allowing EXOs to remain attached to the surface also after washing treatment with pure water or buffer and drying with nitrogen flux for AFM imaging in air. Increasing the incubation time of EXOs on mica makes possible to perform even AFM imaging in liquid solution<sup>338–340</sup>.

Typically, AFM analysis performed in air in amplitude modulation mode results in EXO-height distribution in range from 1-2 nm to 15-20 nm and lateral width of 30-200 nm<sup>341–345</sup>. We performed AFM imaging in air of SKBR3-derived EXOs deposited on mica. Topography analysis of EXOs (Fig. 64a) shows that these vesicles have a donut-shape, being present a central collapsed region that appears almost as dark as the mica surface around it. This effect is mainly imputed to the mechanical perturbation produced by the AFM tip and this effect is more pronounced when increasing the applied force during the AFM measurements. In order to preserve the shape of EXOs while imaging them in air, fixation with glutaraldehyde and paraformaldehyde (PFA) has been reported for the analysis of EVs<sup>346,347</sup>. In Fig. 64 b, we reported AFM image taken in our group of SKBR3-derived EXOs fixed with 4% PFA and analyzed in the same previous conditions. After the fixation the vesicles appear more spherical with the respect to the non-fixed ones.

When vesicles are measured in liquid environment, the spherical shape is maintained and height values in the range of 10-100 nm are measured. In Fig. 64 c, AFM imaging of SKBR3-derived EXOs, spotted on plasma-cleaned glass and measured in PBS is reported.

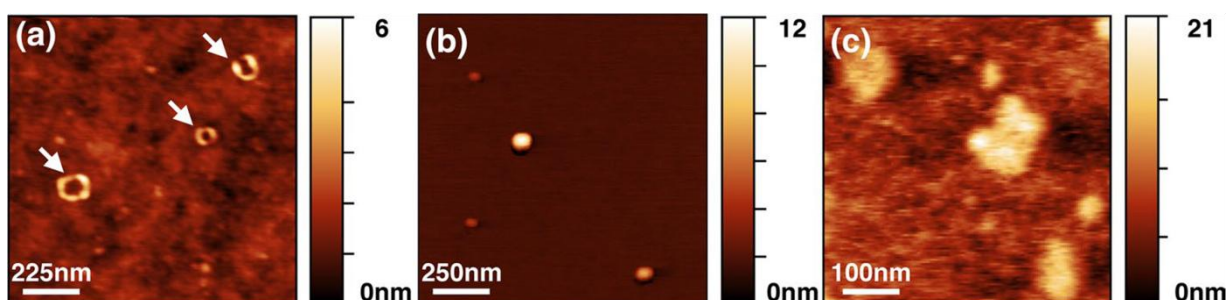


**Fig 64. AFM topographic images of SKBR3-derived EXOs obtained following different preparation methods. (a)** EXOs spotted on mica, dried with nitrogen flux and imaged in air. **(b)** EXOs spotted on mica, fixed with 4% PFA dried with nitrogen flux and imaged in air. **(c)** EXOs spotted on plasma-cleaned glass and imaged in PBS.

The specific drying procedure is a critical step because can create artifacts giving AFM topographic values in air which differ from those obtained during the analysis in liquid buffer. Generally, a gentle drying by a stream nitrogen or leave solution to naturally evaporate on substrate has been demonstrated to better preserve the shape of the vesicles<sup>348,349</sup>. The effect of tip convolution should be taken into account for the assessment of the lateral vesicle size in both air and liquid AFM imaging. This effect is reflected in a broadening of the surface features and it is particularly important during the analysis of size distribution of tumor-derived or healthy vesicles which can be different as already observed<sup>350</sup>. In addition to the size variability, tumor and healthy vesicles even diverge for the mechanical properties (stiffness and adhesion)<sup>338</sup>.

In conclusion we presented here an overview of AFM-based characterization of EVs, reviewing difference conditions of immobilization and imaging of the vesicles. We evidenced the important of operating in liquid buffer to better preserve the physical properties of the vesicles and to obtain significant size distributions. In this context, AFM represents an optimal choice for the collection of the biophysical properties (size distribution, morphology, mechanical properties, biomolecular load) of exosomes derived from specific subpopulations of cells.

## Materials and Methods

AFM imaging in air in amplitude modulation mode were performed on NT-MDT Solver Pro, spring constant 2 N/m, resonance frequency  $\approx 70$  kHz, amplitude  $\approx 50$  nm. AFM imaging in liquid buffer in amplitude modulation mode were performed on MFP-3D Asylum Research, spring constant 0.1 N/m, resonance frequency  $\approx 32$  kHz, amplitude  $\approx 30$  nm.

## **B. AFM analysis of the intimate interaction of interfaced-nanostructured CNTs substrates with the cell membrane**

Extracellular matrix exerts a key role in driving and promoting cellular phenotype destiny by chemical and/or morphological contributions. An example of the role of ECM in modulating cellular phenotype is the calcific aortic valve disease (CAVD) which is strongly correlated to variations in ECM morphological and mechanical properties.

In this framework, in collaboration with my colleagues, Luisa Ulloa Severino and Ilaria Rago, we started investigating such aspect interfacing porcine aortic valve interstitial cells (pVICs) to nanostructured substrates that mimic morphologically the ECM. We took advantages of innovative nano-materials as multi-walled carbon-nanotubes (MWCNTs) carpets directly grown on supporting slides allowing for the first time to perform simultaneously both AFM imaging and fluorescence microscopy assay. These new materials were produced developing a novel strategy based on the chemical vapor deposition (CVD). CNTs have been shown to be very promising nanostructured materials for the development of bioelectronics components for novel neural interfaces. A role of CNTs in the improving of axon growth have been proposed when used to interface neuronal cells. Moreover it has been shown to enhance the synaptic connections between neurons. More precisely, the extracellular environment, when artificially reconstructed by MWCNTs, induced synaptogenesis in cultured hippocampal neurons during early network formation. Enhancing cell-to-cell communication, the idea of direct and intimate contribution of CNTs in regulating cell membrane processes and properties by mimicking the ECM has been grown in the last years. Previous work by the group of Prof. Laura Ballerini (SISSA, Trieste, Italy) and co-workers had already hypothesized that a pinching phenomenon took place between plasma membrane and CNTs decorated substrates when neurons are cultured above them<sup>351</sup>. In this contest, my experimental work aimed in the visualization of the inner side of pVICs grown on flat glass controls or on nanostructured MWCNTs substrates. Cell membranes on both substrates were obtained via osmotic shock protocol and analyzed by AFM in liquid in order to image the cytosolic side of the membrane. In Fig. 64 preliminary results of AFM images on patches attached on both substrates are reported. From height profiles (Fig. 65 B-D) it is possible to see that the basal membrane patches placed on glass (Fig. 65 A) appear, as easily predictable, totally flat without any appreciable protrusion through it while the basal membrane adhering to the CNTs (Fig. 65 C) follows the nanostructured substrate morphology.

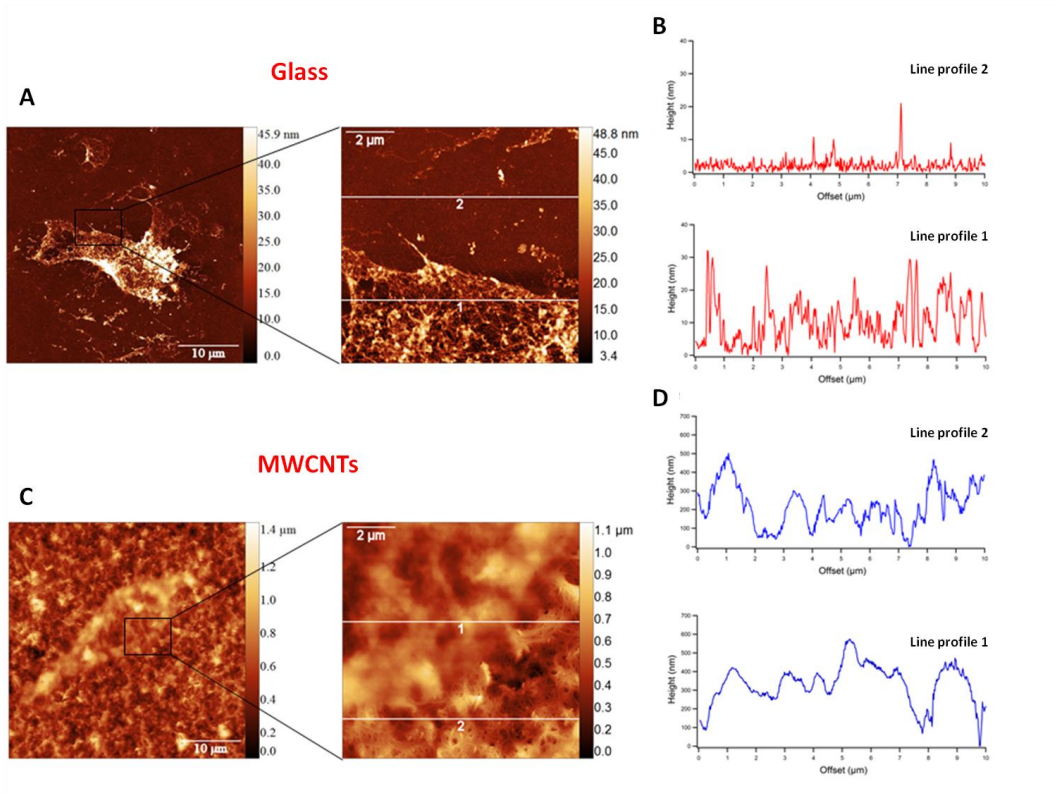


**Figure 65. Characterization of interaction between basal membrane and CNTs of VICs.** AFM images of VICs basal membrane (A) on glass and (C) on CNTs with their respective line profile (B-D).

In order to highlight possible membrane piercing by the substrate we prepared the same samples for electron microscopy investigation. Scanning electron microscopy (SEM) images of pVICs basal membrane patches stuck on both substrates are reported in Fig. 66. In the enlarged image of Fig. 66 B, right, it is clearly visible how a CNT below the plasma membrane cross it completely (red arrow).

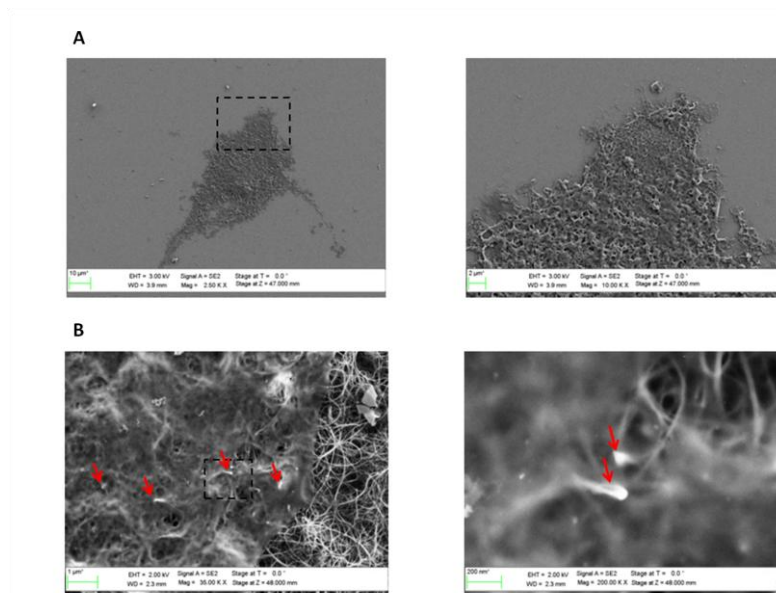


**Figure 66. SEM images of VICs basal membrane grown (a) on the glass and (b) on CNTs.**

## **Materials and Methods**

### **pVICs Squirting assay**

Cells were plated on both substrates (glass and MWCNTs carpets) at a confluence of  $5.0 \times 10^5$  cells. Before seeding, all the substrates were washed with ethanol and plasma cleaned. After 72 hours, the cells were subjected to osmotic shock to obtain the basal cell membrane using a protocol described previously by Ziegler et colleagues (REF). Briefly, the cells were washed with ice cold 20 mM PIPES, 150 mM KCl, pH 6.2, incubated in hypotonic buffer (4 mM PIPES, 30 mM KCl, pH 6.2) for 3 min on ice and subsequently squirted using 5 mL of the same buffer through a 25-gauge needle. Incubation in high salt was done in 2 M NaCl, 2.7 mM KCl, 1.5 mM KH<sub>2</sub>PO<sub>4</sub>, 1 mM Na<sub>2</sub>HPO<sub>4</sub>, pH 7.2 for 30 min at room temperature in order to removed cytoskeleton. The samples were then fixed in 4% PFA and washed 3 times in PBS.

### **AFM analysis**

AFM imaging was performed to visualized and characterize the thickness and morphology of pVICs basal cell membranes. The AFM images were acquired using a commercially available microscopy, NT-MDT Smena (NT-MDT, Russia) mounted on Inverted Research Microscope Eclipse Ti, Nikon (Nikon Corporation). All AFM measurements were carried out at room temperature working in tapping mode in air using commercial cantilevers (HQ:NSC36/C from MikroMasch Co. - Tallinn – Estonia, resonance frequency 65 kHz, force constant 0.6 nN/nm). 512 × 512 pixels images were acquired at 0.3 lines/second scan speed. Gwyddion software ([www.gwyddion.net](http://www.gwyddion.net)) was used to analyze AFM images.

### **Scanning electron microscopy (SEM) imaging**

Before Field Emission Scanning Electron Microscopy (FE-SEM), a lightweight gold evaporation at control (Glass) was performed, while no pretreatment was carried out to CNTs because they were already conductive. FE-SEM imaging was performed on the as-produced CNTs using a Gemini SUPRA 40 SEM (Carl Zeiss NTS GmbH, Oberkochen, Germany) operating at an accelerating voltage of 3 keV.

## BIBLIOGRAPHY

1. Cooper, G. M. Structure of the Plasma Membrane. (2000).
2. Singer, S. J. & Nicolson, G. L. The fluid mosaic model of the structure of cell membranes. *Science* **175**, 720–31 (1972).
3. van Meer, G. & Simons, K. Lipid polarity and sorting in epithelial cells. *J. Cell. Biochem.* **36**, 51–58 (1988).
4. Simons, K. & Ikonen, E. Functional rafts in cell membranes. *Nature* **387**, 569–572 (1997).
5. Centre de recherches agronomiques, G. & Faculté universitaire des sciences agronomiques de Gembloux., M. *Biotechnologie, agronomie, société et environnement = Biotechnology, agronomy, society and environment : BASE*. <http://popups.ulg.ac.be/1780-4507> (Bibliothèque de la Faculté, 1997).
6. Vance, D. E. & Vance, J. E. *Biochemistry of lipids, lipoproteins, and membranes*. (Elsevier, 2002).
7. Frolov, V. A., Shnyrova, A. V. & Zimmerberg, J. Lipid Polymorphisms and Membrane Shape. *Cold Spring Harb. Perspect. Biol.* **3**, a004747–a004747 (2011).
8. Einar K. Fridriksson, ‡ et al. Quantitative Analysis of Phospholipids in Functionally Important Membrane Domains from RBL-2H3 Mast Cells Using Tandem High-Resolution Mass Spectrometry†. (1999). doi:10.1021/BI9828324
9. Wenk, M. R. The emerging field of lipidomics. *Nat. Rev. Drug Discov.* **4**, 594–610 (2005).
10. Fahy, E. et al. A comprehensive classification system for lipids. *J. Lipid Res.* **46**, 839–862 (2005).
11. van Meer, G., Voelker, D. R. & Feigenson, G. W. Membrane lipids: where they are and how they behave. *Nat. Rev. Mol. Cell Biol.* **9**, 112–124 (2008).
12. Marsh, D. Lateral Pressure Profile, Spontaneous Curvature Frustration, and the Incorporation and Conformation of Proteins in Membranes. *Biophys. J.* **93**, 3884–3899 (2007).
13. Athenstaedt, K. & Daum, G. Phosphatidic acid , a key intermediate in lipid metabolism. *Eur. J. Biochem.* **266**, 1–16 (1999).
14. Rodriguez-Berdini, L. & Ferrero, G. A Technique for the Measurement of in vitro Phospholipid Synthesis via Radioactive Labeling. *BIO-PROTOCOL* **6**, (2016).
15. Kolesnick, R. Signal transduction through the sphingomyelin pathway. *Mol. Chem. Neuropathol.* **21**, 287–297 (1994).
16. Simons, K. & Toomre, D. Lipid rafts and signal transduction. *Nat. Rev. Mol. Cell Biol.* **1**, 31–39 (2000).
17. Prayson, R. A. *Neuropathology*. (Elsevier/Saunders, 2012).
18. Nelson, D. L. (David L., Cox, M. M. & Lehninger, A. L. *Lehninger principles of biochemistry*. (W.H. Freeman and Company, 2013).
19. McConnell, H. M. & Radhakrishnan, A. Condensed complexes of cholesterol and phospholipids. *Biochim. Biophys. Acta* **1610**, 159–73 (2003).
20. Maxfield, F. R. & Tabas, I. Role of cholesterol and lipid organization in disease. *Nature* **438**, 612–621 (2005).
21. Alberts, B. et al. *Molecular biology of the cell*. (Garland Science, 2002).
22. Simons, K. & Sampaio, J. L. Membrane organization and lipid rafts. *Cold Spring Harb. Perspect. Biol.* **3**, a004697 (2011).
23. Nagle, J. F. Theory of the Main Lipid Bilayer Phase Transition. *Annu. Rev. Phys. Chem.* **31**, 157–196 (1980).
24. Nagle, J. F. Theory of lipid monolayer and bilayer phase transitions: Effect of headgroup interactions. *J. Membr. Biol.* **27**, 233–250 (1976).
25. Marsh, D. Analysis of the chainlength dependence of lipid phase transition temperatures: Main and pretransitions of phosphatidylcholines; main and non-lamellar transitions of phosphatidylethanolamines. *Biochim. Biophys. Acta - Biomembr.* **1062**, 1–6 (1991).

26. Ipsen, J. H., Karlström, G., Mouritsen, O. G., Wennerström, H. & Zuckermann, M. J. Phase equilibria in the phosphatidylcholine-cholesterol system. *Biochim. Biophys. Acta* **905**, 162–72 (1987).
27. Davis, J. H., Clair, J. J. & Juhasz, J. Phase Equilibria in DOPC/DPPC-d62/Cholesterol Mixtures. *Biophys. J.* **96**, 521–539 (2009).
28. Vist, M. R. & Davis, J. H. Phase equilibria of cholesterol/dipalmitoylphosphatidylcholine mixtures: deuterium nuclear magnetic resonance and differential scanning calorimetry. *Biochemistry* **29**, 451–464 (1990).
29. Lönnfors, M., Doux, J. P. F., Killian, J. A., Nyholm, T. K. M. & Slotte, J. P. Sterols have higher affinity for sphingomyelin than for phosphatidylcholine bilayers even at equal acyl-chain order. *Biophys. J.* **100**, 2633–41 (2011).
30. Veatch, S. L. & Keller, S. L. Miscibility Phase Diagrams of Giant Vesicles Containing Sphingomyelin. *Phys. Rev. Lett.* **94**, 148101 (2005).
31. Wood, W. G., Igbavboa, U., Müller, W. E. & Eckert, G. P. Cholesterol asymmetry in synaptic plasma membranes. *J. Neurochem.* **116**, 684–9 (2011).
32. Ikeda, M., Kihara, A. & Igarashi, Y. Lipid asymmetry of the eukaryotic plasma membrane: functions and related enzymes. *Biol. Pharm. Bull.* **29**, 1542–6 (2006).
33. Schroeder, F. *et al.* Transmembrane distribution of sterol in the human erythrocyte. *Biochim. Biophys. Acta* **1066**, 183–92 (1991).
34. Devaux, P. F., López-Montero, I. & Bryde, S. Proteins involved in lipid translocation in eukaryotic cells. *Chem. Phys. Lipids* **141**, 119–32 (2006).
35. Manno, S., Takakuwa, Y. & Mohandas, N. Identification of a functional role for lipid asymmetry in biological membranes: Phosphatidylserine-skeletal protein interactions modulate membrane stability. *Proc. Natl. Acad. Sci. U. S. A.* **99**, 1943–8 (2002).
36. Fadok, V. A. *et al.* Apoptosis: getting rid of the bodies. *Curr. Biol.* **8**, R693-5 (1998).
37. Emoto, K. & Umeda, M. An essential role for a membrane lipid in cytokinesis. Regulation of contractile ring disassembly by redistribution of phosphatidylethanolamine. *J. Cell Biol.* **149**, 1215–24 (2000).
38. Fujimoto, T. & Parmryd, I. Interleaflet Coupling, Pinning, and Leaflet Asymmetry-Major Players in Plasma Membrane Nanodomain Formation. *Front. cell Dev. Biol.* **4**, 155 (2016).
39. Day, C. A., Kraft, L. J., Kang, M. & Kenworthy, A. K. Analysis of protein and lipid dynamics using confocal fluorescence recovery after photobleaching (FRAP). *Curr. Protoc. Cytom.* **Chapter 2**, Unit2.19 (2012).
40. Chiantia, S., Ries, J. & Schwille, P. Fluorescence correlation spectroscopy in membrane structure elucidation. *Biochim. Biophys. Acta - Biomembr.* **1788**, 225–233 (2009).
41. Vaz, W. L. C., Clegg, R. M. & Hallmann, D. Translational diffusion of lipids in liquid crystalline phase phosphatidylcholine multibilayers. A comparison of experiment with theory. (2002). doi:10.1021/BI00324A037
42. Cohen, M. H. & Turnbull, D. Molecular Transport in Liquids and Glasses. [http://oasc12039.247realmedia.com/RealMedia/ads/click\\_lx.ads/www.aip.org/pt/adcenter/pdfcover\\_test/L-37/2003863737/x01/AIP-PT/JCP\\_ArticleDL\\_091317/scilight717-1640x440.gif/434f71374e315a556e614141774c75?x](http://oasc12039.247realmedia.com/RealMedia/ads/click_lx.ads/www.aip.org/pt/adcenter/pdfcover_test/L-37/2003863737/x01/AIP-PT/JCP_ArticleDL_091317/scilight717-1640x440.gif/434f71374e315a556e614141774c75?x) (2004). doi:10.1063/1.1730566
43. Filippov, A., Orädd, G. & Lindblom, G. Domain formation in model membranes studied by pulsed-field gradient-NMR: the role of lipid polyunsaturation. *Biophys. J.* **93**, 3182–90 (2007).
44. Bacia, K., Scherfeld, D., Kahya, N. & Schwille, P. Fluorescence correlation spectroscopy relates rafts in model and native membranes. *Biophys. J.* **87**, 1034–43 (2004).
45. Lindblom, G. & Orädd, G. Lipid lateral diffusion and membrane heterogeneity. *Biochim. Biophys. Acta* **1788**, 234–44 (2009).
46. Shahedi, V., Orädd, G. & Lindblom, G. Domain-formation in DOPC/SM bilayers studied by pfg-NMR: effect of sterol structure. *Biophys. J.* **91**, 2501–7 (2006).
47. Kaiser, H.-J. *et al.* Lateral sorting in model membranes by cholesterol-mediated hydrophobic matching. *Proc. Natl. Acad. Sci. U. S. A.* **108**, 16628–33 (2011).

48. Marsh, D. Protein modulation of lipids, and vice-versa, in membranes. *Biochim. Biophys. Acta - Biomembr.* **1778**, 1545–1575 (2008).
49. East, J. M., Melville, D. & Lee, A. G. Exchange rates and numbers of annular lipids for the calcium and magnesium ion dependent adenosinetriphosphatase. *Biochemistry* **24**, 2615–23 (1985).
50. Lee, A. G. Lipid-protein interactions in biological membranes: a structural perspective. *Biochim. Biophys. Acta* **1612**, 1–40 (2003).
51. Schwarzer, R. *et al.* The cholesterol-binding motif of the HIV-1 glycoprotein gp41 regulates lateral sorting and oligomerization. *Cell. Microbiol.* **16**, 1565–1581 (2014).
52. Paila, Y. D., Tiwari, S. & Chattopadhyay, A. Are specific nonannular cholesterol binding sites present in G-protein coupled receptors? *Biochim. Biophys. Acta - Biomembr.* **1788**, 295–302 (2009).
53. Huang, C.-L., Feng, S. & Hilgemann, D. W. Direct activation of inward rectifier potassium channels by PIP2 and its stabilization by G $\beta$  | G $\gamma$ . *Nature* **391**, 803–806 (1998).
54. Gahbauer, S. & Böckmann, R. A. Membrane-Mediated Oligomerization of G Protein Coupled Receptors and Its Implications for GPCR Function. *Front. Physiol.* **7**, 494 (2016).
55. Yu, J., Fischman, D. A. & Steck, T. L. Selective solubilization of proteins and phospholipids from red blood cell membranes by nonionic detergents. *J. Supramol. Struct.* **1**, 233–248 (1973).
56. Schroeder, R., London, E. & Brown, D. Interactions between saturated acyl chains confer detergent resistance on lipids and glycosylphosphatidylinositol (GPI)-anchored proteins: GPI-anchored proteins in liposomes and cells show similar behavior. *Proc. Natl. Acad. Sci. U. S. A.* **91**, 12130–4 (1994).
57. Hanada, K., Nishijima, M., Akamatsu, Y. & Pagano, R. E. Both sphingolipids and cholesterol participate in the detergent insolubility of alkaline phosphatase, a glycosylphosphatidylinositol-anchored protein, in mammalian membranes. *J. Biol. Chem.* **270**, 6254–60 (1995).
58. Schuck, S., Honsho, M., Ekroos, K., Shevchenko, A. & Simons, K. Resistance of cell membranes to different detergents. *Proc. Natl. Acad. Sci. U. S. A.* **100**, 5795–800 (2003).
59. Sezgin, E. & Schwille, P. Fluorescence Techniques to Study Lipid Dynamics. *Cold Spring Harb. Perspect. Biol.* **3**, a009803–a009803 (2011).
60. Sezgin, E. & Schwille, P. **Model membrane platforms to study protein-membrane interactions.** *Mol. Membr. Biol.* **29**, 144–154 (2012).
61. Lozano, M. M. *et al.* Colocalization of the ganglioside G(M1) and cholesterol detected by secondary ion mass spectrometry. *J. Am. Chem. Soc.* **135**, 5620–30 (2013).
62. Brown, D. A. & Rose, J. K. Sorting of GPI-anchored proteins to glycolipid-enriched membrane subdomains during transport to the apical cell surface. *Cell* **68**, 533–44 (1992).
63. Kiessling, V., Wan, C. & Tamm, L. K. Domain coupling in asymmetric lipid bilayers. *Biochim. Biophys. Acta - Biomembr.* **1788**, 64–71 (2009).
64. Villar, V. A. M., Cuevas, S., Zheng, X. & Jose, P. A. Localization and signaling of GPCRs in lipid rafts. in 3–23 (2016). doi:10.1016/bs.mcb.2015.11.008
65. Lingwood, D. & Simons, K. Lipid Rafts As a Membrane-Organizing Principle. *Science (80-. ).* **327**, 46–50 (2010).
66. Sengupta, P. *et al.* Probing protein heterogeneity in the plasma membrane using PALM and pair correlation analysis. *Nat. Methods* **8**, 969–75 (2011).
67. Owen, D. M., Williamson, D. J., Magenau, A. & Gaus, K. Sub-resolution lipid domains exist in the plasma membrane and regulate protein diffusion and distribution. *Nat. Commun.* **3**, 1256 (2012).
68. Ando, J. *et al.* Sphingomyelin distribution in lipid rafts of artificial monolayer membranes visualized by Raman microscopy. *Proc. Natl. Acad. Sci.* **112**, 4558–4563 (2015).
69. Pencer, J., Mills, T. T., Kucerka, N., Nieh, M.-P. & Katsaras, J. Small-Angle Neutron Scattering to Detect Rafts and Lipid Domains. in *Methods in molecular biology (Clifton, N.J.)*

- 398**, 231–244 (2007).
70. Filipp, D., Leung, B. L., Zhang, J., Veillette, A. & Julius, M. Enrichment of Ick in lipid rafts regulates colocalized fyn activation and the initiation of proximal signals through TCR alpha beta. *J. Immunol.* **172**, 4266–74 (2004).
  71. Laganowsky, A. *et al.* Membrane proteins bind lipids selectively to modulate their structure and function. *Nature* **510**, 172–175 (2014).
  72. Sezgin, E., Levental, I., Mayor, S. & Eggeling, C. The mystery of membrane organization: composition, regulation and roles of lipid rafts. *Nat. Rev. Mol. Cell Biol.* **18**, 361–374 (2017).
  73. Pelkmans, L. & Helenius, A. Endocytosis via caveolae. *Traffic* **3**, 311–20 (2002).
  74. Parton, R. G. & Simons, K. The multiple faces of caveolae. *Nat. Rev. Mol. Cell Biol.* **8**, 185–194 (2007).
  75. Valadi, H. *et al.* Exosome-mediated transfer of mRNAs and microRNAs is a novel mechanism of genetic exchange between cells. *Nat. Cell Biol.* **9**, 654–659 (2007).
  76. Ratajczak, J., Wysoczynski, M., Hayek, F., Janowska-Wieczorek, A. & Ratajczak, M. Z. Membrane-derived microvesicles: important and underappreciated mediators of cell-to-cell communication. *Leukemia* **20**, 1487–1495 (2006).
  77. de Gassart, A., Geminard, C., Fevrier, B., Raposo, G. & Vidal, M. Lipid raft-associated protein sorting in exosomes. *Blood* **102**, 4336–44 (2003).
  78. Echarri, A. & Del Pozo, M. A. Caveolae – mechanosensitive membrane invaginations linked to actin filaments. *J. Cell Sci.* **128**, (2015).
  79. Pike, L. J. The challenge of lipid rafts. *J. Lipid Res.* **50**, S323–S328 (2009).
  80. Dupree, J. L. & Pomicter, A. D. Myelin, DIGs, and membrane rafts in the central nervous system. *Prostaglandins Other Lipid Mediat.* **91**, 118–129 (2010).
  81. Balasubramanian, N., Scott, D. W., Castle, J. D., Casanova, J. E. & Schwartz, M. A. Arf6 and microtubules in adhesion-dependent trafficking of lipid rafts. *Nat. Cell Biol.* **9**, 1381–91 (2007).
  82. Pryor, S., McCaffrey, G., Young, L. R., Grimes, M. L. & Dedhar, S. NGF Causes TrkA to Specifically Attract Microtubules to Lipid Rafts. *PLoS One* **7**, e35163 (2012).
  83. Field, K. A., Holowka, D. & Baird, B. Fc epsilon RI-mediated recruitment of p53/56lyn to detergent-resistant membrane domains accompanies cellular signaling. *Proc. Natl. Acad. Sci. U. S. A.* **92**, 9201–5 (1995).
  84. Rivera, J., Arudchandran, R., Gonzalez-Espinosa, C., Manetz, T. S. & Xirasagar, S. A perspective: regulation of IgE receptor-mediated mast cell responses by a LAT-organized plasma membrane-localized signaling complex. *Int. Arch. Allergy Immunol.* **124**, 137–41
  85. Stone, M. B., Shelby, S. A., Núñez, M. F., Wisser, K. & Veatch, S. L. Protein sorting by lipid phase-like domains supports emergent signaling function in B lymphocyte plasma membranes. *Elife* **6**, (2017).
  86. Gupta, N. & DeFranco, A. L. Visualizing Lipid Raft Dynamics and Early Signaling Events during Antigen Receptor-mediated B-Lymphocyte Activation. *Mol. Biol. Cell* **14**, 432–444 (2003).
  87. Dinic, J., Riehl, A., Adler, J. & Parmryd, I. The T cell receptor resides in ordered plasma membrane nanodomains that aggregate upon patching of the receptor. *Sci. Rep.* **5**, 10082 (2015).
  88. Wright, S. D., Ramos, R. A., Tobias, P. S., Ulevitch, R. J. & Mathison, J. C. CD14, a receptor for complexes of lipopolysaccharide (LPS) and LPS binding protein. *Science* **249**, 1431–3 (1990).
  89. Gielen, E. *et al.* Rafts in oligodendrocytes: Evidence and structure–function relationship. *Glia* **54**, 499–512 (2006).
  90. Suzuki, T. Lipid rafts at postsynaptic sites: distribution, function and linkage to postsynaptic density. *Neurosci. Res.* **44**, 1–9 (2002).
  91. Linetti, A. *et al.* Cholesterol reduction impairs exocytosis of synaptic vesicles. *J. Cell Sci.* **123**, 595–605 (2010).

92. Gil, C., Soler-Jover, A., Blasi, J. & Aguilera, J. Synaptic proteins and SNARE complexes are localized in lipid rafts from rat brain synaptosomes. *Biochem. Biophys. Res. Commun.* **329**, 117–124 (2005).
93. Patra, S. K. Dissecting lipid raft facilitated cell signaling pathways in cancer. *Biochim. Biophys. Acta - Rev. Cancer* **1785**, 182–206 (2008).
94. Hanahan, D. *et al.* Hallmarks of Cancer: The Next Generation. *Cell* **144**, 646–674 (2011).
95. Murai, T. *et al.* Low Cholesterol Triggers Membrane Microdomain-dependent CD44 Shedding and Suppresses Tumor Cell Migration. *J. Biol. Chem.* **286**, 1999–2007 (2011).
96. Pande, G. The role of membrane lipids in regulation of integrin functions. *Curr. Opin. Cell Biol.* **12**, 569–74 (2000).
97. Hitosugi, T., Sato, M., Sasaki, K. & Umezawa, Y. Lipid Raft Specific Knockdown of Src Family Kinase Activity Inhibits Cell Adhesion and Cell Cycle Progression of Breast Cancer Cells. *Cancer Res.* **67**, 8139–8148 (2007).
98. Söderström, T. S., Nyberg, S. D. & Eriksson, J. E. CD95 capping is ROCK-dependent and dispensable for apoptosis. *J. Cell Sci.* **118**, (2005).
99. Michel, V. & Bakovic, M. Lipid rafts in health and disease. *Biol. Cell* **99**, 129–140 (2007).
100. Marsh, M. & Helenius, A. Virus Entry: Open Sesame. *Cell* **124**, 729–740 (2006).
101. Teissier, É. & Pécheur, E.-I. Lipids as modulators of membrane fusion mediated by viral fusion proteins. *Eur. Biophys. J.* **36**, 887–899 (2007).
102. Iwabuchi, K. Involvement of glycosphingolipid-enriched lipid rafts in inflammatory responses. *Front. Biosci. (Landmark Ed.)* **20**, 325–34 (2015).
103. Harder, T., Scheiffele, P., Verkade, P. & Simons, K. Lipid Domain Structure of the Plasma Membrane Revealed by Patching of Membrane Components. *J. Cell Biol.* **141**, (1998).
104. Kamiyama, H. *et al.* Raft localization of CXCR4 is primarily required for X4-tropic human immunodeficiency virus type 1 infection. *Virology* **386**, 23–31 (2009).
105. Millán, J., Cerny, J., Horejsi, V. & Alonso, M. A. CD4 segregates into specific detergent-resistant T-cell membrane microdomains. *Tissue Antigens* **53**, 33–40 (1999).
106. Sviridov, D. & Bukrinsky, M. Interaction of pathogens with host cholesterol metabolism. *Curr. Opin. Lipidol.* **25**, 333–8 (2014).
107. Zuo, L. *et al.* Caveolin-1 Is Essential for Activation of Rac1 and NAD(P)H Oxidase After Angiotensin II Type 1 Receptor Stimulation in Vascular Smooth Muscle Cells: Role in Redox Signaling and Vascular Hypertrophy. *Arterioscler. Thromb. Vasc. Biol.* **25**, 1824–1830 (2005).
108. MAGUY, A. *et al.* Involvement of lipid rafts and caveolae in cardiac ion channel function. *Cardiovasc. Res.* **69**, 798–807 (2006).
109. Shashkin, P., Dragulev, B. & Ley, K. Macrophage Differentiation to Foam Cells. *Curr. Pharm. Des.* **11**, 3061–3072 (2005).
110. Rios, F. J. O. *et al.* Uptake of oxLDL and IL-10 Production by Macrophages Requires PAFR and CD36 Recruitment into the Same Lipid Rafts. *PLoS One* **8**, e76893 (2013).
111. Schengrund, C.-L. Lipid rafts: Keys to neurodegeneration. *Brain Res. Bull.* **82**, 7–17 (2010).
112. Marin, R. *et al.* Lipid Raft Alterations in Aged - Associated Neuropathologies. (2015). doi:10.2174/1567205013666160314150017
113. Schneider, A. *et al.* Flotillin-Dependent Clustering of the Amyloid Precursor Protein Regulates Its Endocytosis and Amyloidogenic Processing in Neurons. *J. Neurosci.* **28**, 2874–2882 (2008).
114. Bhattacharyya, R., Barren, C. & Kovacs, D. M. Palmitoylation of Amyloid Precursor Protein Regulates Amyloidogenic Processing in Lipid Rafts. *J. Neurosci.* **33**, 11169–11183 (2013).
115. Kalvodova, L. *et al.* Lipids as Modulators of Proteolytic Activity of BACE. *J. Biol. Chem.* **280**, 36815–36823 (2005).
116. Matsumura, N. *et al.*  $\gamma$ -Secretase Associated with Lipid Rafts. *J. Biol. Chem.* **289**, 5109–5121 (2014).
117. Hannaoui, S., Shim, S. Y., Cheng, Y. C., Corda, E. & Gilch, S. Cholesterol balance in prion diseases and Alzheimer's disease. *Viruses* **6**, 4505–35 (2014).

118. Krebs, M. R. H., Bromley, E. H. C. & Donald, A. M. The binding of thioflavin-T to amyloid fibrils: localisation and implications. *J. Struct. Biol.* **149**, 30–37 (2005).
119. NILSSON, M. Techniques to study amyloid fibril formation in vitro. *Methods* **34**, 151–160 (2004).
120. Klunk, W. E., Pettegrew, J. W. & Abraham, D. J. Quantitative evaluation of congo red binding to amyloid-like proteins with a beta-pleated sheet conformation. *J. Histochem. Cytochem.* **37**, 1273–1281 (1989).
121. Kumar, S. & Udgaonkar, J. B. Mechanisms of amyloid fibril formation by proteins. *Current Science* **98**, 639–656
122. Malchiodi-Albedi, F., Paradisi, S., Matteucci, A., Frank, C. & Diociaiuti, M. Amyloid Oligomer Neurotoxicity, Calcium Dysregulation, and Lipid Rafts. *Int. J. Alzheimers. Dis.* **2011**, 1–17 (2011).
123. Beyer, K. Mechanistic aspects of Parkinson's disease: alpha-synuclein and the biomembrane. *Cell Biochem. Biophys.* **47**, 285–99 (2007).
124. Kostka, M. *et al.* Single particle characterization of iron-induced pore-forming alpha-synuclein oligomers. *J. Biol. Chem.* **283**, 10992–1003 (2008).
125. Jellinger, K. A. A critical reappraisal of current staging of Lewy-related pathology in human brain. *Acta Neuropathol.* **116**, 1–16 (2008).
126. Gelb, D. J. *et al.* Diagnostic Criteria for Parkinson Disease. *Arch. Neurol.* **56**, 33 (1999).
127. Hughes, A. J., Daniel, S. E., Kilford, L. & Lees, A. J. Accuracy of clinical diagnosis of idiopathic Parkinson's disease: a clinico-pathological study of 100 cases. *J. Neurol. Neurosurg. Psychiatry* **55**, 181–4 (1992).
128. Beach, T. G. *et al.* Unified staging system for Lewy body disorders: correlation with nigrostriatal degeneration, cognitive impairment and motor dysfunction. *Acta Neuropathol.* **117**, 613–634 (2009).
129. Spillantini, M. G. *et al.*  $\alpha$ -Synuclein in Lewy bodies. *Nature* **388**, 839–840 (1997).
130. Goedert, M. Alpha-synuclein and neurodegenerative diseases. *Nat. Rev. Neurosci.* **2**, 492–501 (2001).
131. Taipa, R., Pinho, J. & Melo-Pires, M. Clinico-Pathological Correlations of the Most Common Neurodegenerative Dementias. *Front. Neurol.* **3**, 68 (2012).
132. Langston, J. W., Ballard, P., Tetrud, J. W. & Irwin, I. Chronic Parkinsonism in humans due to a product of meperidine-analog synthesis. *Science* **219**, 979–80 (1983).
133. Klein, C. & Westenberger, A. Genetics of Parkinson's disease. *Cold Spring Harb. Perspect. Med.* **2**, a008888 (2012).
134. Polymeropoulos, M. H. *et al.* Mutation in the  $\alpha$ -Synuclein Gene Identified in Families with Parkinson's Disease. *Science (80-. )*. **276**, (1997).
135. Pasanen, P. *et al.* A novel  $\alpha$ -synuclein mutation A53E associated with atypical multiple system atrophy and Parkinson's disease-type pathology. *Neurobiol. Aging* **35**, 2180.e1-2180.e5 (2014).
136. Proukakis, C. *et al.* A novel  $\alpha$ -synuclein missense mutation in Parkinson disease. *Neurology* **80**, 1062–4 (2013).
137. Kiely, A. P. *et al.*  $\alpha$ -Synucleinopathy associated with G51D SNCA mutation: a link between Parkinson's disease and multiple system atrophy? *Acta Neuropathol.* **125**, 753–769 (2013).
138. Lesage, S. *et al.* G51D  $\alpha$ -synuclein mutation causes a novel Parkinsonian-pyramidal syndrome. *Ann. Neurol.* **73**, 459–471 (2013).
139. Krüger, R. *et al.* AlaSOPro mutation in the gene encoding  $\alpha$ -synuclein in Parkinson's disease. *Nat. Genet.* **18**, 106–108 (1998).
140. Zarranz, J. J. *et al.* The new mutation, E46K, of  $\alpha$ -synuclein causes parkinson and Lewy body dementia. *Ann. Neurol.* **55**, 164–173 (2004).
141. Rochet, J.-C., Hay, B. A. & Guo, M. Molecular Insights into Parkinson's Disease. in *Progress in molecular biology and translational science* **107**, 125–188 (2012).
142. Wood-Kaczmar, A., Gandhi, S. & Wood, N. W. Understanding the molecular causes of Parkinson's disease. *Trends Mol. Med.* **12**, 521–528 (2006).

143. Singleton, A. B. *et al.* -Synuclein Locus Triplication Causes Parkinson's Disease. *Science* (80-). **302**, 841–841 (2003).
144. Chartier-Harlin, M.-C. *et al.*  $\alpha$ -synuclein locus duplication as a cause of familial Parkinson's disease. *Lancet* **364**, 1167–1169 (2004).
145. Lo Bianco, C., Ridet, J.-L., Schneider, B. L., Deglon, N. & Aebischer, P. -Synucleinopathy and selective dopaminergic neuron loss in a rat lentiviral-based model of Parkinson's disease. *Proc. Natl. Acad. Sci.* **99**, 10813–10818 (2002).
146. Giasson, B. I. *et al.* Neuronal alpha-synucleinopathy with severe movement disorder in mice expressing A53T human alpha-synuclein. *Neuron* **34**, 521–33 (2002).
147. Kahle, P. J. *et al.* Selective insolubility of alpha-synuclein in human Lewy body diseases is recapitulated in a transgenic mouse model. *Am. J. Pathol.* **159**, 2215–25 (2001).
148. Masliah, E. *et al.* Dopaminergic loss and inclusion body formation in alpha-synuclein mice: implications for neurodegenerative disorders. *Science* **287**, 1265–9 (2000).
149. Bertonecini, C. W. *et al.* From The Cover: Release of long-range tertiary interactions potentiates aggregation of natively unstructured  $\alpha$ -synuclein. *Proc. Natl. Acad. Sci.* **102**, 1430–1435 (2005).
150. Uversky, V. N., Gillespie, J. R. & Fink, A. L. Why are "natively unfolded" proteins unstructured under physiologic conditions? *Proteins* **41**, 415–27 (2000).
151. Segrest, J. P. *et al.* The amphipathic helix in the exchangeable apolipoproteins: a review of secondary structure and function. *J. Lipid Res.* **33**, 141–66 (1992).
152. Bisaglia, M., Schievano, E., Caporale, A., Peggion, E. & Mammi, S. The 11-mer repeats of human  $\alpha$ -synuclein in vesicle interactions and lipid composition discrimination: A cooperative role. *Biopolymers* **84**, 310–316 (2006).
153. Bodles, A. M., Guthrie, D. J., Greer, B. & Irvine, G. B. Identification of the region of non-A $\beta$  component (NAC) of Alzheimer's disease amyloid responsible for its aggregation and toxicity. *J. Neurochem.* **78**, 384–95 (2001).
154. Giasson, B. I., Murray, I. V. J., Trojanowski, J. Q. & Lee, V. M.-Y. A Hydrophobic Stretch of 12 Amino Acid Residues in the Middle of  $\alpha$ -Synuclein Is Essential for Filament Assembly\*. (2000). doi:10.1074/jbc.M008919200
155. Murray, I. V. J. *et al.* Role of  $\alpha$ -Synuclein Carboxy-Terminus on Fibril Formation in Vitro<sup>†</sup>. *Biochemistry* **42**, 8530–8540 (2003).
156. Ghosh, D., Mehra, S., Sahay, S., Singh, P. K. & Maji, S. K.  $\alpha$ -synuclein aggregation and its modulation. *Int. J. Biol. Macromol.* **100**, 37–54 (2017).
157. Burré, J., Sharma, M. & Südhof, T. C.  $\alpha$ -Synuclein assembles into higher-order multimers upon membrane binding to promote SNARE complex formation. *Proc. Natl. Acad. Sci.* **111**, E4274–E4283 (2014).
158. Burre, J. *et al.* -Synuclein Promotes SNARE-Complex Assembly in Vivo and in Vitro. *Science* (80-). **329**, 1663–1667 (2010).
159. Scott, D. & Roy, S. -Synuclein Inhibits Intersynaptic Vesicle Mobility and Maintains Recycling-Pool Homeostasis. *J. Neurosci.* **32**, 10129–10135 (2012).
160. Emamzadeh, F. N. Alpha-synuclein structure, functions, and interactions. *J. Res. Med. Sci. Wolters Kluwer - Medknow* **1**, (2016).
161. Wersinger, C. & Sidhu, A. Attenuation of dopamine transporter activity by alpha-synuclein. *Neurosci. Lett.* **340**, 189–92 (2003).
162. Lee, F. J., Liu, F., Pristupa, Z. B. & Niznik, H. B. Direct binding and functional coupling of alpha-synuclein to the dopamine transporters accelerate dopamine-induced apoptosis. *FASEB J.* **15**, 916–26 (2001).
163. Fu, H., Subramanian, R. R. & Masters, S. C. 14-3-3 Proteins: Structure, Function, and Regulation. *Annu. Rev. Pharmacol. Toxicol.* **40**, 617–647 (2000).
164. Ruipérez, V., Darios, F. & Davletov, B. Alpha-synuclein, lipids and Parkinson's disease. *Prog. Lipid Res.* **49**, 420–428 (2010).
165. Jin, H. *et al.* -Synuclein Negatively Regulates Protein Kinase C Expression to Suppress Apoptosis in Dopaminergic Neurons by Reducing p300 Histone Acetyltransferase Activity.

- J. Neurosci.* **31**, 2035–2051 (2011).
166. Lashuel, H. A., Overk, C. R., Oueslati, A. & Masliah, E. The many faces of  $\alpha$ -synuclein: from structure and toxicity to therapeutic target. *Nat. Rev. Neurosci.* **14**, 38–48 (2012).
  167. Eschbach, J. & Danzer, K. M.  $\alpha$ -Synuclein in Parkinson's Disease: Pathogenic Function and Translation into Animal Models. *Neurodegener. Dis.* **14**, 1–17 (2014).
  168. Uversky, V. N. A Protein-Chameleon: Conformational Plasticity of  $\alpha$ -Synuclein, a Disordered Protein Involved in Neurodegenerative Disorders. *J. Biomol. Struct. Dyn.* **21**, 211–234 (2003).
  169. Kelly A. Conway, James D. Harper, and Peter T. Lansbury, J. . Fibrils Formed in Vitro from  $\alpha$ -Synuclein and Two Mutant Forms Linked to Parkinson's Disease are Typical Amyloid $\dagger$ . (2000). doi:10.1021/BI991447R
  170. Giasson, B. I., Uryu, K., Trojanowski, J. Q. & Lee, V. M. Mutant and wild type human alpha-synucleins assemble into elongated filaments with distinct morphologies in vitro. *J. Biol. Chem.* **274**, 7619–22 (1999).
  171. Fink, A. L. The Aggregation and Fibrillation of  $\alpha$ -Synuclein. *Acc. Chem. Res.* **39**, 628–634 (2006).
  172. Uversky, V. N., Li, J. & Fink, A. L. Evidence for a partially folded intermediate in alpha-synuclein fibril formation. *J. Biol. Chem.* **276**, 10737–44 (2001).
  173. Uversky, V. N. *et al.* Biophysical properties of the synucleins and their propensities to fibrillate: inhibition of alpha-synuclein assembly by beta- and gamma-synucleins. *J. Biol. Chem.* **277**, 11970–8 (2002).
  174. Kaylor, J. *et al.* Characterization of Oligomeric Intermediates in  $\alpha$ -Synuclein Fibrillation: FRET Studies of Y125W/Y133F/Y136F  $\alpha$ -Synuclein. *J. Mol. Biol.* **353**, 357–372 (2005).
  175. Horvath, I. *et al.* Mechanisms of Protein Oligomerization: Inhibitor of Functional Amyloids Templates  $\alpha$ -Synuclein Fibrillation. *J. Am. Chem. Soc.* **134**, 3439–3444 (2012).
  176. Munishkina, L. A., Phelan, C., Uversky, V. N. & Fink, A. L. Conformational Behavior and Aggregation of  $\alpha$ -Synuclein in Organic Solvents: Modeling the Effects of Membranes $^\dagger$ . *Biochemistry* **42**, 2720–2730 (2003).
  177. Buell, A. K. *et al.* Solution conditions determine the relative importance of nucleation and growth processes in  $\alpha$ -synuclein aggregation. *Proc. Natl. Acad. Sci. U. S. A.* **111**, 7671–6 (2014).
  178. Conway, K. A. *et al.* Acceleration of oligomerization, not fibrillization, is a shared property of both alpha-synuclein mutations linked to early-onset Parkinson's disease: implications for pathogenesis and therapy. *Proc. Natl. Acad. Sci. U. S. A.* **97**, 571–6 (2000).
  179. Conway, K. A., Harper, J. D. & Lansbury, P. T. Accelerated in vitro fibril formation by a mutant  $\alpha$ -synuclein linked to early-onset Parkinson disease. *Nat. Med.* **4**, 1318–1320 (1998).
  180. Choi, W. *et al.* Mutation E46K increases phospholipid binding and assembly into filaments of human  $\alpha$ -synuclein. *FEBS Lett.* **576**, 363–368 (2004).
  181. Ingelsson, M. Alpha-Synuclein Oligomers-Neurotoxic Molecules in Parkinson's Disease and Other Lewy Body Disorders. *Front. Neurosci.* **10**, 408 (2016).
  182. Winner, B. *et al.* In vivo demonstration that  $\alpha$ -synuclein oligomers are toxic. *Proc. Natl. Acad. Sci.* **108**, 4194–4199 (2011).
  183. Taschenberger, G. *et al.* Aggregation of  $\alpha$ Synuclein promotes progressive in vivo neurotoxicity in adult rat dopaminergic neurons. *Acta Neuropathol.* **123**, 671–683 (2012).
  184. Martin, Z. S. *et al.*  $\alpha$ -Synuclein oligomers oppose long-term potentiation and impair memory through a calcineurin-dependent mechanism: relevance to human synucleopathic diseases. *J. Neurochem.* **120**, 440–452 (2012).
  185. Kahle, P. J. *et al.* Subcellular localization of wild-type and Parkinson's disease-associated mutant alpha -synuclein in human and transgenic mouse brain. *J. Neurosci.* **20**, 6365–73 (2000).
  186. Tsigelny, I. F. *et al.* Mechanisms of Hybrid Oligomer Formation in the Pathogenesis of Combined Alzheimer's and Parkinson's Diseases. *PLoS One* **3**, e3135 (2008).

187. Danzer, K. M. *et al.* Different Species of  $\alpha$ -Synuclein Oligomers Induce Calcium Influx and Seeding. *J. Neurosci.* **27**, 9220–9232 (2007).
188. Scott, D. A. *et al.* A Pathologic Cascade Leading to Synaptic Dysfunction in  $\alpha$ -Synuclein-Induced Neurodegeneration. *J. Neurosci.* **30**, 8083–8095 (2010).
189. Rockenstein, E. *et al.* Accumulation of oligomer-prone  $\alpha$ -synuclein exacerbates synaptic and neuronal degeneration in vivo. *Brain* **137**, 1496–1513 (2014).
190. Olanow, C. W. & Brundin, P. Parkinson's Disease and Alpha Synuclein: Is Parkinson's Disease a Prion-Like Disorder? *Mov. Disord.* **28**, 31–40 (2013).
191. Volpicelli-Daley, L. A. *et al.* Exogenous  $\alpha$ -Synuclein Fibrils Induce Lewy Body Pathology Leading to Synaptic Dysfunction and Neuron Death. *Neuron* **72**, 57–71 (2011).
192. Snead, D. & Eliezer, D. Alpha-Synuclein Function and Dysfunction on Cellular Membranes. *Exp. Neurobiol.* **23**, 292 (2014).
193. De Franceschi, G. *et al.* Structural and morphological characterization of aggregated species of  $\alpha$ -synuclein induced by docosahexaenoic acid. *J. Biol. Chem.* **286**, 22262–74 (2011).
194. Cole, N. B. *et al.* Lipid droplet binding and oligomerization properties of the Parkinson's disease protein alpha-synuclein. *J. Biol. Chem.* **277**, 6344–52 (2002).
195. The Formation of Highly Soluble Oligomers of  $\alpha$ -Synuclein Is Regulated by Fatty Acids and Enhanced in Parkinson's Disease. *Neuron* **37**, 583–595 (2003).
196. Zhu, M., Li, J. & Fink, A. L. The association of alpha-synuclein with membranes affects bilayer structure, stability, and fibril formation. *J. Biol. Chem.* **278**, 40186–97 (2003).
197. Necula, M., Chirita, C. N. & Kuret, J. Rapid anionic micelle-mediated alpha-synuclein fibrillization in vitro. *J. Biol. Chem.* **278**, 46674–80 (2003).
198. Lee, H.-J., Choi, C. & Lee, S.-J. Membrane-bound alpha-synuclein has a high aggregation propensity and the ability to seed the aggregation of the cytosolic form. *J. Biol. Chem.* **277**, 671–8 (2002).
199. Rivers, R. C. *et al.* Molecular determinants of the aggregation behavior of  $\alpha$ - and  $\beta$ -synuclein. *Protein Sci.* **17**, 887–898 (2008).
200. The N-Terminus of the Intrinsically Disordered Protein  $\alpha$ -Synuclein Triggers Membrane Binding and Helix Folding. *Biophys. J.* **99**, 2116–2124 (2010).
201. Bodner, C. R., Maltsev, A. S., Dobson, C. M. & Bax, A. Differential Phospholipid Binding of  $\alpha$ -Synuclein Variants Implicated in Parkinson's Disease Revealed by Solution NMR Spectroscopy. *Biochemistry* **49**, 862–871 (2010).
202. Fusco, G. *et al.* Direct observation of the three regions in  $\alpha$ -synuclein that determine its membrane-bound behaviour. *Nat. Commun.* **5**, 3827 (2014).
203. Ulmer, T. S., Bax, A., Cole, N. B. & Nussbaum, R. L. Structure and dynamics of micelle-bound human alpha-synuclein. *J. Biol. Chem.* **280**, 9595–603 (2005).
204. Davidson, W. S., Jonas, A., Clayton, D. F. & George, J. M. Stabilization of alpha-synuclein secondary structure upon binding to synthetic membranes. *J. Biol. Chem.* **273**, 9443–9 (1998).
205.  $\alpha$ -Synuclein Selectively Binds to Anionic Phospholipids Embedded in Liquid-Disordered Domains. *J. Mol. Biol.* **375**, 1394–1404 (2008).
206. Pfefferkorn, C. M., Jiang, Z. & Lee, J. C. Biophysics of  $\alpha$ -synuclein membrane interactions. *Biochim. Biophys. Acta - Biomembr.* **1818**, 162–171 (2012).
207. Effects of Curvature and Composition on  $\alpha$ -Synuclein Binding to Lipid Vesicles. *Biophys. J.* **99**, 2279–2288 (2010).
208. Ghosh, D. *et al.* The Newly Discovered Parkinson's Disease Associated Finnish Mutation (A53E) Attenuates  $\alpha$ -Synuclein Aggregation and Membrane Binding. *Biochemistry* **53**, 6419–6421 (2014).
209. Kubo, S. *et al.* A combinatorial code for the interaction of alpha-synuclein with membranes. *J. Biol. Chem.* **280**, 31664–72 (2005).
210. McMahon, H. T. & Gallop, J. L. Membrane curvature and mechanisms of dynamic cell membrane remodelling. *Nature* **438**, 590–596 (2005).

211. Kamp, F. & Beyer, K. Binding of alpha-synuclein affects the lipid packing in bilayers of small vesicles. *J. Biol. Chem.* **281**, 9251–9 (2006).
212. The Influence of Vesicle Size and Composition on  $\alpha$ -Synuclein Structure and Stability. *Biophys. J.* **96**, 2857–2870 (2009).
213. Fortin, D. L. *et al.* Lipid Rafts Mediate the Synaptic Localization of  $\alpha$ -Synuclein. doi:10.1523/JNEUROSCI.1594-04.2004
214. Martinez, Z., Zhu, M., Han, S. & Fink, A. L. GM1 Specifically Interacts with  $\alpha$ -Synuclein and Inhibits Fibrillation. doi:10.1021/bi061749a
215. van Rooijen, B. D., Claessens, M. M. A. E. & Subramaniam, V. Membrane interactions of oligomeric alpha-synuclein: potential role in Parkinson's disease. *Curr. Protein Pept. Sci.* **11**, 334–42 (2010).
216. Lorenzen, N., Lemminger, L., Pedersen, J. N., Nielsen, S. B. & Otzen, D. E. The N-terminus of  $\alpha$ -synuclein is essential for both monomeric and oligomeric interactions with membranes. *FEBS Lett.* **588**, 497–502 (2014).
217. Two Different Binding Modes of  $\alpha$ -Synuclein to Lipid Vesicles Depending on its Aggregation State. *Biophys. J.* **102**, 1646–1655 (2012).
218. Stöckl, M., Claessens, M. M. A. E. & Subramaniam, V. Kinetic measurements give new insights into lipid membrane permeabilization by  $\alpha$ -synuclein oligomers. *Mol. Biosyst.* **8**, 338–345 (2012).
219. Andreasen, M., Lorenzen, N. & Otzen, D. Interactions between misfolded protein oligomers and membranes: A central topic in neurodegenerative diseases? *Biochim. Biophys. Acta - Biomembr.* **1848**, 1897–1907 (2015).
220.  $\alpha$ -Synuclein, Especially the Parkinson's Disease-associated Mutants, Forms Pore-like Annular and Tubular Protofibrils. *J. Mol. Biol.* **322**, 1089–1102 (2002).
221. and, M. J. V. & Peter T. Lansbury, J. . Vesicle Permeabilization by Protofibrillar  $\alpha$ -Synuclein Is Sensitive to Parkinson's Disease-Linked Mutations and Occurs by a Pore-like Mechanism†. (2002). doi:10.1021/BI0121353
222. Kim, H.-Y. *et al.* Structural Properties of Pore-Forming Oligomers of  $\alpha$ -Synuclein. *J. Am. Chem. Soc.* **131**, 17482–17489 (2009).
223. Pacheco, C., Aguayo, L. G. & Opazo, C. An extracellular mechanism that can explain the neurotoxic effects of  $\alpha$ -synuclein aggregates in the brain. *Front. Physiol.* **3**, 297 (2012).
224. Riederer, P. *et al.* Transition metals, ferritin, glutathione, and ascorbic acid in parkinsonian brains. *J. Neurochem.* **52**, 515–20 (1989).
225. Gorell, J. M., Rybicki, B. A., Cole Johnson, C. & Peterson, E. L. Occupational metal exposures and the risk of Parkinson's disease. *Neuroepidemiology* **18**, 303–8 (1999).
226. Uversky, V. N., Li, J. & Fink, A. L. Metal-triggered Structural Transformations, Aggregation, and Fibrillation of Human  $\alpha$ -Synuclein. *J. Biol. Chem.* **276**, 44284–44296 (2001).
227. Dexter, D. T. *et al.* Increased nigral iron content and alterations in other metal ions occurring in brain in Parkinson's disease. *J. Neurochem.* **52**, 1830–6 (1989).
228. Hirsch, E. C., Brandel, J. P., Galle, P., Javoy-Agid, F. & Agid, Y. Iron and aluminum increase in the substantia nigra of patients with Parkinson's disease: an X-ray microanalysis. *J. Neurochem.* **56**, 446–51 (1991).
229. Dexter, D. T. *et al.* Alterations in the levels of iron, ferritin and other trace metals in Parkinson's disease and other neurodegenerative diseases affecting the basal ganglia. *Brain* **114 ( Pt 4)**, 1953–75 (1991).
230. Uversky, V. N., Li, J. & Fink, A. L. Evidence for a Partially Folded Intermediate in  $\alpha$ -Synuclein Fibril Formation. *J. Biol. Chem.* **276**, 10737–10744 (2001).
231. Binolfi, A. *et al.* Interaction of  $\alpha$ -Synuclein with Divalent Metal Ions Reveals Key Differences: A Link between Structure, Binding Specificity and Fibrillation Enhancement. *J. Am. Chem. Soc.* **128**, 9893–9901 (2006).
232. Martin-Bastida, A. *et al.* Motor associations of iron accumulation in deep grey matter nuclei in Parkinson's disease: a cross-sectional study of iron-related magnetic resonance imaging susceptibility. *Eur. J. Neurol.* **24**, 357–365 (2017).

233. Lhermitte, J., Kraus, W. M. & McAlpine, D. Original Papers: ON THE OCCURRENCE OF ABNORMAL DEPOSITS OF IRON IN THE BRAIN IN PARKINSONISM WITH SPECIAL REFERENCE TO ITS LOCALISATION. *J. Neurol. Psychopathol.* **5**, 195–208 (1924).
234. Li, K. & Reichmann, H. Role of iron in neurodegenerative diseases. *J. Neural Transm.* **123**, 389–399 (2016).
235. Ortega, R. *et al.*  $\alpha$ -Synuclein Over-Expression Induces Increased Iron Accumulation and Redistribution in Iron-Exposed Neurons. *Mol. Neurobiol.* **53**, 1925–1934 (2016).
236. Ostrerova-Golts, N. *et al.* The A53T alpha-synuclein mutation increases iron-dependent aggregation and toxicity. *J. Neurosci.* **20**, 6048–54 (2000).
237. Febbraro, F., Giorgi, M., Caldarola, S., Loreni, F. & Romero-Ramos, M.  $\alpha$ -Synuclein expression is modulated at the translational level by iron. *Neuroreport* **23**, 576–580 (2012).
238. Peetla, C., Stine, A. & Labhasetwar, V. Biophysical Interactions with Model Lipid Membranes: Applications in Drug Discovery and Drug Delivery. *Mol. Pharm.* **6**, 1264–1276 (2009).
239. Kiessling, V., Yang, S.-T. & Tamm, L. K. *Supported Lipid Bilayers as Models for Studying Membrane Domains. Current topics in membranes* **75**, 1–23 (Academic Press, 2015).
240. Holger Schönherr, \*, †, ‡, †, Joseph M. Johnson, †, §, Peter Lenz, §, #, Curtis W. Frank, †, ‡ and Steven G. Boxer†, §. Vesicle Adsorption and Lipid Bilayer Formation on Glass Studied by Atomic Force Microscopy. (2004). doi:10.1021/LA049302V
241. and, H. E. & Furusawa\*, K. Liposome Adhesion on Mica Surface Studied by Atomic Force Microscopy. (1999). doi:10.1021/LA980923W
242. Goksu, E. I., Vanegas, J. M., Blanchette, C. D., Lin, W.-C. & Longo, M. L. AFM for structure and dynamics of biomembranes. *Biochim. Biophys. Acta - Biomembr.* **1788**, 254–266 (2009).
243. Dopico, A. *Methods in membrane lipids.* (Humana, 2007).
244. Hull, M. C., Cambrea, L. R. & Hovis, J. S. Infrared Spectroscopy of Fluid Lipid Bilayers. *Anal. Chem.* **77**, 6096–6099 (2005).
245. Smith, M. B., McGillivray, D. J., Genzer, J., Lösche, M. & Kilpatrick, P. K. Neutron reflectometry of supported hybrid bilayers with inserted peptide. *Soft Matter* **6**, 862–865 (2010).
246. Bhattacharya, G. *et al.* X-ray Reflectivity Study of the Interaction of an Imidazolium-Based Ionic Liquid with a Soft Supported Lipid Membrane. *Langmuir* **33**, 1295–1304 (2017).
247. Kiessling, V. & Tamm, L. K. Measuring Distances in Supported Bilayers by Fluorescence Interference-Contrast Microscopy: Polymer Supports and SNARE Proteins. *Biophys. J.* **84**, 408–418 (2003).
248. Rossi, C. & Chopineau, J. Biomimetic tethered lipid membranes designed for membrane-protein interaction studies. *Eur. Biophys. J.* **36**, 955–965 (2007).
249. Goennenwein, S., Tanaka, M., Hu, B., Moroder, L. & Sackmann, E. Functional Incorporation of Integrins into Solid Supported Membranes on Ultrathin Films of Cellulose: Impact on Adhesion. *Biophys. J.* **85**, 646–655 (2003).
250. Frézard, F. Liposomes: from biophysics to the design of peptide vaccines. *Brazilian J. Med. Biol. Res.* **32**, 181–189 (1999).
251. Uhumwangho, M. & Okor, R. Current trends in the production and biomedical applications of liposomes: a review. *J. Med. Biomed. Res.* **4**, (2009).
252. Deleu, M., Crowet, J.-M., Nasir, M. N. & Lins, L. Complementary biophysical tools to investigate lipid specificity in the interaction between bioactive molecules and the plasma membrane: A review. *Biochim. Biophys. Acta - Biomembr.* **1838**, 3171–3190 (2014).
253. Crane, J. M., Kiessling, V. & Tamm, L. K. Measuring Lipid Asymmetry in Planar Supported Bilayers by Fluorescence Interference Contrast Microscopy. *Langmuir* **21**, 1377–1388 (2005).
254. Oliveira, O. N. Langmuir-Blodgett Films -Properties and Possible Applications. *Brazilian J. Physiks* **22**, (1992).
255. Kalb, E., Frey, S. & Tamm, L. K. Formation of supported planar bilayers by fusion of vesicles

- to supported phospholipid monolayers. *Biochim. Biophys. Acta* **1103**, 307–16 (1992).
256. Erik Reimhult, \*, Fredrik Höök, and & Kasemo, B. Intact Vesicle Adsorption and Supported Biomembrane Formation from Vesicles in Solution: Influence of Surface Chemistry, Vesicle Size, Temperature, and Osmotic Pressure†. (2002). doi:10.1021/LA0263920
  257. Wu, H.-L., Chen, P.-Y., Chi, C.-L., Tsao, H.-K. & Sheng, Y.-J. Vesicle deposition on hydrophilic solid surfaces. *Soft Matter* **9**, 1908–1919 (2013).
  258. Seul, M. & Sammon, M. J. Preparation of surfactant multilayer films on solid substrates by deposition from organic solution. *Thin Solid Films* **185**, 287–305 (1990).
  259. Spangenberg, T., de Mello, N. F., Creczynski-Pasa, T. B., Pasa, A. A. & Niehus, H. AFM in-situ characterization of supported phospholipid layers formed by solution spreading. *Phys. status solidi* **201**, 857–860 (2004).
  260. Mennicke, U. & Salditt, T. Preparation of Solid-Supported Lipid Bilayers by Spin-Coating. *Langmuir* **18**, 8172–8177 (2002).
  261. Honigmann, A. *et al.* Phosphatidylinositol 4,5-bisphosphate clusters act as molecular beacons for vesicle recruitment. *Nat. Struct. Mol. Biol.* **20**, 679–86 (2013).
  262. Honigmann, A., Mueller, V., Hell, S. W. & Eggeling, C. STED microscopy detects and quantifies liquid phase separation in lipid membranes using a new far-red emitting fluorescent phosphoglycerolipid analogue. *Faraday Discuss.* **161**, 77–89–50 (2013).
  263. Yuan, C., Furlong, J., Burgos, P. & Johnston, L. J. The size of lipid rafts: an atomic force microscopy study of ganglioside GM1 domains in sphingomyelin/DOPC/cholesterol membranes. *Biophys. J.* **82**, 2526–35 (2002).
  264. Seghezza, S., Diaspro, A., Canale, C. & Dante, S. Cholesterol Drives A $\beta$ (1–42) Interaction with Lipid Rafts in Model Membranes. *Langmuir* **30**, 13934–13941 (2014).
  265. Alessandrini, A. & Facci, P. Unraveling lipid/protein interaction in model lipid bilayers by Atomic Force Microscopy. *J. Mol. Recognit.* **24**, 387–396 (2011).
  266. Binnig, G., Quate, C. F. & Gerber, C. Atomic Force Microscope. *Phys. Rev. Lett.* **56**, 930–933 (1986).
  267. Braet, F. & Taatjes, D. J. Foreword to the special issue on applications of atomic force microscopy in cell biology. *Semin. Cell Dev. Biol.* (2017). doi:10.1016/j.semcdb.2017.06.025
  268. Alexander, S. *et al.* An atomic-resolution atomic-force microscope implemented using an optical lever. *J. Appl. Phys.* **65**, 164–167 (1989).
  269. Thomas, G., Burnham, N. A., Camesano, T. A. & Wen, Q. Measuring the mechanical properties of living cells using atomic force microscopy. *J. Vis. Exp.* (2013). doi:10.3791/50497
  270. Chen, M., Balhara, V., Jaimes Castillo, A. M., Balsevich, J. & Johnston, L. J. Interaction of saponin 1688 with phase separated lipid bilayers. *Biochim. Biophys. Acta - Biomembr.* **1859**, 1263–1272 (2017).
  271. Lyubchenko, Y. L. & Shlyakhtenko, L. S. Imaging of DNA and Protein-DNA Complexes with Atomic Force Microscopy. *Crit. Rev. Eukaryot. Gene Expr.* **26**, 63–96 (2016).
  272. Watanabe-Nakayama, T. *et al.* High-speed atomic force microscopy reveals structural dynamics of amyloid  $\beta$ 1-42 aggregates. *Proc. Natl. Acad. Sci. U. S. A.* **113**, 5835–40 (2016).
  273. Attwood, S., Choi, Y. & Leonenko, Z. Preparation of DOPC and DPPC Supported Planar Lipid Bilayers for Atomic Force Microscopy and Atomic Force Spectroscopy. *Int. J. Mol. Sci.* **14**, 3514–3539 (2013).
  274. Shipley, G. G., Avecilla, L. S. & Small, D. M. Phase behavior and structure of aqueous dispersions of sphingomyelin.
  275. and, S. X. & Liu\*, G. Nanometer-Scale Fabrication by Simultaneous Nanoshaving and Molecular Self-Assembly. (1997). doi:10.1021/LA962029F
  276. Sullan, R. M. A., Li, J. K., Hao, C., Walker, G. C. & Zou, S. Cholesterol-dependent nanomechanical stability of phase-segregated multicomponent lipid bilayers. *Biophys. J.* **99**, 507–16 (2010).
  277. Fabbro, A. *et al.* Spinal Cord Explants Use Carbon Nanotube Interfaces To Enhance Neurite Outgrowth and To Fortify Synaptic Inputs. *ACS Nano* **6**, 2041–2055 (2012).

278. Mattson, M. P., Haddon, R. C. & Rao, A. M. Molecular Functionalization of Carbon Nanotubes and Use as Substrates for Neuronal Growth. *J. Mol. Neurosci.* **14**, 175–182 (2000).
279. Cellot, G. *et al.* Carbon Nanotube Scaffolds Tune Synaptic Strength in Cultured Neural Circuits: Novel Frontiers in Nanomaterial-Tissue Interactions. *J. Neurosci.* **31**, 12945–12953 (2011).
280. Viviana Lovat, † *et al.* Carbon Nanotube Substrates Boost Neuronal Electrical Signaling. (2005). doi:10.1021/NL050637M
281. Pampaloni, N. P. *et al.* Sculpting neurotransmission during synaptic development by 2D nanostructured interfaces. *Nanomedicine Nanotechnology, Biol. Med.* (2017). doi:10.1016/j.nano.2017.01.020
282. Exploring the ripple phase of biomembranes. *Phys. A Stat. Mech. its Appl.* **308**, 89–100 (2002).
283. Kaasgaard, T., Leidy, C., Crowe, J. H., Mouritsen, O. G. & Jørgensen, K. Temperature-Controlled Structure and Kinetics of Ripple Phases in One- and Two-Component Supported Lipid Bilayers. *Biophys. J.* **85**, 350–360 (2003).
284. Czajkowsky, D. M., Huang, sg C. & Shao, Z. Ripple Phase in Asymmetric Unilamellar Bilayers with Saturated and Unsaturated Phospholipids? *Biochemistry* **34**, 12501–12505 (1995).
285. Mazzatenta, A. *et al.* Interfacing Neurons with Carbon Nanotubes: Electrical Signal Transfer and Synaptic Stimulation in Cultured Brain Circuits. *J. Neurosci.* **27**, 6931–6936 (2007).
286. Hardy, G. J., Nayak, R. & Zauscher, S. Model cell membranes: Techniques to form complex biomimetic supported lipid bilayers via vesicle fusion. *Curr. Opin. Colloid Interface Sci.* **18**, 448–458 (2013).
287. Ong, S. G. M., Chitneni, M., Lee, K. S., Ming, L. C. & Yuen, K. H. Evaluation of Extrusion Technique for Nanosizing Liposomes. *Pharmaceutics* **8**, (2016).
288. Dopico, A. M. & Tigyi, G. J. A Glance at the Structural and Functional Diversity of Membrane Lipids. in *Methods in molecular biology (Clifton, N.J.)* **400**, 1–13 (2007).
289. Richter, R. P. & Brisson, A. R. Following the Formation of Supported Lipid Bilayers on Mica: A Study Combining AFM, QCM-D, and Ellipsometry. *Biophys. J.* **88**, 3422–3433 (2005).
290. Seantier, B. & Kasemo, B. Influence of Mono- And Divalent Ions on the Formation of Supported Phospholipid Bilayers via Vesicle Adsorption. *Langmuir* **25**, 5767–5772 (2009).
291. Yeagle, P. L. Cholesterol and the cell membrane. *Biochim. Biophys. Acta - Rev. Biomembr.* **822**, 267–287 (1985).
292. Heerklotz, H. & Tsamaloukas, A. Gradual change or phase transition: characterizing fluid lipid-cholesterol membranes on the basis of thermal volume changes. *Biophys. J.* **91**, 600–7 (2006).
293. Moreno-Altamirano, M. M. B., Aguilar-Carmona, I. & Sánchez-García, F. J. Expression of GM1, a marker of lipid rafts, defines two subsets of human monocytes with differential endocytic capacity and lipopolysaccharide responsiveness. *Immunology* **120**, 536–43 (2007).
294. Yu, R. K., Tsai, Y.-T., Ariga, T. & Yanagisawa, M. Structures, biosynthesis, and functions of gangliosides--an overview. *J. Oleo Sci.* **60**, 537–44 (2011).
295. Yanagisawa, K. GM1 ganglioside and Alzheimer's disease. *Glycoconj. J.* **32**, 87–91 (2015).
296. Linden, R. *et al.* Physiology of the Prion Protein. *Physiol. Rev.* **88**, 673–728 (2008).
297. Linden, R. *et al.* Physiology of the Prion Protein. *Physiol. Rev.* **88**, 673–728 (2008).
298. Lewis, V. & Hooper, N. M. The role of lipid rafts in prion protein biology. *Front. Biosci. (Landmark Ed.)* **16**, 151–68 (2011).
299. Priola, S. A. & McNally, K. L. The role of the prion protein membrane anchor in prion infection. *Prion* **3**, 134–8
300. Kim, J.-I., Surewicz, K., Gambetti, P. & Surewicz, W. K. The role of glycoposphatidylinositol anchor in the amplification of the scrapie isoform of prion protein in vitro. *FEBS Lett.* **583**, 3671–3675 (2009).

301. Chu, N. K. *et al.* A C-terminal membrane anchor affects the interactions of prion proteins with lipid membranes. *J. Biol. Chem.* **289**, 30144–60 (2014).
302. Giocondi, M.-C., Seantier, B., Dosset, P., Milhiet, P.-E. & Le Grimmellec, C. Characterizing the interactions between GPI-anchored alkaline phosphatases and membrane domains by AFM. *Pflügers Arch. - Eur. J. Physiol.* **456**, 179–188 (2008).
303. Milhiet, P.-E. *et al.* AFM Detection of GPI Protein Insertion into DOPC/DPPC Model Membranes. *Single Mol.* **3**, 135–140 (2002).
304. Olschewski, D. *et al.* Semisynthetic Murine Prion Protein Equipped with a GPI Anchor Mimic Incorporates into Cellular Membranes. *Chem. Biol.* **14**, 994–1006 (2007).
305. Ku, S. H. & Park, C. B. Highly Accelerated Self-Assembly and Fibrillation of Prion Peptides on Solid Surfaces. *Langmuir* **24**, 13822–13827 (2008).
306. Mao, X. *et al.* Binding modes of thioflavin T molecules to prion peptide assemblies identified by using scanning tunneling microscopy. *ACS Chem. Neurosci.* **2**, 281–7 (2011).
307. Robinson, P. J. & Pinheiro, T. J. T. Phospholipid Composition of Membranes Directs Prions Down Alternative Aggregation Pathways. *Biophys. J.* **98**, 1520–1528 (2010).
308. Pan, Y. *et al.* Nanoscale insights into full-length prion protein aggregation on model lipid membranes. *Chem. Commun.* **52**, 8533–8536 (2016).
309. Burré, J. The Synaptic Function of  $\alpha$ -Synuclein. *J. Parkinsons. Dis.* **5**, 699–713 (2015).
310. Ingelsson, M. Alpha-Synuclein Oligomers-Neurotoxic Molecules in Parkinson's Disease and Other Lewy Body Disorders. *Front. Neurosci.* **10**, 408 (2016).
311. Deas, E. *et al.* Alpha-Synuclein Oligomers Interact with Metal Ions to Induce Oxidative Stress and Neuronal Death in Parkinson's Disease. *Antioxid. Redox Signal.* **24**, 376–91 (2016).
312. Hane, F. & Leonenko, Z. Effect of metals on kinetic pathways of amyloid- $\beta$  aggregation. *Biomolecules* **4**, 101–16 (2014).
313. Lingor, P., Carboni, E. & Koch, J. C. Alpha-synuclein and iron: two keys unlocking Parkinson's disease. *J. Neural Transm.* **124**, 973–981 (2017).
314. Beck, K. *et al.* Destabilization of osteogenesis imperfecta collagen-like model peptides correlates with the identity of the residue replacing glycine.
315. Coskuner, O. & Wise-Scira, O. Structures and free energy landscapes of the A53T mutant-type  $\alpha$ -synuclein protein and impact of A53T mutation on the structures of the wild-type  $\alpha$ -synuclein protein with dynamics. *ACS Chem. Neurosci.* **4**, 1101–13 (2013).
316. Stefanovic, A. N. D., Stöckl, M. T., Claessens, M. M. A. E. & Subramaniam, V.  $\alpha$ -Synuclein oligomers distinctively permeabilize complex model membranes. *FEBS J.* **281**, 2838–2850 (2014).
317. Chaudhary, H., Iyer, A., Subramaniam, V. & Claessens, M. M. A. E.  $\alpha$ -Synuclein Oligomers Stabilize Pre-Existing Defects in Supported Bilayers and Propagate Membrane Damage in a Fractal-Like Pattern. *Langmuir* **32**, 11827–11836 (2016).
318. van Maarschalkerweerd, A., Vetri, V. & Vestergaard, B. Cholesterol facilitates interactions between  $\alpha$ -synuclein oligomers and charge-neutral membranes. *FEBS Lett.* **589**, 2661–2667 (2015).
319. Chaudhary, H., Stefanovic, A. N. D., Subramaniam, V. & Claessens, M. M. A. E. Membrane interactions and fibrillization of  $\alpha$ -synuclein play an essential role in membrane disruption. *FEBS Lett.* **588**, 4457–4463 (2014).
320. Choucair, A., Chakrapani, M., Chakravarthy, B., Katsaras, J. & Johnston, L. J. Preferential accumulation of A $\beta$ (1–42) on gel phase domains of lipid bilayers: An AFM and fluorescence study. *Biochim. Biophys. Acta - Biomembr.* **1768**, 146–154 (2007).
321. Li, W., Jiang, H., Song, N. & Xie, J. Oxidative Stress Partially Contributes to Iron-Induced Alpha-Synuclein Aggregation in SK-N-SH Cells. *Neurotox. Res.* **19**, 435–442 (2011).
322. Levin, J. *et al.* Generation of ferric iron links oxidative stress to  $\alpha$ -synuclein oligomer formation. *J. Parkinsons. Dis.* **1**, 205–16 (2011).
323. Nečas, D. & Klapetek, P. Gwyddion: an open-source software for SPM data analysis. *Open Phys.* **10**, 181–188 (2012).

324. Oropesa-Nuñez, R. *et al.* Interaction of toxic and non-toxic HypF-N oligomers with lipid bilayers investigated at high resolution with atomic force microscopy. *Oncotarget* **7**, 44991–45004 (2016).
325. Huang, C., Ren, G., Zhou, H. & Wang, C. A new method for purification of recombinant human  $\alpha$ -synuclein in Escherichia coli. *Protein Expr. Purif.* **42**, 173–177 (2005).
326. Fais, S. *et al.* Evidence-Based Clinical Use of Nanoscale Extracellular Vesicles in Nanomedicine. *ACS Nano* **10**, 3886–3899 (2016).
327. Bourkoula, E. *et al.* Glioma-Associated Stem Cells: A Novel Class of Tumor-Supporting Cells Able to Predict Prognosis of Human Low-Grade Gliomas. *Stem Cells* **32**, 1239–1253 (2014).
328. Vella, L. J. The Emerging Role of Exosomes in Epithelial–Mesenchymal-Transition in Cancer. *Front. Oncol.* **4**, 361 (2014).
329. Svensson, K. J. *et al.* Hypoxia triggers a proangiogenic pathway involving cancer cell microvesicles and PAR-2-mediated heparin-binding EGF signaling in endothelial cells. *Proc. Natl. Acad. Sci. U. S. A.* **108**, 13147–52 (2011).
330. Skog, J. *et al.* Glioblastoma microvesicles transport RNA and proteins that promote tumour growth and provide diagnostic biomarkers. *Nat. Cell Biol.* 2008 1012 **10**, 1470 (2008).
331. Akers, J. C. *et al.* miR-21 in the Extracellular Vesicles (EVs) of Cerebrospinal Fluid (CSF): A Platform for Glioblastoma Biomarker Development. *PLoS One* **8**, e78115 (2013).
332. Woo, J., Sharma, S. & Gimzewski, J. The Role of Isolation Methods on a Nanoscale Surface Structure and its Effect on the Size of Exosomes. *J. Circ. Biomarkers* **5**, 11 (2016).
333. Paolini, L. *et al.* Residual matrix from different separation techniques impacts exosome biological activity. *Sci. Rep.* **6**, 23550 (2016).
334. Khatun, Z., Bhat, A., Sharma, S. & Sharma, A. Elucidating diversity of exosomes: biophysical and molecular characterization methods. *Nanomedicine* **11**, 2359–2377 (2016).
335. Iwai, K., Minamisawa, T., Suga, K., Yajima, Y. & Shiba, K. Isolation of human salivary extracellular vesicles by iodixanol density gradient ultracentrifugation and their characterizations. *J. Extracell. Vesicles* **5**, 30829 (2016).
336. Gholizadeh, S. *et al.* Microfluidic approaches for isolation, detection, and characterization of extracellular vesicles: Current status and future directions. *Biosens. Bioelectron.* **91**, 588–605 (2017).
337. Parisse, P. *et al.* Atomic force microscopy analysis of extracellular vesicles. *Eur. Biophys. J.* **46**, 813–820 (2017).
338. Whitehead, B. *et al.* Tumour exosomes display differential mechanical and complement activation properties dependent on malignant state: implications in endothelial leakiness. *J. Extracell. Vesicles* **4**, 29685 (2015).
339. Regev-Rudzki, N. *et al.* Cell-Cell Communication between Malaria-Infected Red Blood Cells via Exosome-like Vesicles. *Cell* **153**, 1120–1133 (2013).
340. Danielson, K. M. *et al.* Diurnal Variations of Circulating Extracellular Vesicles Measured by Nano Flow Cytometry. *PLoS One* **11**, e0144678 (2016).
341. Di Noto, G. *et al.* Merging colloidal nanoplasmonics and surface plasmon resonance spectroscopy for enhanced profiling of multiple myeloma-derived exosomes. *Biosens. Bioelectron.* **77**, 518–524 (2016).
342. Hardij, J. *et al.* Characterisation of tissue factor-bearing extracellular vesicles with AFM: comparison of air-tapping-mode AFM and liquid Peak Force AFM. *J. Extracell. Vesicles* **2**, 21045 (2013).
343. Sharma, S. *et al.* Structural-Mechanical Characterization of Nanoparticle Exosomes in Human Saliva, Using Correlative AFM, FESEM, and Force Spectroscopy. *ACS Nano* **4**, 1921–1926 (2010).
344. Sharma, S. & K. Gimzewski, J. The Quest for Characterizing Exosomes: Circulating Nano-Sized Vesicles. *J. Nanomed. Nanotechnol.* **3**, (2012).
345. Palanisamy, V. *et al.* Nanostructural and Transcriptomic Analyses of Human Saliva Derived Exosomes. *PLoS One* **5**, e8577 (2010).
346. Rauti, R. *et al.* Graphene Oxide Nanosheets Reshape Synaptic Function in Cultured Brain

- Networks. *ACS Nano* **10**, 4459–4471 (2016).
347. Nguyen, D. B. *et al.* Characterization of Microvesicles Released from Human Red Blood Cells. *Cell. Physiol. Biochem.* **38**, 1085–99 (2016).
348. Sebaihi, N., De Boeck, B., Yuana, Y., Nieuwland, R. & Pétry, J. Dimensional characterization of extracellular vesicles using atomic force microscopy. *Meas. Sci. Technol.* **28**, 34006 (2017).
349. Chernyshev, V. S. *et al.* Size and shape characterization of hydrated and desiccated exosomes. *Anal. Bioanal. Chem.* **407**, 3285–3301 (2015).
350. Canet-Ferrer, J., Coronado, E., Forment-Aliaga, A. & Pinilla-Cienfuegos, E. Correction of the tip convolution effects in the imaging of nanostructures studied through scanning force microscopy. *Nanotechnology* **25**, 395703 (2014).
351. Usmani, S. *et al.* 3D meshes of carbon nanotubes guide functional reconnection of segregated spinal explants. *Sci. Adv.* **2**, e1600087–e1600087 (2016).

## **ACKNOWLEDGMENTS**

**I wish to thank my supervisor Dr. Loredana Casalis who gave the possibility to work in her laboratory and for a great help for the production of my PhD. thesis in the right direction.**

**I would like to thank my Co-supervisor Dr. Denis Scaini for a great help with experimental work.**

**I wish to thank Prof. Giuseppe Legname for providing me Alpha synuclein proteins and lipidated-Prion protein.**

**I must acknowledge the SISSI group, especially Chiara for helping me in IR-experiments**

**I would like to thank further all group members of NanoInnovation Laboratory at Elettra, Pietro, Luisa, Ilaria and the previous members Elena, Cap, Amna. A special thanks go to Maryse, who taught me and guided at the beginning of my PhD. journey.**

**Big gratitude to all of my friends and my family for supporting me in all these years.**